

# Towards Large-Scale Quantum Computation

Austin Greig Fowler

Submitted in total fulfilment of the requirements  
of the degree of Doctor of Philosophy

March 2005

School of Physics  
The University of Melbourne

# Abstract

This thesis deals with a series of quantum computer implementation issues from the Kane  $^{31}\text{P}$  in  $^{28}\text{Si}$  architecture to Shor's integer factoring algorithm and beyond. The discussion begins with simulations of the adiabatic Kane CNOT and readout gates, followed by linear nearest neighbor implementations of 5-qubit quantum error correction with and without fast measurement. A linear nearest neighbor circuit implementing Shor's algorithm is presented, then modified to remove the need for exponentially small rotation gates. Finally, a method of constructing optimal approximations of arbitrary single-qubit fault-tolerant gates is described and applied to the specific case of the remaining rotation gates required by Shor's algorithm.

# Declaration

This is to certify that

1. the thesis comprises only my original work towards the PhD,
2. due acknowledgement has been made in the text to all other material used,
3. the thesis is less than 100,000 words in length, exclusive of tables, maps, bibliographies and appendices.

---

# Acknowledgements

This thesis would never have been finished without the help of a number of people. My parents, who have put up with me for more years than I care to mention and have always been there when I needed them. My supervisor, Lloyd Hollenberg, for the freedom he has allowed me and his constant academic and professional support. The DLU, and specifically Maun Suang Boey, for years of assistance above and beyond the call of duty. I am in your debt. I have enjoyed getting to know you as much as working with you. Adam Healy, for his friendship, and, together with Paul Noone, turning my life around. And finally, Natasha, who didn't help me finish the thesis at all, but showed me I was human.

# Contents

1. <i>Introduction</i> . . . . .	1
1.1 Why quantum compute? . . . . .	1
1.2 Models of quantum computing . . . . .	3
1.2.1 The circuit model . . . . .	4
1.2.2 Adiabatic quantum computation . . . . .	8
1.2.3 Cluster states . . . . .	8
1.2.4 Topological quantum computation . . . . .	9
1.2.5 Geometric quantum computation . . . . .	12
1.3 Quantum computation is possible in principle . . . . .	12
1.4 Overview . . . . .	20
2. <i>The adiabatic Kane CNOT gate</i> . . . . .	23
2.1 The Kane architecture . . . . .	24
2.2 Adiabatic CNOT pulse profiles . . . . .	26
2.3 Intrinsic dephasing and fidelity . . . . .	33
2.4 Conclusion . . . . .	34
3. <i>Adiabatic Kane single-spin readout</i> . . . . .	39
3.1 Adiabatic readout pulse profiles . . . . .	39
3.2 Readout performance . . . . .	40
3.3 Conclusion . . . . .	42

---

4. <i>Implementing arbitrary 2-qubit gates</i> . . . . .	45
4.1 Background . . . . .	46
4.2 Terminology and notation . . . . .	48
4.3 Constructing a canonical decomposition . . . . .	49
4.4 Making a canonical decomposition unique . . . . .	52
4.5 Building gates out of physical interactions . . . . .	53
4.6 Conclusion . . . . .	55
5. <i>5-qubit QEC on an LNN QC</i> . . . . .	57
5.1 Compound gates . . . . .	58
5.2 5-qubit LNN QEC . . . . .	59
5.3 Simulation of performance . . . . .	60
5.4 Conclusion . . . . .	65
6. <i>QEC without measurement</i> . . . . .	67
6.1 Resetting . . . . .	68
6.2 5-qubit QEC without measurement . . . . .	69
6.3 5-qubit QEC with slow resetting . . . . .	72
6.4 Conclusion . . . . .	72
7. <i>Shor's algorithm</i> . . . . .	75
8. <i>Shor's algorithm on an LNN QC</i> . . . . .	83
8.1 Decomposing Shor's algorithm . . . . .	84
8.2 Quantum Fourier Transform . . . . .	87
8.3 Modular Addition . . . . .	89
8.4 Controlled swap . . . . .	92
8.5 Modular Multiplication . . . . .	94
8.6 Complete Circuit . . . . .	94

---

8.7 Conclusion . . . . .	96
9. <i>Shor's algorithm with a limited set of rotation gates</i> . . . . .	99
9.1 Approximate quantum Fourier transform . . . . .	100
9.2 Dependence of output reliability on period of $f(k) = m^k \bmod N$	101
9.3 Dependence of output usefulness on integer length and rota- tion gate set . . . . .	103
9.4 Conclusion . . . . .	107
10. <i>Constructing arbitrary single-qubit fault-tolerant gates</i> . . . . .	109
10.1 Finding optimal approximations . . . . .	110
10.2 Simple Steane code single-qubit gates . . . . .	112
10.3 The fault-tolerant T-gate . . . . .	116
10.4 Approximations of phase gates . . . . .	125
10.5 Approximations of arbitrary gates . . . . .	131
10.6 Conclusion . . . . .	133
11. <i>Concluding remarks</i> . . . . .	135
<i>Appendix</i>	139
A. <i>Simple Steane code gates</i> . . . . .	141





# List of Figures

1.1	(a) Common single-qubit gates, (b) the CNOT gate with solid dot representing the control qubit, (c) the swap gate. . . . .	6
1.2	(a) Example of a quantum circuit, (b) depth 6 rearrangement of (a). This circuit implements the encode stage of 5-qubit non-fault-tolerant quantum error correction. . . . .	7
1.3	Lattice of hypothetical particles used in the construction of the anyonic model of quantum computation. . . . .	10
1.4	A conjugate pair of non-Abelian anyons. . . . .	11
1.5	Performing operations in the anyonic model of quantum computation. . . . .	11
1.6	Example of the path independence of the phase shift induced by the Aharonov-Bohm effect. A particle of charge $q$ executing a loop around a perfectly insulated solenoid containing flux $\Phi$ acquires a geometric phase $e^{iq\Phi}$ . . . . .	13
1.7	7-qubit transversal logical CNOT gate. . . . .	17
2.1	Schematic of the Kane architecture. The rightmost two qubits show the notation to be used when discussing the CNOT gate. .	25
2.2	Gate profiles and state energies during a CNOT gate in units of $g_n\mu_n B_z = 7.1 \times 10^{-5}\text{meV}$ . . . . .	30

---

2.3	Possible forms of the $J(t)$ profile for step 2 of the adiabatic CNOT gate. $J(t)$ is in units of $g_n\mu_n B_z = 7.1 \times 10^{-5}\text{meV}$ . . . . .	31
2.4	The adiabatic measure $\Theta(t)$ for each $J(t)$ profile. . . . .	32
2.5	Probability of error $\varepsilon$ during a CNOT gate as a function of $\tau_e$ and $\tau_n$ for input state (a) $ 00\rangle$ and (b) $ 01\rangle$ . The first qubit is the control. . . . .	35
2.6	Probability of error $\varepsilon$ during a CNOT gate as a function of $\tau_e$ and $\tau_n$ for input state (a) $ 10\rangle$ and (b) $ 11\rangle$ . The first qubit is the control. . . . .	36
2.7	The worst case probability of error $\varepsilon$ during a CNOT gate as a function of $\tau_e$ and $\tau_n$ for all input states. . . . .	37
3.1	Geometry of adiabatic Kane readout. . . . .	40
3.2	Evolution of the hyperfine and exchange interaction strengths required to convert nuclear spin information into electron spin information, as shown in Eqs. (3.1–3.4). . . . .	41
3.3	Probability of error $\varepsilon$ during readout state preparation as a function of $\tau_e$ and $\tau_n$ for input state (a) $ 00\rangle$ and (b) $ 01\rangle$ . . . .	43
3.4	Probability of error $\varepsilon$ during readout state preparation as a function of $\tau_e$ and $\tau_n$ for input state $ 10\rangle$ . . . . .	44
4.1	(a) Circuit equivalent to an arbitrary gate constructed via the canonical decomposition. (b) Similar equivalent circuit which exists for a restricted class of 2-qubit evolution operators. (c) Arbitrary gate expressed as at most three periods evolution of the 2-qubit evolution operator and eight single-qubit gates. . .	47

---

5.1	Decomposition into physical operations of (a) CNOT and (b) Hadamard, CNOT then swap. Note that the Kane architecture has been used for illustrative purposes. . . . .	59
5.2	(a) 5-qubit encoding circuit for general architecture, (b) equivalent circuit for linear nearest neighbor architecture with dashed boxes indicating compound gates. CNOT gates that must be performed sequentially are numbered. . . . .	60
5.3	A sequence of physical gates implementing the circuit of Fig. 5.2b. Note the Kane architecture has been used for illustrative purposes. . . . .	61
5.4	Circuit equivalence used to reduce the number of physical gates in Fig. 5.3. $W = U_{A_2} V_{B_1}$ . . . . .	61
5.5	A complete encode-wait-decode-measure-correct QEC cycle. . .	61
6.1	Example of a physical model of resetting through relaxation. Given a double potential well with left and right occupancy representing $ 0\rangle$ and $ 1\rangle$ respectively, resetting to $ 0\rangle$ can be achieved by lowering the barrier and applying a bias. . . . .	68
6.2	Quantum circuit acting on a recently decoded logical qubit to correct the data qubit based on the value of the ancilla qubits. Hollow dots represent control qubits that must be $ 0\rangle$ for the attached gate to be applied. . . . .	69
6.3	Linear nearest neighbor version of Fig. 6.2. . . . .	70
6.4	5-qubit quantum error correction scheme not requiring fast measurement or classical processing. . . . .	73

- 
- 7.1 The complete Shor's algorithm including classical pre- and post-processing. The first branch is highly likely to fail, resulting in many repetitions of the quantum heart of the algorithm, whereas the second branch is highly likely to succeed. . . . . 77
- 7.2 Probability of different measurements  $j$  at the end of quantum period finding with total number of states  $2^{2L} = 256$  and (a) period  $r = 8$ , (b) period  $r = 10$ . . . . . 80
- 8.1 (a) Standard quantum Fourier transform circuit. (b) An equivalent linear nearest neighbor circuit. . . . . 87
- 8.2 (a) Swap gate expressed as a sequence of physical operations via the canonical decomposition. (b) Similarly decomposed compound gate consisting of a Hadamard gate, controlled phase rotation, and swap gate. Note that the Kane architecture has been used for illustrative purposes. . . . . 88
- 8.3 (a) Quantum Fourier addition. (b) Controlled quantum Fourier addition and its symbolic equivalent circuit.  $Cont + a$  denotes the addition of  $a$  if  $Cont = 1$ . . . . . 89

- 
- 8.4 Circuit to compute  $c = (b + 2^j m^{2^i}) \bmod N$ . The diagonal circuit elements labelled swap represent a series of 2-qubit swap gates. Small gates spaced close together represent compound gates. The qubits  $x(i)$  are defined in Eq. 8.2 and essentially store the current partially calculated value of the modular exponentiation that forms the heart of Shor's algorithm. The  $MS$  (Most Significant) qubit is used to keep track of the sign of the partially calculated modular addition result. The  $k_i$  qubit is the  $i$ th bit of  $k$  in Eq. 8.1. The  $kx$  qubit is set to 1 if and only if  $x(i)_j = k_i = 1$ .  $kx \pm 2^j m^{2^i} \bmod N$  denotes modular addition (subtraction) conditional on  $kx = 1$ . . . . . 91
- 8.5 Circuit designed to interleave two quantum registers. . . . . 93
- 8.6 (a) LNN circuit for the controlled swapping of two qubits  $|a\rangle$  and  $|b\rangle$ . The qubits  $|a'\rangle$  and  $|b'\rangle$  represent the potentially swapped states. (b) LNN circuit for the controlled swapping of two quantum registers. Note that when chained together, the effective depth of the cswap gate is 4. . . . . 93
- 8.7 Circuit designed to modularly multiply  $x(i)$  by  $m^{2^i}$  if and only if  $k_i = 1$ . Note that for simplicity the circuit for  $L = 4$  has been shown. Note that the bottom  $L + 1$  qubits are ancilla and as such start and end in the  $|\phi(0)\rangle$  state. The swap gates within the two QFT structures represent compound gates.  $k_i \times m^{2^i} \bmod N$  denotes modular multiplication conditional on  $k_i = 1$ . 95

8.8	Circuit implementing the quantum part of Shor's algorithm. The single-qubit gates interleaved between the modular multiplications comprise a QFT that has been decomposed by using measurement gates to remove the need for controlled quantum phase rotations. Note that without these single-qubit gates the remaining circuit is simply modular exponentiation. . . . .	97
9.1	Circuit for a 4-qubit (a) quantum Fourier transform and (b) approximate quantum Fourier transform with $d_{\max} = 1$ . . . . .	100
9.2	Decomposition of a controlled phase gate into single-qubit rotations and a CNOT gate. . . . .	103
9.3	Probability $s$ of obtaining useful output from quantum period finding as a function of period $r$ for different integer lengths $L$ and rotation gate restrictions $\pi/2^{d_{\max}}$ . The effect of using inaccurate controlled rotation gates ( $\sigma = \pi/32$ ) is shown in (e). . . . .	104
9.4	Dependence of the probability of useful output from the quantum part of Shor's algorithm on the length $L$ of the integer being factored for different levels of restriction of controlled rotation gates of angle $\pi/2^{d_{\max}}$ . The parameter $L_0$ characterizes lines of best fit of the form $s \propto 2^{-L/L_0}$ . . . . .	105
10.1	Non-fault-tolerant 7-qubit Steane code encoding circuits taking an arbitrary state $\alpha 0\rangle + \beta 1\rangle$ and producing $\alpha 0_L\rangle + \beta 1_L\rangle$ . (a) Depth 4 circuit for an architecture able to interact arbitrary pairs of qubits. (b) Depth 5 circuit for a linear nearest neighbor architecture. . . . .	114

10.2	Circuits fault-tolerantly applying common single-qubit gates to Steane code logical qubits. Gates in brackets are optional as they implement stabilizers. . . . .	117
10.3	High-level representation of the circuit implementing the $T$ -gate on a Steane code logical qubit. Input $\alpha 0_L\rangle + \beta 1_L\rangle$ is transformed into $\alpha 0_L\rangle + \beta e^{i\pi/4} 1_L\rangle$ . . . . .	117
10.4	Circuit measuring whether $ \Psi\rangle$ is in the $+1$ or $-1$ eigenstate of $A$ . . . . .	118
10.5	(a) Simple circuit fault-tolerantly preparing a cat state. (b) Circuit undoing the preparation of a cat state. . . . .	119
10.6	Typical, but unnecessarily complicated circuit fault-tolerantly preparing a cat state. . . . .	120
10.7	Symbolic representation of transversal controlled operations. . .	121
10.8	Circuit fault-tolerantly projecting $ \Psi\rangle$ onto the $\pm 1$ eigenstates of $XIXIXIX$ , then converting $-1$ eigenstate's into $+1$ eigenstates. The third measurement structure can be omitted if $M_1 = M_2$ . .	121
10.9	Circuit taking arbitrary input and producing $ 0_L\rangle$ by repeated stabilizer measurement. . . . .	122
10.10	Circuit taking arbitrary input and producing $ 0_L\rangle$ via physical resetting and just three stabilizer measurements. . . . .	122
10.11	Complete circuit implementing the $T$ -gate on a Steane code logical qubit. . . . .	124
10.12	Optimal fault-tolerant approximations $U_l$ of phase rotation gates $R_{2^d}$ , for $R_8$ to $R_{128}$ . . . . .	126
10.13	Non-fault-tolerant circuit exactly implementing $R_{128}$ by first decoding the logical qubit and re-encoding after application of $R_{128}$ . . . . .	128

---

10.14	Schematic of a minimum complexity, sufficiently accurate fault-tolerant approximation of $R_{128}$ given in full by Eq. (10.26). . .	128
10.15	Circuit fault-tolerantly correcting an arbitrary single error within the logical qubit. The qubit acted on by the correct $Z/X$ boxes is described by Table 10.2. . . . .	129
10.16	Approximate probability of more than one error in the output logical qubit versus probability per qubit per time step of discrete error for different circuits implementing a $R_{128}$ phase rotation gate. (a) NFT: non-fault-tolerant circuit from Fig. 10.13, (b) FT I: fault-tolerant circuit from Fig. 10.14, (c) FT II: as above but with Fig. 10.15 error correction after every second T-gate, (d) FT III: as above but with error correction after every T-gate. Note that all fault-tolerant results are for the 7-qubit Steane code without concatenation. . . . .	130
10.17	Average accuracy of optimal fault-tolerant gate sequence approximations of length $l$ . . . . .	133



# List of Tables

5.1	Action required to correct the data qubit $\Psi'$ vs measured value of ancilla qubits. Note that the X-operations simply reset the ancilla. . . . .	62
5.2	Probability per time step $\epsilon_{step}$ of the logical qubit being destroyed when using 5-qubit QEC vs physical probability $p$ per qubit per time step of a discrete error. . . . .	64
5.3	Probability per time step $\epsilon_{step}$ of the logical qubit being destroyed when using 5-qubit QEC vs standard deviation $\sigma$ of continuous errors. . . . .	65
6.1	Second column shows the action required to correct the data qubit given a certain ancilla value immediately after decoding. Third column shows the action required to correct the data qubit given a certain ancilla value after the application of the first half of Fig. 6.2. . . . .	70
6.2	Probability per time step $\epsilon_{step}$ of the logical qubit being destroyed when using no measurement 5-qubit QEC vs physical probability $p$ per qubit per time step of a discrete error. . . . .	71
6.3	Probability per time step $\epsilon_{step}$ of the logical qubit being destroyed when using no measurement 5-qubit QEC vs standard deviation $\sigma$ of continuous errors. . . . .	71

7.1	Required number of qubits and circuit depth of different implementations of the quantum part of Shor's algorithm. Where possible, figures are accurate to leading order in $L$ . . . . .	76
10.1	Best case complexity of the T-gate. . . . .	124
10.2	Qubit to correct given certain sequence of eigenvalue measurements in both halves of Fig. 10.15. . . . .	130

# 1. Introduction

This chapter begins with a brief review of the quantum computing field with a bias towards the specific topics developed in later chapters. The main purpose of the review is to introduce the concepts and language required to overview the aims and content of this thesis (Section 1.4). The reader familiar with quantum computing can go directly to Section 1.4. Familiarity with quantum mechanics is assumed.

In Section 1.1 we provide justification and motivation for the study of quantum computing. Section 1.2 reviews the various models of quantum computation, namely the circuit model, adiabatic quantum computation, cluster states, topological quantum computation, and geometric quantum computation. The theoretical work demonstrating that arbitrarily large quantum computations can be performed arbitrarily reliably is gathered in Section 1.3. Section 1.4 then overviews the thesis.

## *1.1 Why quantum compute?*

The incredible exponential growth in the number of transistors used in conventional computers, popularly described as Moore's Law, is expected to continue until at least the end of this decade [1]. This growth is achieved through miniaturization. Smaller transistors consume less power, can be packed more densely, and switch faster. However, in some areas, particu-

larly the silicon dioxide insulating layer within each transistor, atomic scales are already being approached [2]. This fundamental barrier is one of many factors fuelling research into radical new computing technologies.

Furthermore, certain problems simply cannot be solved efficiently on conventional computers irrespective of their inexorable technological and computational progress. One such problem is the simulation of quantum systems. The amount of classical data required to describe a quantum system grows exponentially with the system size. The data storage problem alone precludes the existence of an efficient method of simulation on a conventional computer.

The first hint of a way around this impasse was provided by Feynman in 1982 [3] when he suggested using quantum mechanical components to store and manipulate the data describing a quantum system. The number of quantum mechanical components required would be directly proportional to the size of the quantum system. This idea was built on by Deutsch in 1985 [4] to form a model of computation called a quantum Turing machine — the quantum mechanical equivalent of the universal Turing machine [5] which previously was thought to be the most powerful and only model of computation.

That the laws of physics in principle permit the construction of quantum computers exponentially more powerful than their classical relatives is hugely significant. Despite this, it was not until the publication of Shor's quantum integer factoring algorithm [6] that research into quantum computing began to attract serious attention. The difficulty of classically factoring integers forms the basis of the popular RSA encryption protocol [7]. RSA is used to establish secure connections over the Internet, enabling the transmission of sensitive data such as passwords, credit card details, and online

banking sessions. RSA also forms the heart of the popular secure messaging utility PGP (Pretty Good Privacy) [8]. Rightly or wrongly, the prospect of rendering much of modern classical communication insecure has arguably driven the race to build a quantum computer.

More recently, quantum algorithm offering an exponential speed up over their classical equivalents have been devised for problems within group theory [9], knot theory [10], eigenvalue calculation [11], image processing [12], basis transformations [13], and numerical integrals [14]. Other promising quantum algorithms exist [15, 16], but have not been thoroughly analyzed.

On the commercial front, the communication of quantum data has been shown to enable unconditionally secure communication in principle [17] resulting in the creation of companies offering real products [18, 19] that have already found application in the information technology sector [20]. Despite this, it remains to be seen whether human ingenuity is sufficient to make large-scale quantum computing a reality.

## 1.2 Models of quantum computing

Classical computers have a single well defined computational model — the direct manipulation of bits via Boolean logic. The field of quantum computation is too young to have settled on a single model. This section attempts to make a brief yet complete review of the current status of the various quantum computation models currently under investigation. We neglect quantum Turing machines [4] as they are a purely abstract rather than a physically realisable computation model. We also neglect quantum neural networks [21, 22] due to their use of nonlinear gates, and both Type II quantum computers [23] and quantum cellular automata [24] due to their essentially classical nature.

### 1.2.1 The circuit model

The most widely used model of quantum computation is called the circuit model. Instead of the traditional bits of conventional computing which can take the values 0 or 1, the circuit model is based on qubits which are quantum systems with two states denoted by  $|0\rangle$  and  $|1\rangle$ . The power of quantum computing lies in the fact that qubits can be placed in superpositions  $\alpha|0\rangle + \beta|1\rangle$ , and entangled with one another, eg.  $(|00\rangle + |11\rangle)/\sqrt{2}$ . Manipulation of qubits is performed via quantum gates. An  $n$ -qubit gate is a  $2^n \times 2^n$  unitary matrix. The most general single-qubit gate can be written in the form

$$U = \begin{pmatrix} e^{i(\alpha+\beta)/2} \cos \theta & e^{i(\alpha-\beta)/2} \sin \theta \\ -e^{i(-\alpha+\beta)/2} \sin \theta & e^{-i(\alpha+\beta)/2} \cos \theta \end{pmatrix}. \quad (1.1)$$

Common single-qubit gates are

$$\begin{aligned} H &= \frac{1}{\sqrt{2}} \begin{pmatrix} 1 & 1 \\ 1 & -1 \end{pmatrix}, & X &= \begin{pmatrix} 0 & 1 \\ 1 & 0 \end{pmatrix}, & Z &= \begin{pmatrix} 1 & 0 \\ 0 & -1 \end{pmatrix}, \\ S &= \begin{pmatrix} 1 & 0 \\ 0 & i \end{pmatrix}, & S^\dagger &= \begin{pmatrix} 1 & 0 \\ 0 & -i \end{pmatrix}, & T &= \begin{pmatrix} 1 & 0 \\ 0 & e^{i\pi/4} \end{pmatrix}. \end{aligned} \quad (1.2)$$

For example, the result of applying an  $X$ -gate to  $\alpha|0\rangle + \beta|1\rangle$  is

$$\begin{pmatrix} 0 & 1 \\ 1 & 0 \end{pmatrix} \begin{pmatrix} \alpha \\ \beta \end{pmatrix} = \begin{pmatrix} \beta \\ \alpha \end{pmatrix}. \quad (1.3)$$

The  $X$ -gate will sometimes be referred to as a NOT gate or inverter. Its action will sometimes be referred to as a bit-flip or inversion, and that of the  $Z$ -gate as a phase-flip. The  $H$ -gate was derived from the Walsh-Hadamard transform [25, 26] and first named as the Hadamard gate in [27].

Given the ability to implement arbitrary single qubit gates and almost any multiple qubit gate, arbitrary quantum computations can be performed [28, 29]. The column vector form of an arbitrary 2-qubit state  $|\Psi\rangle = \alpha|00\rangle + \beta|01\rangle + \gamma|10\rangle + \delta|11\rangle$  is

$$\begin{pmatrix} \alpha \\ \beta \\ \gamma \\ \delta \end{pmatrix}. \quad (1.4)$$

Note the ordering of the computational basis states. For convenience, such states will occasionally be denoted by  $|q_1q_0\rangle$  with  $q_1$  ( $q_0$ ) referred to as the first (last) or left (right) qubit regardless of the actual physical arrangement. The most common 2-qubit gate is the controlled-NOT (CNOT)

$$\begin{pmatrix} 1 & 0 & 0 & 0 \\ 0 & 1 & 0 & 0 \\ 0 & 0 & 0 & 1 \\ 0 & 0 & 1 & 0 \end{pmatrix}, \quad (1.5)$$

which given an arbitrary 2-qubit state  $|q_1q_0\rangle$ , inverts the target qubit  $q_0$  if the control qubit  $q_1$  is 1. Note that a CNOT with target qubit  $q_1$  and control qubit  $q_0$  would have the form

$$\begin{pmatrix} 1 & 0 & 0 & 0 \\ 0 & 0 & 0 & 1 \\ 0 & 0 & 1 & 0 \\ 0 & 1 & 0 & 0 \end{pmatrix}. \quad (1.6)$$

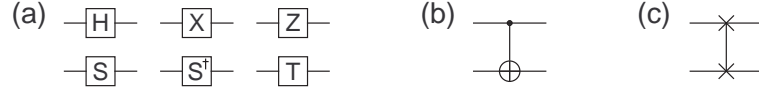


Fig. 1.1: (a) Common single-qubit gates, (b) the CNOT gate with solid dot representing the control qubit, (c) the swap gate.

The swap gate

$$\begin{pmatrix} 1 & 0 & 0 & 0 \\ 0 & 0 & 1 & 0 \\ 0 & 1 & 0 & 0 \\ 0 & 0 & 0 & 1 \end{pmatrix} \quad (1.7)$$

swaps the states of  $q_1$  and  $q_0$ . Additional 2-qubit gates will be defined as required.

By representing qubits as horizontal lines, a time sequence of quantum gates can conveniently be represented by notation that looks like a conventional circuit. Symbols equivalent to the gates described above are shown in Fig. 1.1. An example of a complete circuit is shown in Fig. 1.2a. Note that the horizontal lines represent time flowing from left to right, not wires. We define the depth of a quantum circuit to be the number of layers of 2-qubit gates required to implement it. Note that multiple single-qubit gates and 2-qubit gates applied to the same two qubits can be combined into a single 2-qubit gate. For example, Fig. 1.2b is a depth 6 rearrangement of Fig. 1.2a. These circuits are discussed in more detail in Chapter 5.

The basis  $\{|0\rangle, |1\rangle\}$  is referred to as the computational basis. The simplest representation of an  $n$ -qubit state is

$$|\Psi\rangle = \frac{1}{\sqrt{2^n}} \sum_{k=1}^{2^n-1} |k\rangle, \quad (1.8)$$

where  $k$  is an  $n$ -bit number. The information theoretic properties of qubits



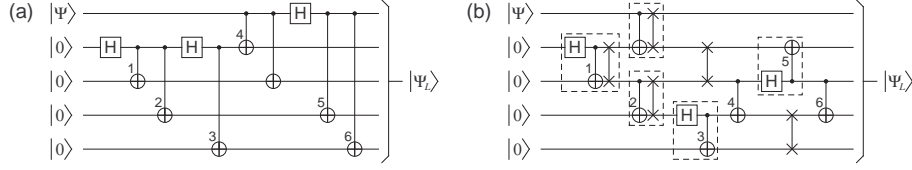


Fig. 1.2: (a) Example of a quantum circuit, (b) depth 6 rearrangement of (a). This circuit implements the encode stage of 5-qubit non-fault-tolerant quantum error correction.

have undergone investigation by many authors and are well reviewed in [30].

One natural extension of the qubit circuit model is to use  $d$ -level quantum systems (qudits). The simplest representation of an  $n$ -qudit state is

$$|\Psi\rangle = \frac{1}{\sqrt{d^n}} \sum_{k=1}^{d^n-1} |k\rangle, \quad (1.9)$$

where  $k$  is expressed in base  $d$ . The properties of qudit entanglement [31], qudit teleportation [32], qudit error correction [33, 34], qudit cryptography [35, 36], and qudit algorithms [37, 38] are broadly similar to the corresponding properties of qubits, and will not be discussed further here.

A third variant of the circuit model exists based on continuous quantum variables such as the position and momentum eigenstates of photons. Considerable experimental work on the entanglement of continuous quantum variables has been performed and is reviewed in Ref. [39]. In particular, the problem of continuous quantum variable teleportation [40] has received a great deal of attention. Furthermore, methods have been devised to perform continuous variable error correction [41], cryptography [42], and continuous variable versions of a number of algorithms [43, 44, 45, 46].

### 1.2.2 Adiabatic quantum computation

In the adiabatic model of quantum computation [47], a Hamiltonian  $H_f$  is found such that its ground state is the solution of the problem under consideration. This final Hamiltonian  $H_f$  must also be continuously deformable (for example, by varying the strength of a magnetic field) to some initial Hamiltonian  $H_i$  with a ground state that is easy to prepare. After initializing the computer in the ground state of  $H_i$ ,  $H_i$  is adiabatically (i.e. sufficiently slowly to leave the system in the ground state) deformed into  $H_f$  yielding the ground state of  $H_f$ . The major difficulty is determining how slowly the deformation must occur to be adiabatic. The adiabatic model can be applied to systems of qubits, qudits, and continuous quantum variables, and is equivalent to the circuit model in the sense that any adiabatic algorithm can be converted into a quantum circuit with at most polynomial overhead [48, 49]. The principal advantage of the adiabatic model is an alternative way of thinking about quantum computation that has led to numerous new algorithms tackling problems in graph theory [50], combinatorics [47, 51], condensed matter and nuclear physics [52], and set theory [53].

### 1.2.3 Cluster states

Given a multi-dimensional lattice of qubits each initialized to  $(|0\rangle + |1\rangle)/\sqrt{2}$  with identical tunable nearest neighbor interactions of form

$$H_{ij}(t) = \hbar g(t)(1 + \sigma_z^{(i)})(1 + \sigma_z^{(j)})/4, \quad (1.10)$$

a cluster state [54] can be created by evolving the system for a time such that  $\int g(t)dt = \pi$ . Cluster states are highly entangled states with the remarkable

property that arbitrary quantum computations can be performed purely via single-qubit measurements along arbitrary axes [55, 56]. A small amount of classical computation is required between measurements. Cluster states can also be defined over qudits [57], and are special cases of the more general class of graph states [58]. Methods have been devised to perform quantum communication [59], error correction [60] and fault-tolerant computation [61] within the cluster state model. Entanglement purification can be used to increase the reliability of cluster state generation [62]. Unlike the adiabatic model however, the cluster state model is yet to lead to any genuinely new algorithms. Given the equivalence of the cluster state model to the circuit model [63], the primary utility of the cluster state model appears to be simpler physical implementation in certain systems such as linear optics [64, 65], and possibly special cases of NV-centers in diamond, quantum dots, and ion traps [66].

#### 1.2.4 Topological quantum computation

The primary difficulty in building a quantum computer is controlling data degradation through interaction with the environment, generally called decoherence. Interaction with the environment can in principle be eliminated by using a topological model of computation. Topological quantum computation was proposed by Kitaev in 1997 [67], and developed further in Ref. [68]. An alternative proposal was given by Freedman in Ref. [69]. Kitaev considered an oriented 2-dimensional lattice of hypothetical particles with many body interactions as shown in Fig. 1.3. The hypothetical particles on each lattice link are related to the 60 permutations of five distinguishable objects  $P_5$ . Certain types of excitations of the lattice are also related to the group  $P_5$ , and exist on lattice sites which correspond to a vertex and face pair

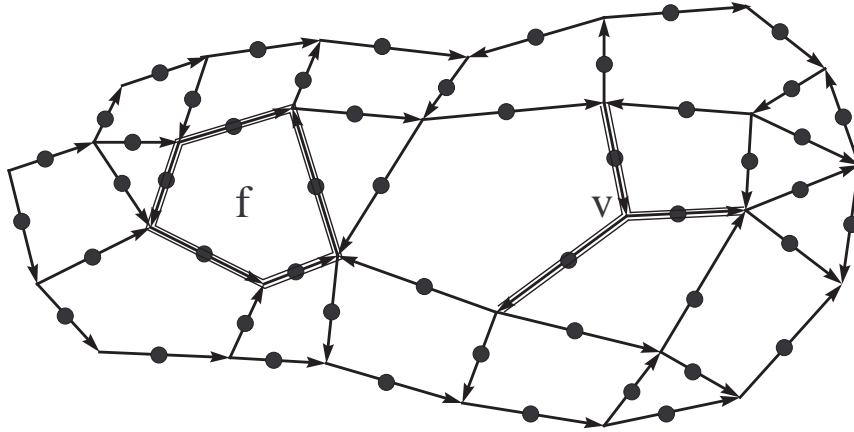


Fig. 1.3: Lattice of hypothetical particles used in the construction of the anyonic model of quantum computation.

as shown in Fig. 1.4. These excitations are called non-Abelian anyons. Of particular interest are pairs of excitations  $|g, g^{-1}\rangle$ . Non-Abelian anyon pairs have the remarkable property that simply moving them through one another effects computation. Given two pairs  $|g, g^{-1}\rangle, |h, h^{-1}\rangle$ , moving  $|g, g^{-1}\rangle$  through  $|h, h^{-1}\rangle$  as shown in Fig. 1.5 creates the state  $|hgh^{-1}, hg^{-1}h^{-1}\rangle$ .

Let  $|0\rangle = |g, g^{-1}\rangle$  and  $|1\rangle = |h, h^{-1}\rangle$ . Find  $x$  such that  $h = xgx^{-1}$ . A quantum inverter can be constructed simply by moving states  $|0\rangle, |1\rangle$  through the ancilla pair  $|x, x^{-1}\rangle$ . More complicated operations can be performed simply in a similar manner, using more ancilla pairs and pull through operations.

At sufficiently low temperature, the only way data can be corrupted in a topological quantum computer is via the spontaneous interaction of two anyons — an event that occurs with probability  $O(e^{-\alpha l})$ , where  $l$  is the minimum separation of any pair of anyons. This probability can be made arbitrarily small simply by keeping the anyons well separated. While this is a desirable property, clearly a computational model based on hypothetical

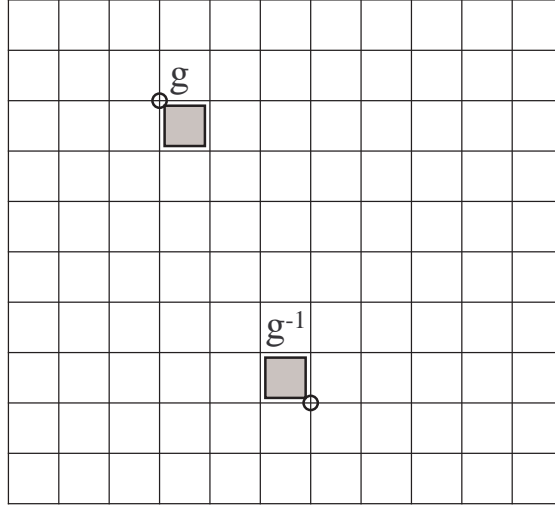


Fig. 1.4: A conjugate pair of non-Abelian anyons.

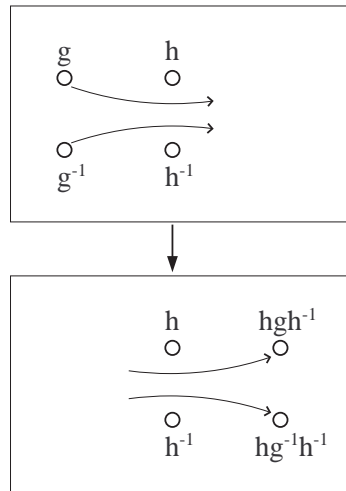


Fig. 1.5: Performing operations in the anyonic model of quantum computation.

particles that do not exist in nature cannot be implemented.

Recently, significant progress has been made on the topological quantum computation model. General schemes using anyons based on arbitrary non-solvable groups [70], and smaller, solvable, non-nilpotent groups [71] have been devised. A less robust but simpler scheme based on Abelian anyons has been proposed [72] and designs for possible experimental realizations are emerging [73, 74]. Experimental proposals based on non-Abelian anyons have also been constructed [75, 76].

### 1.2.5 Geometric quantum computation

The basic idea of geometric quantum computation is illustrated by the Aharonov-Bohm effect [77] in which a particle of charge  $q$  executing a loop around a perfectly insulated solenoid containing flux  $\Phi$  acquires a geometric phase  $e^{iq\Phi}$  [78]. As shown in Fig. 1.6, the phase acquired is insensitive to the exact path taken. This phase shift can be used to build quantum gates [79, 80]. At the moment, there are conflicting numerical and analytic calculations both supporting and attacking the fundamental robustness of geometric quantum computation [81].

## 1.3 Quantum computation is possible in principle

For the remainder of the thesis we will focus on the qubit circuit model. Physical realizations of this model of computation have been proposed in the context of liquid NMR [82], ion traps [83] including optically [84, 85] and physically [86, 87] coupled microtraps, linear optics [88], Josephson junctions utilizing both charge [89, 90] and flux [91] degrees of freedom, quantum dots [92],  $^{31}\text{P}$  in  $^{28}\text{Si}$  architectures utilizing indirectly exchange coupled donor nuclear spins [93], exchange coupled electron spins [94, 95],

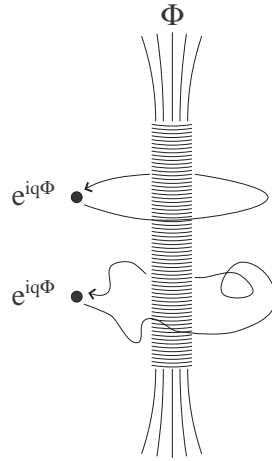


Fig. 1.6: Example of the path independence of the phase shift induced by the Aharonov-Bohm effect. A particle of charge  $q$  executing a loop around a perfectly insulated solenoid containing flux  $\Phi$  acquires a geometric phase  $e^{iq\Phi}$ .

both spins [96, 97], magnetic dipolar coupled electron spins [98] and qubits encoded in the charge distribution of a single electron on two donors [99], deep donors in silicon [100], acceptors in silicon [101], solid-state ensemble NMR utilizing lines of  $^{29}\text{Si}$  in  $^{28}\text{Si}$  [102], electrons floating on liquid helium [103], cavity QED [104, 105], optical lattices [106, 107] and the quantum Hall effect [108]. At the present time, the ion trap approach is the closest to realizing the five basic requirements of scalable quantum computation [109].

The mere existence of quantum computer proposals and quantum algorithms is not sufficient to say that quantum computation is possible in principle. Firstly, almost all quantum algorithms that provide an exponential speed up over the best-known equivalent classical algorithms make use of the quantum Fourier transform which in turn uses exponentially small rotations. For example, in the case of Shor's algorithm, to factor an  $L$ -bit number, in principle single-qubit rotations of magnitude  $2\pi/2^{2L}$  are required. Clearly

this is impossible for large  $L$ .

Coppersmith resolved this issue by showing that most of the small rotations in the quantum Fourier transform could simply be ignored without significantly affecting the output of the circuit. For the specific case of Shor’s algorithm, as described in Chapter 9, we took this work further to show that rotations of magnitude  $\pi/128$  implemented with accuracy  $\pm\pi/512$  were sufficient to factor integers thousands of bits long.

More seriously, quantum systems are inherently fragile. The gamut of relaxation processes, environmental couplings, and even systematic errors induced by architectural imperfections are typically grouped under the heading of decoherence. Ignoring leakage errors in which a qubit is destroyed or placed in a state other than those selected for computation [110], Shor made the surprising discovery that all types of decoherence could be corrected simply by correcting unwanted bit-flips ( $X$ ), phase-flips ( $Z$ ) and both simultaneously ( $XZ$ ) [111]. Shor’s scheme required each qubit of data to be encoded across nine physical qubits. This was the first quantum error correction code (QECC).

Later work by Laflamme gave rise to a 5-qubit QECC [112] — the smallest code that can correct an arbitrary error to one of its qubits [30]. Steane’s 7-qubit code [113], which also only guarantees to correct an arbitrary error to one of its qubits, is, however, more convenient for the purposes of quantum computation. Steane’s code is part of the large class of CSS codes (Calderbank, Shor, Steane) [114], which is in turn part of the very large class of stabilizer codes [115]. Only a few examples such as permutationally invariant codes [116] exists outside the class of stabilizer codes.

To illustrate the utility of the stabilizer formalism, consider a 5-qubit QECC [117] in which we create logical  $|0\rangle$  and  $|1\rangle$  states corresponding to



the superpositions

$$\begin{aligned}
|0_L\rangle &= |00000\rangle + |10010\rangle + |01001\rangle + |10100\rangle \\
&\quad + |01010\rangle - |11011\rangle - |00110\rangle - |11000\rangle \\
&\quad - |11101\rangle - |00011\rangle - |11110\rangle - |01111\rangle \\
&\quad - |10001\rangle - |01100\rangle - |10111\rangle + |00101\rangle, \tag{1.11}
\end{aligned}$$

$$\begin{aligned}
|1_L\rangle &= |11111\rangle + |01101\rangle + |10110\rangle + |01011\rangle \\
&\quad + |10101\rangle - |00100\rangle - |11001\rangle - |00111\rangle \\
&\quad - |00010\rangle - |11100\rangle - |00001\rangle - |10000\rangle \\
&\quad - |01110\rangle - |10011\rangle - |01000\rangle + |11010\rangle. \tag{1.12}
\end{aligned}$$

These superstitions redundantly encode data in such a way that an arbitrary error to any one qubit can be corrected. They are, however, difficult to work with directly. In the stabilizer formalism,  $|0_L\rangle$  and  $|1_L\rangle$  are instead described as simultaneous +1 eigenstates of

$$M_1 = X \otimes Z \otimes Z \otimes X \otimes I \tag{1.13}$$

$$M_2 = I \otimes X \otimes Z \otimes Z \otimes X \tag{1.14}$$

$$M_3 = X \otimes I \otimes X \otimes Z \otimes Z \tag{1.15}$$

$$M_4 = Z \otimes X \otimes I \otimes X \otimes Z \tag{1.16}$$

These operators are called stabilizers. Let  $S$  denote the set of stabilizers (which is the group generated by  $M_1$ – $M_4$ ). Any valid logical state must satisfy  $M|\Psi_L\rangle = |\Psi_L\rangle$  for all  $M \in S$ . This observation allows us to determine which quantum gates can be applied directly to the logical states. Specifically, if we wish to apply  $U$  to our logical state to obtain  $U|\Psi_L\rangle$ , then

since  $UMU^\dagger U|\Psi\rangle$  must be a logical state,  $UMU^\dagger$  must be a stabilizer. If we restrict our attention to gates  $U$  that are products of single-qubit gates, only two single logical qubit gates

$$X_L = X \otimes X \otimes X \otimes X \otimes X \quad (1.17)$$

$$Z_L = Z \otimes Z \otimes Z \otimes Z \otimes Z \quad (1.18)$$

can be applied directly to data encoded using this version of 5-qubit QEC. Note that by restricting our attention to products of single-qubit gates, any error present in one of the qubits of the code before a logical gate operation cannot be copied to other qubits. Any circuit with the property that a single error can cause that most one error in the output is called fault-tolerant.

So far, we have not explained how errors are corrected using a QECC. Given a potentially erroneous state  $|\Psi'\rangle$ , one way of locating any errors is to check whether  $|\Psi'\rangle$  is still a +1 eigenstate of each of the stabilizers. Any errors so located can then be manually corrected. This method is described in some detail in Chapter 10.

We now have basic single logical qubit gates and error correction. To achieve universal quantum computation we need to be able to couple logical qubits and perform arbitrary single logical qubits gates [28, 29]. Unfortunately, the 5-qubit QECC does not readily permit multiple logical qubits to be coupled, though a complicated three logical qubit gate does exist [118]. For universal quantum computation, the 7-qubit Steane code, or indeed any of the CSS codes, is more appropriate as they permit a simple transversal implementation of logical CNOT as shown in Fig. 1.7. The 7-qubit Steane code also permits similar transversal single-qubit gates  $H$ ,  $X$ ,  $Z$ ,  $S$  and  $S^\dagger$  (see Fig. 10.2). These are, however, insufficient to construct arbitrary

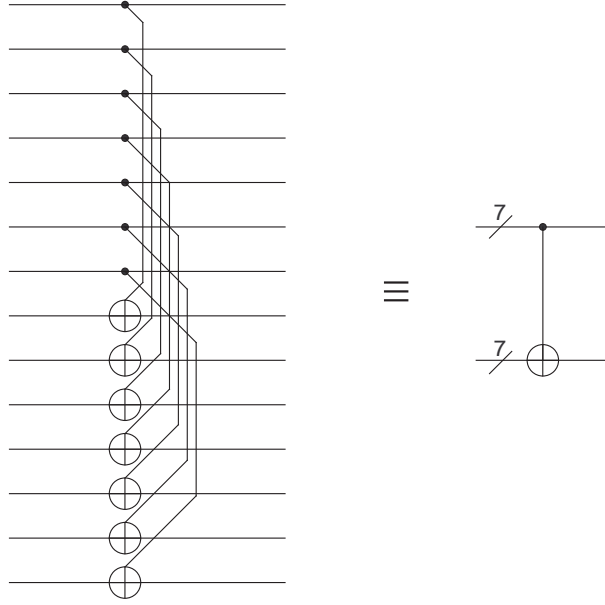


Fig. 1.7: 7-qubit transversal logical CNOT gate.

single-qubit rotations of the form

$$\begin{pmatrix} \cos(\theta/2)e^{i(\alpha+\beta)/2} & \sin(\theta/2)e^{i(\alpha-\beta)/2} \\ -\sin(\theta/2)e^{i(-\alpha+\beta)/2} & \cos(\theta/2)e^{i(-\alpha-\beta)/2} \end{pmatrix}. \quad (1.19)$$

An additional gate such as the  $T$ -gate is required to construct arbitrary single-qubit gates. The simplest fault-tolerant implementation of the  $T$ -gate we have been able to devise still requires an additional 12 ancilla qubits, and at least 93 gates, 45 resets and 17 measurements arranged on a circuit of depth at least 92 and is described in detail in Chapter 10. By virtue of the fact that the operation  $HT$  corresponds to the rotation of a qubit by an angle that is an irrational number, and the fact that repeated rotation by an irrational number enables arbitrarily close approximation of a rotation of any angle, the pair of single-qubit gates  $H$ ,  $T$  is sufficient to approximate an arbitrary single-qubit rotation arbitrarily accurately. In practice, it is

better to use the 23 unique combinations of  $H$ ,  $X$ ,  $Z$ ,  $S$  and  $S^\dagger$  in addition to the  $T$ -gate since, for example, the logical  $X$ -gate is vastly simpler to implement than  $HTTTTH$ . The existence of efficient sequences of gates to approximate arbitrary unitary rotations in general, and single-qubit gates in particular, is guaranteed by the Solovay-Kitaev theorem [119, 120, 30, 121]. The exact length of such sequences required to achieve a given accuracy is discussed in Chapter 10.

We now have enough machinery to consider arbitrarily large, arbitrarily reliable quantum computation. Suppose every qubit in our computer has probability  $p$  of suffering an error per unit time, where unit time refers to the amount of time required to implement the slowest fundamental gate (not logical gate). Consider a circuit consisting of the most complicated fault-tolerant logic gate, the  $T$ -gate, followed by quantum error correction. By virtue of being fault-tolerant, this circuit can only fail to produce useful output if at least two errors occur. For some constant  $c$ , and sufficiently low error rate  $p$ , the probability of failure of the structure is thus  $cp^2$ . Since we have chosen the most complicated gate, every other fault-tolerant gate followed by error correction, including the identity  $I$  (do nothing) gate, has probability of failure at most  $cp^2$ .

Consider an arbitrary quantum circuit expressed in terms of the fundamental gates CNOT,  $I$ ,  $H$ ,  $X$ ,  $Z$ ,  $S$ ,  $S^\dagger$ , their products, and  $T$  (no QEC at this stage). In the worst-case, if an error anywhere causes the circuit to fail, the probability of success of such a circuit is  $(1 - p)^{qt}$  where  $q$  is the number of qubits and  $t$  the number of time steps. By replacing each gate with an error corrected fault-tolerant structure, this can be reduced to  $(1 - cp^2)^{qt}$ . Note that the new circuit is still expressed entirely in terms of the allowed gates and measurement. We can therefore repeat the process and replace

these gates in turn with error corrected fault-tolerant structures giving an overall reliability of  $(1 - c^3 p^4)^{qt}$ . If we repeat this  $k$  times we find that the overall circuit reliability is

$$\left(1 - \frac{(cp)^{2k}}{c}\right)^{qt}. \quad (1.20)$$

Clearly, provided the error rate per time step is less than  $p_{th} = 1/c$  and we have sufficient resources, an arbitrarily large quantum computation can be performed arbitrarily reliably. This is the threshold theorem of quantum computation [122]. Note that the greater the amount  $p < p_{th}$ , the fewer levels of error correction that are required. Despite the lack of a definitive reference,  $p_{th}$  is frequently assumed to be  $10^{-4}$ .

Substantial customization and optimization of the threshold theorem has occurred over the years. As described, the threshold theorem requires the ability to interact arbitrarily distant pairs of qubits in parallel, fast measurement gates, and fast and reliable classical computation. A detailed study of the impact of noisy long-range communication has been performed yielding threshold error rates  $\sim 10^{-4}$  for a variety of assumptions [123]. Modifications removing the need for measurement and classical processing but still requiring error-free long-range interactions have been devised at the cost of greatly increased resources [124], though subsequent work has substantially reduce the complexity of the required quantum circuitry with a threshold  $p_{th} = 2.4 \times 10^{-6}$  obtained under the additional assumption that the quantum computer consists of a single line qubits with nearest neighbor interactions only [125].

By using a much simplified error correction scheme devised by Steane [126] that works on any CSS code, and using larger QECCs and less concate-

nation, encouragingly high thresholds  $\sim 10^{-3}$  [127] and even  $9 \times 10^{-3}$  [128] have been calculated, although in the latter case only under the assumption that errors occur after gates, not to idle qubits, and in both cases long-range interactions must be available.

An alternative approach is to perform computation by interacting data with specially prepared ancilla states [129, 130], a method called postselected quantum computing. While the resources required to prepare sufficiently reliable ancilla states are prohibitive, in principle this approach permits arbitrarily large computations to be performed provided  $p < p_{th} = 0.03$  [131].

#### 1.4 Overview

The primary goal of this thesis is to relax the theoretical resource requirements required for large-scale quantum computation. Much of our work is motivated by the Kane  $^{31}\text{P}$  in  $^{28}\text{Si}$  architecture in which fast and reliable measurement and classical processing is difficult to achieve, and qubits may be limited to a single line with nearest neighbor interactions only.

In Chapters 2–3, the viability of the adiabatic Kane CNOT gate and read-out operation are assessed. Chapter 4 reviews a technique of constructing efficient 2-qubit gates. A greatly simplified non-fault-tolerant linear nearest neighbor implementation of 5-qubit quantum error correction is presented in Chapter 5, and further modified to remove the need for measurement and classical processing in Chapter 6. Chapter 7 provides a detailed review of Shor’s algorithm, followed by a linear nearest neighbor circuit implementation in Chapter 8. Chapter 9 focuses on removing the need for exponentially small rotations in circuit implementations of Shor’s algorithm. Finally, Chapter 10 presents a method of constructing arbitrary single-qubit fault-

---

tolerant gates, and applies this to the specific case of the remaining rotation gates required by Shor's algorithm. Chapter 11 contains concluding remarks and summarizes the results of the thesis. Chapters 2, 3, 5, 8 and 9 have been published in [132, 133, 134, 135, 136] respectively.





## 2. The adiabatic Kane CNOT gate

The spins of the  $^{31}\text{P}$  nucleus and donor electron in bulk  $^{28}\text{Si}$  have extremely long coherence times [137, 138]. Consequently, a number of quantum computer proposals have been based on this system [93, 97, 98, 95]. In this chapter and Chapter 3, we focus on Kane’s 1998 proposal [93] which calls for a line of single  $^{31}\text{P}$  atoms spaced approximately 20nm apart [139, 140]. The spin of each phosphorus nucleus is used as a qubit and the donor electron used to couple to neighboring qubits. Neglecting readout mechanisms for the moment, each qubit requires at least two electrodes to achieve single- and 2-qubit gates. The extent to which the presence and operation of these electrodes will reduce the system’s coherence times is unknown. We therefore study the error rate of the Kane CNOT gate as a function of the coherence times to determine their approximate minimum acceptable values. We find that the coherence times required to achieve a CNOT error rate of  $10^{-4}$  are a factor of 6 less than those already observed experimentally.

The chapter is organized as follows. In Section 2.1, the Kane architecture is briefly described followed by the method of performing a CNOT in Section 2.2. In Section 2.3, the technique we used to model finite coherence times is presented along with contour plots of the CNOT error rate as a function of the coherence times. In Section 2.4, we discuss the implications of our results.

### 2.1 The Kane architecture

Ignoring readout mechanisms, which we discuss in Chapter 3, the basic layout of the adiabatic Kane phosphorus in silicon solid-state quantum computer [93, 96] is shown in Fig. 2.1. The phosphorous donor electrons are used primarily to mediate interactions between neighboring nuclear spin qubits. As such, the donor electrons are polarized to remove their spin degree of freedom. This can be achieved by maintaining a steady  $B_z = 2\text{T}$  at around  $T = 100\text{mK}$  [141]. Techniques for relaxing the high field and low temperature requirements such as spin refrigeration are under investigation [96].

In addition to the potential to build on the vast expertise acquired during the last 50 years of silicon integrated circuit development, the primary attraction to the Kane architecture, and  $^{31}\text{P}$  in  $^{28}\text{Si}$  architectures in general, is their extraordinarily long spin coherence times [137, 138]. Four quantities are of interest — the relaxation ( $T_1$ ) and dephasing ( $T_2$ ) times of both the donor electron and nucleus. Both times only have meaning when the system is in a steady magnetic field. Assuming the field is parallel with the z-axis, the relaxation time refers to the time taken for  $1/e$  of the spins in the sample to spontaneously flip whereas the dephasing time refers to the time taken for the  $x$  and  $y$  components of a single spin to decay by a factor of  $1/e$ . Existing experiments cannot measure  $T_2$  directly, but instead a third quantity  $T_2^*$  which is the time taken for the  $x$  and  $y$  components of an ensemble of spins to decay by a factor of  $1/e$ . Since  $T_2^* \leq T_2$  [142], we can use experimental values  $T_2^*$  as a lower bound for  $T_2$ .

In natural silicon containing 4.7%  $^{29}\text{Si}$ , relaxation times  $T_1$  in excess 1 hour have been observed for the donor electron at  $T = 1.25\text{K}$  and  $B \sim 0.3\text{T}$  [137]. The nuclear relaxation time has been estimated at over 80 hours in similar conditions [143]. These times are so long that we will ignore relax-

ation in our simulations of gate reliability. The donor electron dephasing time  $T_2^*$  in enriched  $^{28}\text{Si}$  containing less than 50ppm  $^{29}\text{Si}$ , at 7K and donor concentration  $0.8 \times 10^{15}$  has been measured to be 14ms [138]. Extrapolation to a single donor suggests  $T_2 = 60\text{ms}$  at 7K. An even longer  $T_2$  is expected at lower temperatures. At the time of writing, to the authors' knowledge, no experimental data relating to the nuclear dephasing time has been obtained. However, considering the much greater isolation from the environment of the nuclear spin, this time is expected to be much larger than the electron dephasing time.

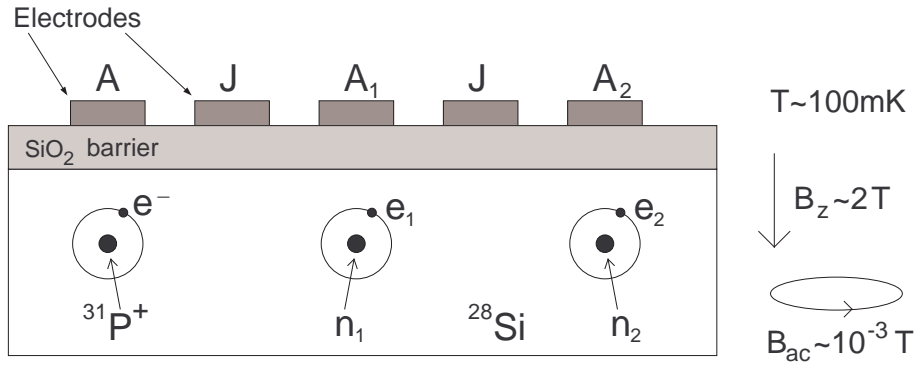


Fig. 2.1: Schematic of the Kane architecture. The rightmost two qubits show the notation to be used when discussing the CNOT gate.

Control of the nuclear spin qubits is achieved via electrodes above and between each phosphorus atom and global transverse oscillating fields of magnitude  $\sim 10^{-3}\text{T}$ . To selectively manipulate a single qubit, the  $A$ -electrode above it is biased. A positive/negative bias draws/drives the donor electron away from the nucleus, in both cases reducing the magnitude of the hyperfine interaction. This in turn reduces the energy difference between nuclear spin up ( $|0\rangle$ ) and down ( $|1\rangle$ ) allowing this transition to be brought into resonance with a globally applied oscillating magnetic field. Depending on the timing

of the  $A$ -electrode bias, an arbitrary rotation about an axis in the  $x$ - $y$  plane can be implemented [144]. By utilizing up to three such rotations, a qubit can be rotated into an arbitrary superposition  $\alpha|0\rangle + \beta|1\rangle$ .

Biasing an  $A$ -electrode above a particular donor will also effect neighboring and more distant donors. It is likely that compensatory biasing of nearby electrodes will be required to ensure non-targeted qubits remain off resonant. Subject to this restriction, there is no limit to the number of simultaneous single-qubit rotations that can be implemented throughout a Kane quantum computer.

Interactions between neighboring qubits are governed by the  $J$ -electrodes. A positive bias encourages greater overlap of the donor electron wave functions leading to indirect coupling of their associated nuclei. In analogy to the single-qubit case, this allows multiple 2-qubit gates to be performed selectively between arbitrary neighbors. A discussion of the electrode pulses required to implement a CNOT is given in the next section.

## 2.2 Adiabatic CNOT pulse profiles

Performing a CNOT gate on an adiabatic Kane QC is an involved process described in detail in [141]. Given the high field (2T) and low temperature (100mK) operating conditions, we can model the behavior of the system with a spin Hamiltonian. Only two qubits are required to perform a CNOT, so for the remainder of the chapter we will restrict our attention to a computer with just two qubits. The basic notation is shown in the right half of Fig. 2.1. Furthermore, let  $\sigma_{n1}^z \equiv \sigma^z \otimes I \otimes I \otimes I$ ,  $\sigma_{e1}^z \equiv I \otimes \sigma^z \otimes I \otimes I$ ,  $\sigma_{n2}^z \equiv I \otimes I \otimes \sigma^z \otimes I$  and  $\sigma_{e2}^z \equiv I \otimes I \otimes I \otimes \sigma^z$  where  $I$  is the  $2 \times 2$  identity matrix,  $\sigma^z$  is the usual Pauli matrix and  $\otimes$  denotes the matrix outer product. With these definitions the meaning of terms such as  $\sigma_{n2}^y$  and  $\vec{\sigma}_{e1}$  should

be self evident.

Let  $g_n$  be the g-factor for the phosphorus nucleus,  $\mu_n$  the nuclear magneton and  $\mu_B$  the Bohr magneton. The Hamiltonian can be broken into three parts

$$H = H_Z + H_{\text{int}}(t) + H_{\text{ac}}(t). \quad (2.1)$$

The Zeeman energy terms are contained in  $H_Z$

$$H_Z = -g_n\mu_n B_z(\sigma_{n1}^z + \sigma_{n2}^z) + \mu_B B_z(\sigma_{e1}^z + \sigma_{e2}^z). \quad (2.2)$$

The contact hyperfine and exchange interaction terms, both of which can be modified via the electrode potentials are

$$H_{\text{int}}(t) = A_1(t)\vec{\sigma}_{n1} \cdot \vec{\sigma}_{e1} + A_2(t)\vec{\sigma}_{n2} \cdot \vec{\sigma}_{e2} + J(t)\vec{\sigma}_{e1} \cdot \vec{\sigma}_{e2}, \quad (2.3)$$

where  $A_i(t) = 8\pi\mu_B g_n \mu_n |\Phi_i(0, t)|^2/3$ ,  $|\Phi_i(0, t)|$  is the magnitude of the wavefunction of donor electron  $i$  at phosphorous nucleus  $i$  at time  $t$ , and  $J(t)$  depends on the overlap of the two donor electron wave functions. The dependence of these quantities on their associated electrode voltages is a subject of ongoing research [145, 146, 147, 148, 139, 140], though it appears atomic precision placement of the phosphorus donors is required due to strong oscillatory dependence of the exchange interaction strength on the distance and direction of separation of donors. For our purposes, it is sufficient to ignore the exact voltage required and assume that the hyperfine and exchange interaction energies  $A_i$  and  $J$  are directly manipulable.

The last part of the Hamiltonian contains the coupling to a globally

applied oscillating field of magnitude  $B_{\text{ac}}(t)$ .

$$\begin{aligned} H_{\text{ac}}(t) = & B_{\text{ac}}(t) \cos(\omega t) [-g_n \mu_n (\sigma_{n1}^x + \sigma_{n2}^x) + \mu_B (\sigma_{e1}^x + \sigma_{e2}^x)] \\ & + B_{\text{ac}}(t) \sin(\omega t) [-g_n \mu_n (\sigma_{n1}^y + \sigma_{n2}^y) + \mu_B (\sigma_{e1}^y + \sigma_{e2}^y)]. \end{aligned} \quad (2.4)$$

Using the above definitions, only the quantities  $A_1$ ,  $J$  and  $B_{\text{ac}}$  need to be manipulated to perform a CNOT gate.

For clarity, assume the computer is initially in one of the states  $|00\rangle$ ,  $|01\rangle$ ,  $|10\rangle$  or  $|11\rangle$  and that we wish to perform a CNOT gate with qubit 1 (the left qubit) as the control. The necessary profiles are shown in Fig. 2.2. Step one is to break the degeneracy of the two qubits' energy levels to allow the control and target qubits to be distinguished. To make qubit 1 the control, the value of  $A_1$  is increased (qubit 1 will be assumed to be the control qubit for the remainder of the chapter).

Step two is to gradually apply a positive potential to the  $J$ -electrode in order to force greater overlap of the donor electron wave functions and hence greater (indirect) coupling of the underlying nuclear qubits. The rate of this change is limited so as to be adiabatic — qubits initially in energy eigenstates remain in energy eigenstates throughout this step. This point shall be discussed in more detail shortly.

Let  $|\text{symm}\rangle$  and  $|\text{anti}\rangle$  denote the standard symmetric and antisymmetric superpositions of  $|10\rangle$  and  $|01\rangle$ . Step three is to adiabatically reduce the  $A_1$  coupling back to its initial value once more. During this step, anti-level-crossing behavior changes the input states  $|10\rangle \rightarrow |\text{symm}\rangle$  and  $|01\rangle \rightarrow |\text{anti}\rangle$ .

Step four is the application of an oscillating field  $B_{\text{ac}}$  resonant with the  $|\text{symm}\rangle \leftrightarrow |11\rangle$  transition. This oscillating field is maintained until these two states have been interchanged. Steps five to seven are the time reverse of steps one to three. Note that steps one and seven (the increasing and

decreasing of  $A_1$ ) appear instantaneous in Fig. 2.2 as the only limit to their speed is that they be done in a time much greater than  $\hbar/0.01\text{eV} \sim 0.1\text{ps}$  where  $0.01\text{eV}$  is the orbital excitation energy of the donor electron.

In principle, the adiabatic steps should be performed slowly to achieve maximum fidelity. In practice, slow gates are more vulnerable to decoherence. To resolve this conflict, consider the degree to which the evolution of a given  $H(t)$  deviates from perfect adiabaticity [149]

$$\Theta(t) \equiv \text{Max}_{a \neq b} \left[ \frac{\hbar |\langle \psi_a(t) | \frac{\partial}{\partial t} (H(t)) | \psi_b(t) \rangle|}{(\langle \psi_a(t) | H(t) | \psi_a(t) \rangle - \langle \psi_b(t) | H(t) | \psi_b(t) \rangle)^2} \right]. \quad (2.5)$$

Ignoring decoherence for the moment, for high fidelity it is necessary that  $\Theta(t) \ll 1$ . The states  $|\psi_a(t)\rangle$  are the eigenstates of  $H(t)$ . To a certain extent, it is possible to reduce  $\Theta(t)$  without increasing the duration of a step by optimizing the profiles of the adiabatically varying parameters in  $H(t)$ . In the case of the adiabatic Kane CNOT, this means optimizing the profiles of  $A_1(t)$  and  $J(t)$ .

Various profiles for the adiabatic steps in the CNOT procedure have been investigated in [150]. In Fig. 2.3, we have plotted three possible  $J(t)$  profiles for step two of the CNOT gate. The function  $\Theta(t)$  for each profile is shown in Fig. 2.4. Profile 1 is a simple linear pulse. Profile 2 can be seen to be the best of the three and is described by  $J(t) = 810\alpha(1 - \text{sech}(5t/\tau))$  where  $\tau = 9\mu\text{s}$  is the duration of the pulse and  $\alpha = 1.0366$  is a factor introduced to ensure that  $J(\tau) = 810$ . The third profile

$$J(t) = \begin{cases} \frac{J_{max}}{2} \frac{t(1+\pi/2)}{\tau}, & 0 < t < \tau/(1+\pi/2) \\ \frac{J_{max}}{2} \left[ 1 + \sin \left( \frac{\pi}{2} \frac{t-\tau/(1+\pi/2)}{\tau/(1+2/\pi)} \right) \right], & \tau/(1+\pi/2) < t < \tau \end{cases} \quad (2.6)$$

is a composite linear-sinusoidal profile that was used in the calculations pre-

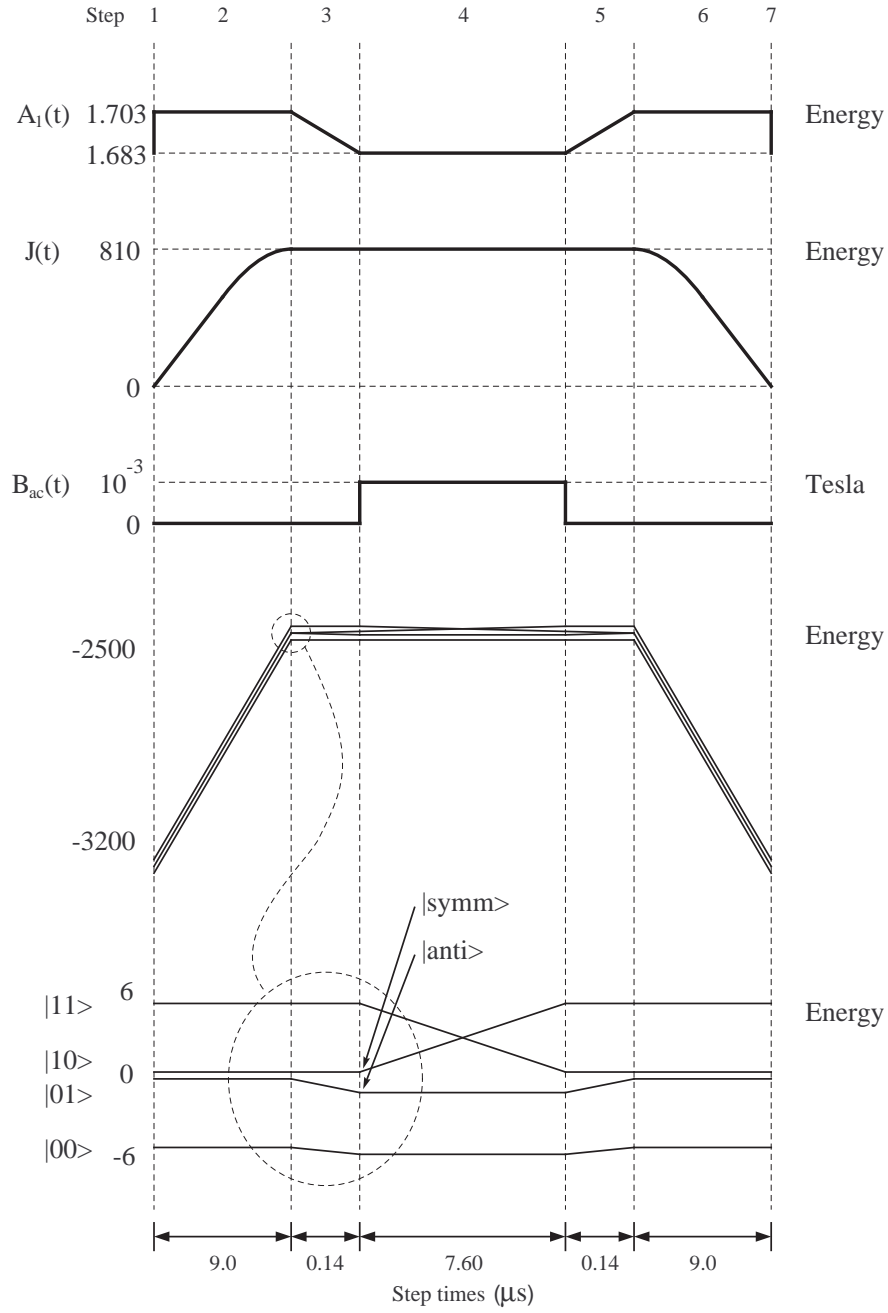


Fig. 2.2: Gate profiles and state energies during a CNOT gate in units of  $g_n\mu_n B_z = 7.1 \times 10^{-5}\text{meV}$ .



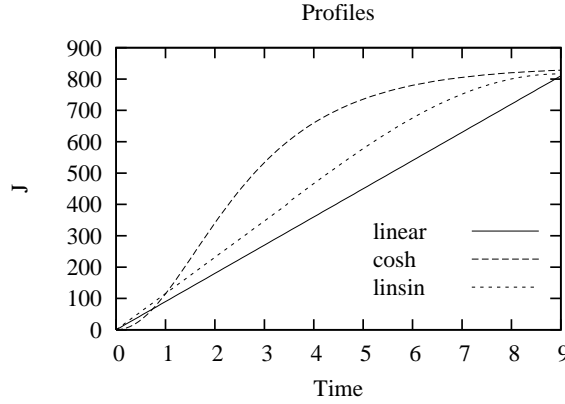


Fig. 2.3: Possible forms of the  $J(t)$  profile for step 2 of the adiabatic CNOT gate.  $J(t)$  is in units of  $g_n\mu_n B_z = 7.1 \times 10^{-5}\text{meV}$ .

sented in this chapter due to numerical difficulties in solving the Schrödinger equation for profile 2. The advantage of the second two profiles over the linear one is that they flatten out as  $J$  approaches 810. At  $J = 816.65$ , the system undergoes a level crossing. To maintain adiabatic evolution,  $J(t)$  needs to change more slowly near this value. Note that the reason it is desirable to make  $J(t)$  so large is to ensure that there is a large energy difference between  $|\text{symm}\rangle$  and  $|\text{anti}\rangle$  during step 4 (the application of  $B_{\text{ac}}$ ). This difference is given by

$$\delta E = 2A^2 \left( \frac{1}{\mu_B B_z + g_n \mu_n B_z} - \frac{1}{\mu_B B_z + g_n \mu_n B_z - 2J} \right). \quad (2.7)$$

Without a large energy difference, the oscillating field  $B_{\text{ac}}$  which is set to resonate with the transition  $|\text{symm}\rangle \leftrightarrow |11\rangle$  will also be very close to resonant with  $|\text{anti}\rangle \leftrightarrow |11\rangle$  causing a large error during the operation of the CNOT gate. This source of error can be further reduced by using a weaker  $B_{\text{ac}}$  at the cost of slower gate operation.

Step 3 (the decreasing of  $A_1$ ) could be performed without degrading the

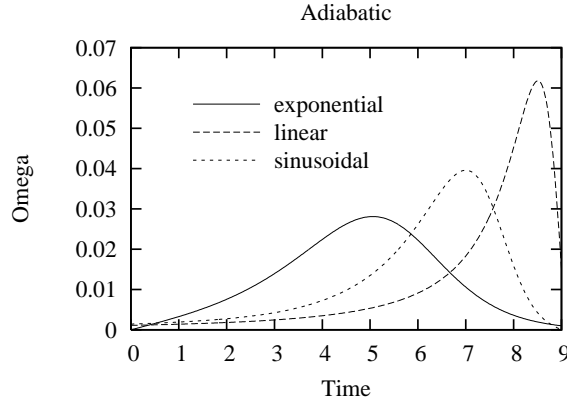


Fig. 2.4: The adiabatic measure  $\Theta(t)$  for each  $J(t)$  profile.

overall fidelity of the gate in a time of less than a micro-second with a linear pulse profile.

The above steps were simulated using an adaptive Runge-Kutta routine to solve the density matrix form of the Schrödinger equation

$$\dot{\rho}(t) = \frac{1}{i\hbar}[H(t), \rho(t)] \quad (2.8)$$

in the computational basis  $|n_1 e_1 n_2 e_2\rangle$ . The times used for each stage were as follows

stage	duration ( $\mu s$ )
2	9.0000
3	0.1400
4	7.5989
5	9.0000
6	0.1400

Note that the precision of the duration of stage 4 is required as the oscillating field  $B_{ac}$  induces the states  $|11\rangle$  and  $|\text{symm}\rangle$  to swap smoothly

back and forth. The duration  $7.5989\mu s$  is the time required for one swap at  $B_{ac} = 10^{-3}T$ .

The other step times were obtained by first setting them to arbitrary values ( $\sim 5\mu s$ ) and increasing them until the gate fidelity ceased to increase. The step times were then decreased one by one until the fidelity started to decrease. As such, the above times are the minimum time in which the maximum fidelity can be achieved. This maximum fidelity was found to be  $5 \times 10^{-5}$  for all computation basis states.

### 2.3 Intrinsic dephasing and fidelity

In this chapter and Chapter 3, dephasing is modelled as exponential decay of the off diagonal components of the density matrix. While a large variety of more detailed dephasing models exist [151, 152, 153, 154, 155, 156], the chosen method is consistent with the observed experimental behavior of dephasing in solid-state systems [142]. The donor electrons and phosphorous nuclei are assumed to dephase at independent rates. With the inclusion of dephasing terms, Eq. (2.8) becomes

$$\begin{aligned} \dot{\rho} = & \frac{1}{i\hbar}[H, \rho] \\ & -\Gamma_e[\sigma_{e_1}^z, [\sigma_{e_1}^z, \rho]] - \Gamma_e[\sigma_{e_2}^z, [\sigma_{e_2}^z, \rho]] \\ & -\Gamma_n[\sigma_{n_1}^z, [\sigma_{n_1}^z, \rho]] - \Gamma_n[\sigma_{n_2}^z, [\sigma_{n_2}^z, \rho]]. \end{aligned} \quad (2.9)$$

To understand the effect of each double commutator, it is instructive to consider the following simple mathematical example :

$$\dot{M} = -\Gamma[\sigma^z, [\sigma^z, M]]$$

$$\begin{pmatrix} \dot{m}_{11} & \dot{m}_{12} \\ \dot{m}_{21} & \dot{m}_{22} \end{pmatrix} = \begin{pmatrix} 0 & -4\Gamma m_{12} \\ -4\Gamma m_{21} & 0 \end{pmatrix}$$

$$\begin{pmatrix} m_{11}(t) & m_{12}(t) \\ m_{21}(t) & m_{22}(t) \end{pmatrix} = \begin{pmatrix} m_{11}(0) & m_{12}(0)e^{-4\Gamma t} \\ m_{21}(0)e^{-4\Gamma t} & m_{22}(0) \end{pmatrix}. \quad (2.10)$$

Thus each double commutator in Eq. (2.9) exponentially decays its associated off diagonal elements with characteristic time  $\tau_e = 1/4\Gamma_e$  or  $\tau_n = 1/4\Gamma_n$ .

For each initial state  $|00\rangle$ ,  $|01\rangle$ ,  $|10\rangle$  and  $|11\rangle$ , Eq. (2.9) was solved for a range of values of  $\tau_e$  and  $\tau_n$  using the pulse profiles described in Section 2.2 allowing a contour plot of the gate error versus  $\tau_e$  and  $\tau_n$  to be constructed (Figs 2.5–2.6). Note that each contour is a double line as each run of the simulation required considerable computational time and the data available does not allow finer delineation of exactly where each contour is. The worst case error of all input states as a function of  $\tau_e$  and  $\tau_n$  is shown in Fig. 2.7.

## 2.4 Conclusion

Fig. 2.7 suggests that it would be acceptable for the dephasing times of the phosphorus donor electron and nuclei to be 10ms and 0.5s respectively if a CNOT reliability of  $10^{-4}$  was desired. Given that the current best estimate of the donor electron dephasing time is 60ms [138], and assuming that the nuclear dephasing time is at least a factor of 80 longer again, as for the case of the relaxation times, it would be acceptable for the presence of the silicon dioxide barrier, gate electrodes, and other control structures to reduce the dephasing times by a factor of 6 without impacting on the desired reliability of the gate.

Since the publication of this work [132], simpler and faster methods of

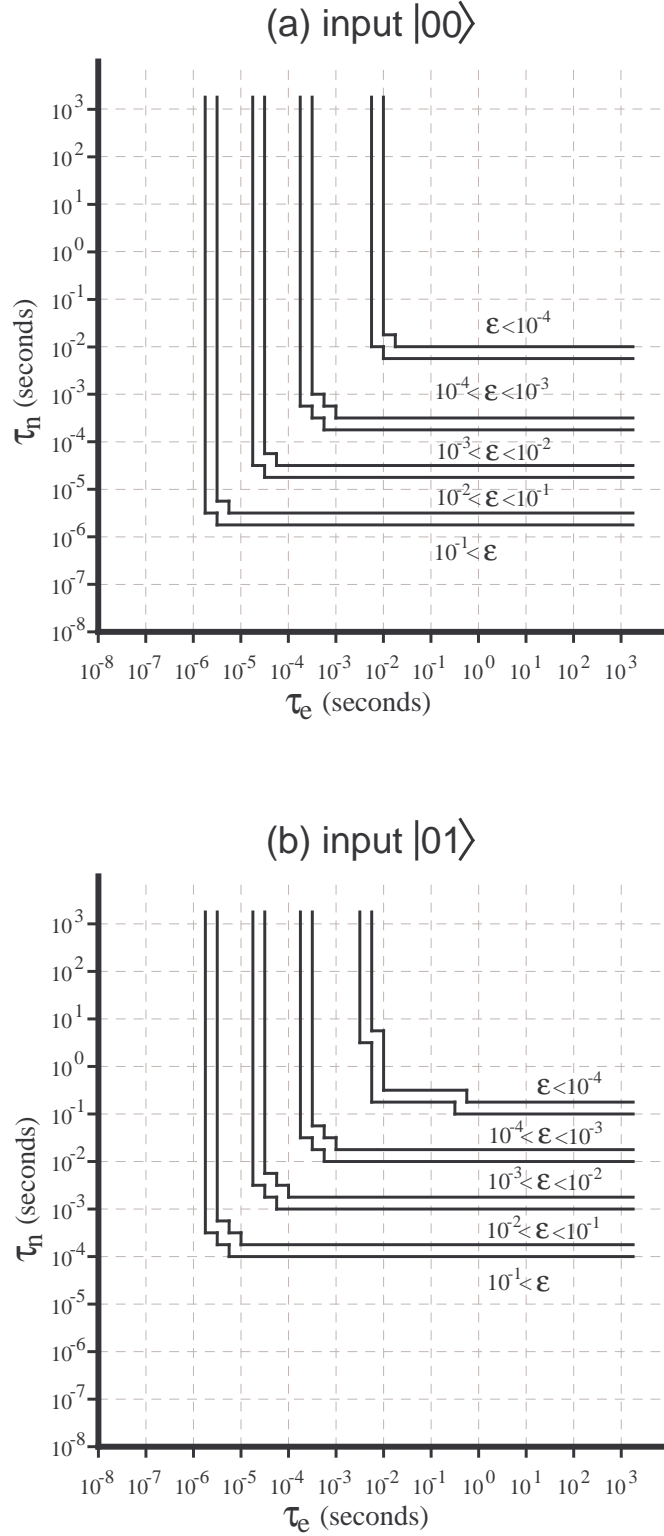


Fig. 2.5: Probability of error  $\varepsilon$  during a CNOT gate as a function of  $\tau_e$  and  $\tau_n$  for input state (a)  $|00\rangle$  and (b)  $|01\rangle$ . The first qubit is the control.

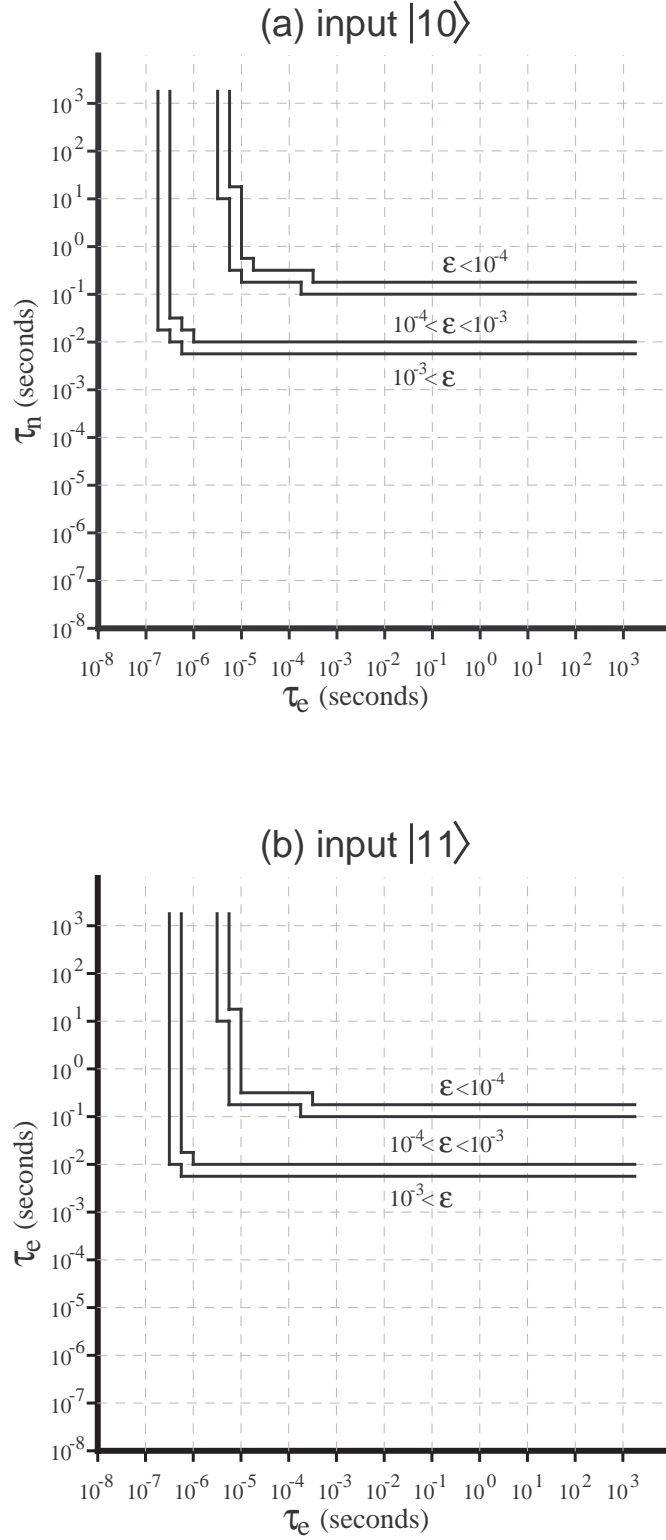


Fig. 2.6: Probability of error  $\varepsilon$  during a CNOT gate as a function of  $\tau_e$  and  $\tau_n$  for input state (a)  $|10\rangle$  and (b)  $|11\rangle$ . The first qubit is the control.

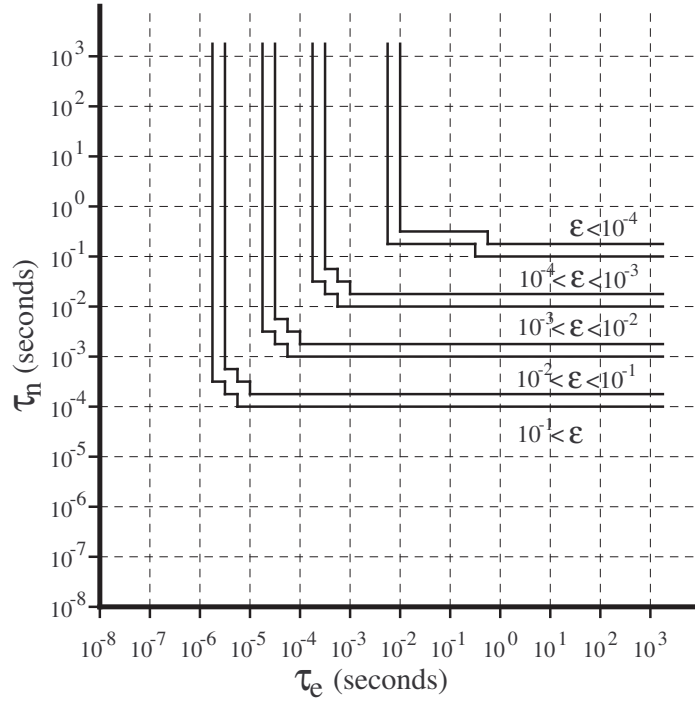


Fig. 2.7: The worst case probability of error  $\varepsilon$  during a CNOT gate as a function of  $\tau_e$  and  $\tau_n$  for all input states.

implementing gates in the Kane architecture have been devised [144], though they are slightly more vulnerable to decoherence [157]. An interesting avenue of further work would be to similarly analyze 2-qubit gates in the context of three electron spin encoded qubits which enable arbitrary computations to be performed utilizing the exchange interaction only [158], thereby eliminating the need for oscillating magnetic fields and resulting in much faster gates.





### 3. Adiabatic Kane single-spin readout

Meaningful quantum computation can not occur without qubit readout. In this chapter, we assess the viability of the adiabatic Kane single-spin readout proposal [93] when dephasing and other effects such as finite exchange coupling control are taken into account. We find that there are serious barriers to the implementation of the proposal, and briefly review alternatives under active investigation.

The evolution of the hyperfine and exchange interaction strengths required to implement readout is reviewed in Section 3.1. The performance of the scheme is described in Section 3.2. Section 3.3 summarizes our results and points to alternative approaches to readout.

#### 3.1 *Adiabatic readout pulse profiles*

The geometry of the adiabatic Kane readout proposal is shown in Fig. 3.1. The basic idea is to raise  $A_1$  to distinguish the qubits, and apply appropriate voltages to induce the evolution of the hyperfine and exchange interaction strengths as shown in Fig. 3.2. This evolution passes through a level crossing resulting in the conversion of states [141]

$$|\downarrow\downarrow\rangle|11\rangle \rightarrow |\downarrow\downarrow\rangle|11\rangle, \quad (3.1)$$

$$|\downarrow\downarrow\rangle|10\rangle \rightarrow |\downarrow\downarrow\rangle|s_n\rangle, \quad (3.2)$$

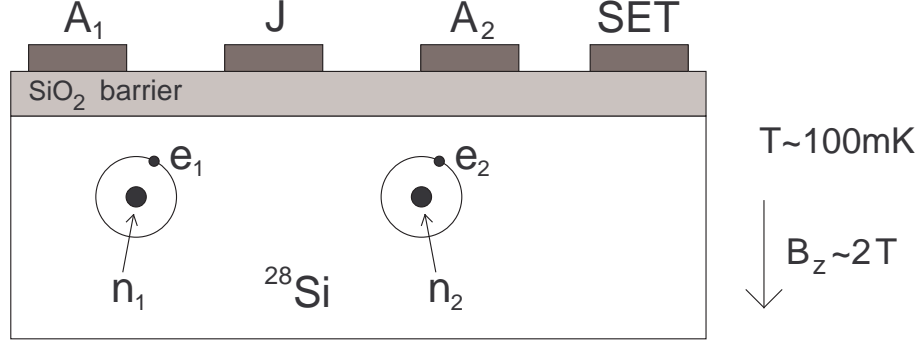


Fig. 3.1: Geometry of adiabatic Kane readout.

$$|\downarrow\downarrow\rangle|01\rangle \rightarrow |a_e\rangle|11\rangle, \quad (3.3)$$

$$|\downarrow\downarrow\rangle|00\rangle \rightarrow |a_e\rangle|a_n\rangle, \quad (3.4)$$

where  $|\downarrow\rangle$  denotes a spin-down electron,  $|a_e\rangle$  denotes the antisymmetric superposition of the two electrons, and similarly for  $|s_n\rangle$  and  $|a_n\rangle$ . Note that if qubit 1 is in state  $|1\rangle$  ( $|0\rangle$ ) the final electron state will be  $|\downarrow\downarrow\rangle$  ( $|a_e\rangle$ ).

By converting the nuclear spin information into electron spin information in this manner, in principle we can apply a potential difference to the  $A_1$  and  $A_2$ -electrodes and, by virtue of the Pauli exclusion principle, use the SET (single electron transistor) to observe tunnelling of electron 1 onto donor 2 if and only if the nuclear spin was  $|0\rangle$ .

### 3.2 Readout performance

In exactly the same manner as Chapter 2, the performance of the adiabatic state conversion stage of readout was simulated with variable nuclear and electronic dephasing times  $\tau_n$  and  $\tau_e$ . The results of these simulations are shown in Figs. 3.3–3.4 and show strong dependence on the initial computational basis state. Indeed, we found the basis state  $|11\rangle$  to be immune to

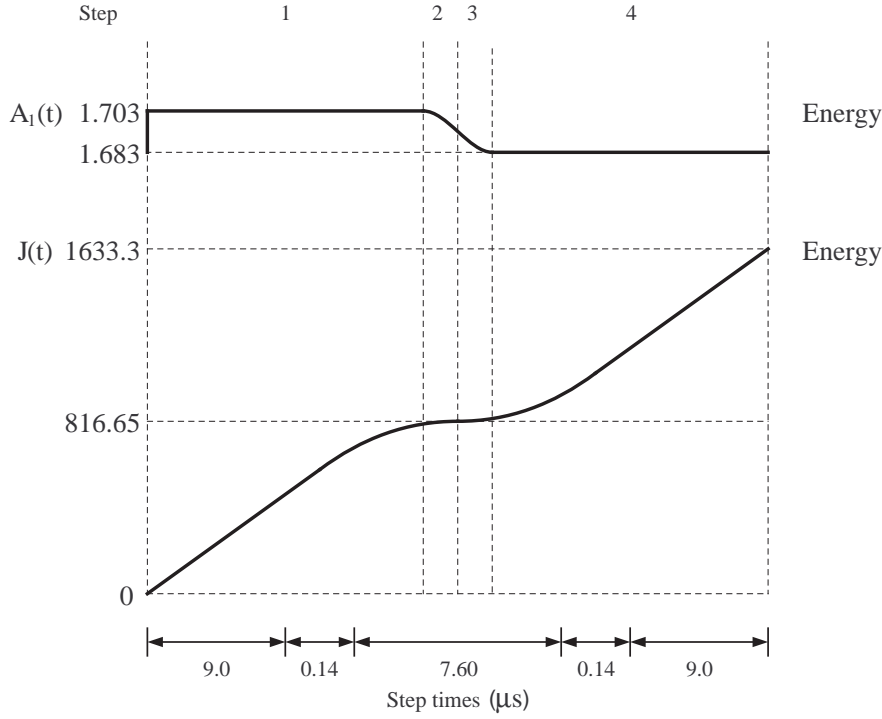


Fig. 3.2: Evolution of the hyperfine and exchange interaction strengths required to convert nuclear spin information into electron spin information, as shown in Eqs. (3.1–3.4).

dephasing, and, since it is far from any level crossings, perfectly preserved during the adiabatic evolution. Consequently, no figure has been included for  $|11\rangle$ .

At the other extreme, even in the absence of dephasing, the nuclear state  $|00\rangle$  is converted into electron state  $|a_e\rangle$  with high probability of error  $\epsilon \sim 10^{-3}$ . With dephasing, state  $|00\rangle$  also embodies the worst-case fidelity of the readout operation. For realistic dephasing times, this suggests a fidelity of state preparation (before tunnelling an actual readout) of  $10^{-2}$ .

While this low fidelity is not ideal, it could probably be tolerated. There are, however, more serious concerns. Firstly, even with donors spaced 20nm apart and 1V applied to the  $J$ -electrode, simulations suggest that the ex-

change coupling could be as weak as 0.03meV, or 420 in units of  $g_n\mu_n B_z$  [159]. This is insufficient to access the desired level crossing.

Furthermore, the  $D^-$  state of two electrons on one donor has a very weak binding energy of 1.7meV. Calculations suggest that a DC field designed to encourage electron 1 to tunnel onto donor 2 would also be sufficient to ionize the  $D^-$  state [133].

### 3.3 *Conclusion*

Current simulations suggests that there are serious concerns with regard to the accessibility, fidelity, and stability of the states used in the adiabatic Kane readout proposal. Modifications to the scheme such as using an rf field to Rabi flip electron 1 dependent on nuclear spin 1 instead of the adiabatic process and using resonant fields to induce Rabi oscillations of electron 1 onto donor 2 provided the transition is permitted by spin have been suggested as a way around these problems [133]. A completely new scheme involving three donors, one ionized, and avoiding the need for double occupancy has also been proposed [160]. Further theoretical and experimental work is required to develop these ideas.

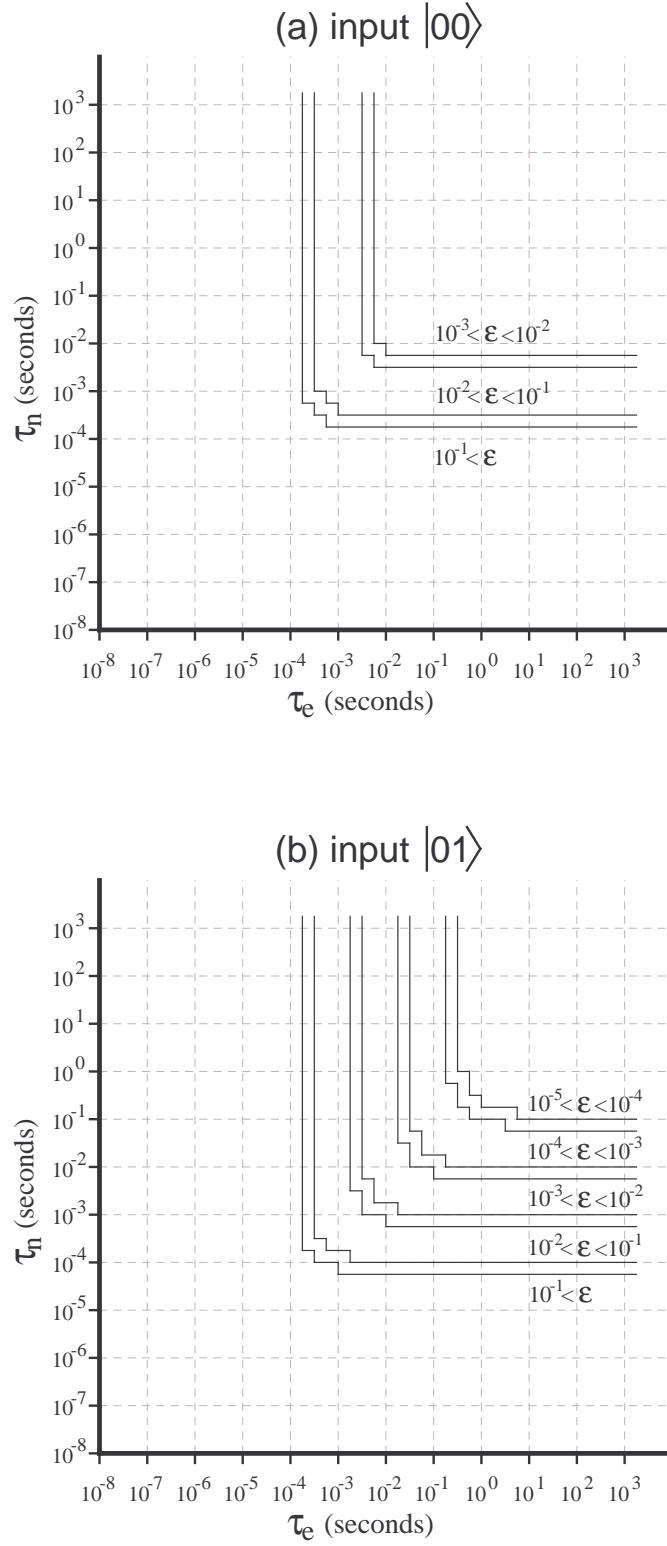


Fig. 3.3: Probability of error  $\epsilon$  during readout state preparation as a function of  $\tau_e$  and  $\tau_n$  for input state (a)  $|00\rangle$  and (b)  $|01\rangle$ .

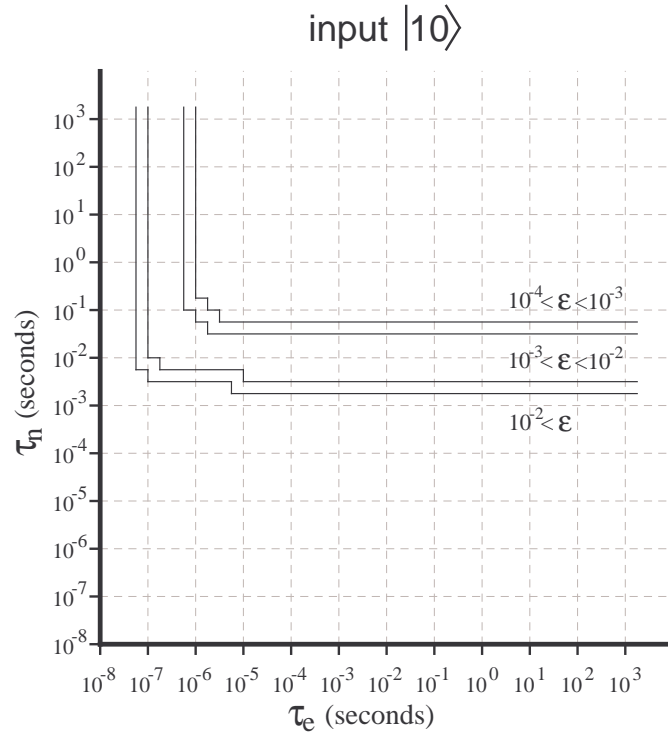


Fig. 3.4: Probability of error  $\epsilon$  during readout state preparation as a function of  $\tau_e$  and  $\tau_n$  for input state  $|10\rangle$ .

## 4. Implementing arbitrary 2-qubit gates

Efficiently implementing arbitrary 2-qubit gates using a given physical architecture is an important part of practical quantum computation. In this chapter, we combine techniques from Refs [161, 162, 163, 164] to present an efficient, but not necessarily time-optimal implementation of an arbitrary 2-qubit gate using at most three periods of free evolution of a certain class of 2-qubit system interspersed with at most eight single-qubit gates. The construction requires that the architecture be able to isolate qubits from one another. This chapter should be considered clarification and review rather than original research. A number of examples of gates built using the method detailed in this chapter can be found in Ref. [144].

In Section 4.1, prior work on implementing quantum gates is reviewed. Section 4.2 contains essential terminology and notation. Given an arbitrary 2-qubit gate  $G$ , Section 4.3 details how to construct a canonical decomposition comprised of four single-qubit gates and one purely non-local 2-qubit gate. Section 4.4 describes how to make the canonical decomposition unique. Section 4.5 uses the unique canonical decompositions of  $G$  and a given 2-qubit evolution operator  $U(t)$  to obtain a physical implementation of  $G$  using at most three periods of free evolution of  $U(t)$  and eight single-qubit gates. Section 4.6 concludes with a discussion of the implications of canonically decomposed gates, and describes further work.

### 4.1 Background

Implementing arbitrary gates given an arbitrary architecture is a nontrivial task. General methods have been developed for two special classes of physical architecture — those in which single-qubit gates can be approximated as instantaneous due to their speed relative to multiple qubit interactions, and those with the ability to isolate qubits from one another. When single-qubit gates are much faster than multiple-qubit interactions, time-optimal implementations can be found [165, 166, 164]. In the Kane architecture, single qubit gates cannot be approximated as instantaneous, but qubits can be isolated from one another [140], so we focus on the efficient, but not necessarily time-optimal method described in [163].

In both cases, the canonical decomposition [161, 162, 163, 164] forms the starting point of the construction. Given an arbitrary 2-qubit gate  $G$ , the canonical decomposition is a circuit, equivalent up to global phase, involving up to four single-qubit gates  $G_{1A}, G_{1B}, G_{2A}, G_{2B}$  and a purely non-local gate  $G_{\vec{\theta}} = e^{i(\theta_1 X \otimes X + \theta_2 Y \otimes Y + \theta_3 Z \otimes Z)}$  (Fig. 4.1a). Note that this decomposition is only unique if certain restrictions are placed on  $\vec{\theta}$ . A complete discussion of the many symmetries of the canonical decomposition is given in [163].

Not all 2-qubit time evolution operators  $U(t)$  admit such a simple decomposition. The most general time-dependent decomposition has a 2-qubit term

$$U_{(\phi_1(t), \phi_2(t), \phi_3(t))} = e^{i(\phi_1(t)X \otimes X + \phi_2(t)Y \otimes Y + \phi_3(t)Z \otimes Z)}. \quad (4.1)$$

This case is dealt with in [163], but is not required here. Instead, we focus on time evolution operators that can be decomposed as  $U_{\vec{\phi}t}$  (Fig. 4.1b). Comparing  $\vec{\theta}$  and  $\vec{\phi}$ ,  $G$  can be expressed as at most three applications of  $U_{\vec{\phi}t}$  interspersed with at most eight single-qubit gates (Fig. 4.1c).



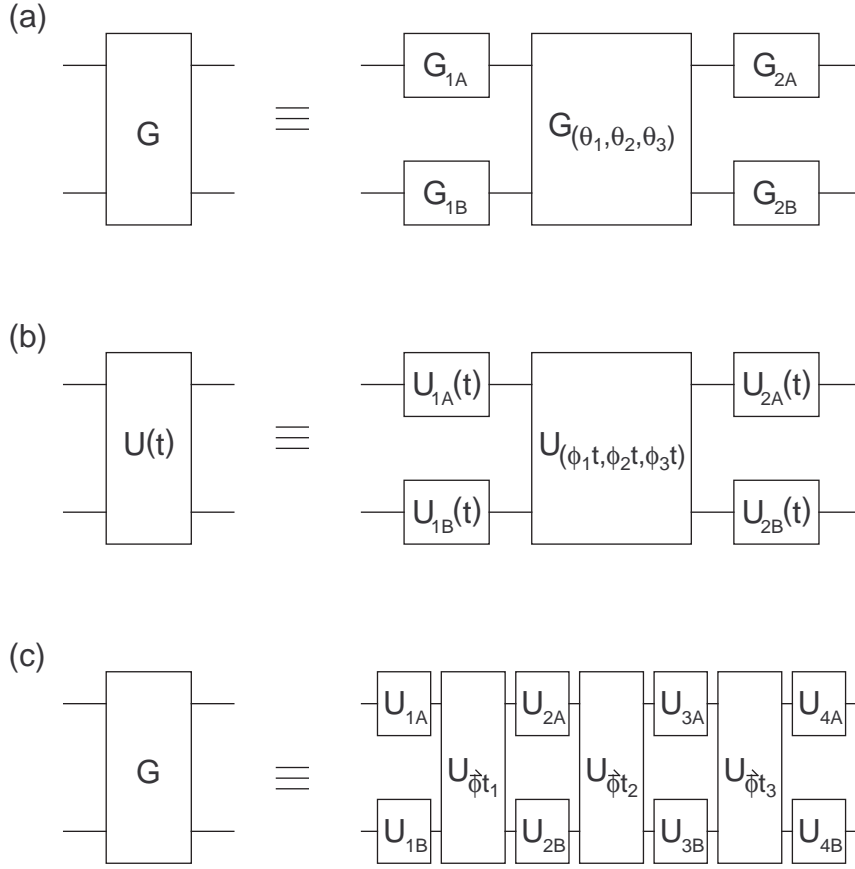


Fig. 4.1: (a) Circuit equivalent to an arbitrary gate constructed via the canonical decomposition. (b) Similar equivalent circuit which exists for a restricted class of 2-qubit evolution operators. (c) Arbitrary gate expressed as at most three periods evolution of the 2-qubit evolution operator and eight single-qubit gates.

## 4.2 Terminology and notation

This section contains the terminology and notation used in this chapter. Unless otherwise specified, all quantities in this chapter are expressed in the computational basis  $\{|00\rangle, |01\rangle, |10\rangle, |11\rangle\}$ . Heavy use will also be made of the magic basis [167]

$$\begin{aligned}
|\Phi_1\rangle &= \frac{1}{\sqrt{2}}(|00\rangle + |11\rangle) \\
|\Phi_2\rangle &= \frac{-i}{\sqrt{2}}(|00\rangle - |11\rangle) \\
|\Phi_3\rangle &= \frac{1}{\sqrt{2}}(|01\rangle - |10\rangle) \\
|\Phi_4\rangle &= \frac{-i}{\sqrt{2}}(|01\rangle + |10\rangle).
\end{aligned} \tag{4.2}$$

The transformation matrix from the magic basis to the computational basis is

$$Q = \frac{1}{\sqrt{2}} \begin{pmatrix} 1 & -i & 0 & 0 \\ 0 & 0 & 1 & -i \\ 0 & 0 & -1 & -i \\ 1 & i & 0 & 0 \end{pmatrix}. \tag{4.3}$$

States  $|\Psi\rangle$  and matrices  $G$  expressed in the magic basis will be denoted by  $|\tilde{\Psi}\rangle = Q^\dagger|\Psi\rangle$  and  $\tilde{G} = Q^\dagger G Q$  respectively.

Given an arbitrary 2-qubit gate  $G$ , a canonical decomposition is a set of four single-qubit gates  $G_{1A}, G_{1B}, G_{2A}, G_{2B}$  and a purely non-local gate  $G_{\vec{\theta}} = e^{i(\theta_1 X \otimes X + \theta_2 Y \otimes Y + \theta_3 Z \otimes Z)}$  such that

$$G \cong (G_{2A} \otimes G_{2B}) G_{\vec{\theta}} (G_{1A} \otimes G_{1B}), \tag{4.4}$$

where  $\cong$  denotes equality up to global phase. Two sets of non-local parameters  $\vec{\theta}, \vec{\phi}$  are called locally equivalent if there exist matrices  $U_1, U_2, U_3, U_4 \in$

$U(2)$  such that  $G_{\vec{\theta}} = (U_3 \otimes U_4)G_{\vec{\theta}}(U_1 \otimes U_2)$ . The canonical decomposition can be made unique by requiring  $\theta_1 \geq \theta_2$ ,  $\pi/2 - \theta_1 \geq \theta_2$ ,  $\theta_2 \geq \theta_3$ ,  $\theta_3 \geq 0$ , and  $\pi/2 - \theta_1 \geq \theta_1$  if  $\theta_3 = 0$ .

### 4.3 Constructing a canonical decomposition

In this section, we take a 2-qubit gate  $G$  and construct a canonical decomposition  $G \cong (G_{2A} \otimes G_{2B})G_{\vec{\theta}}(G_{1A} \otimes G_{1B})$ . Firstly, let  $G_S = e^{-i\delta}G$ ,  $\delta = -\arg(\det(G))/4$ , so that  $\det(G_S) = 1$ . Since  $\arg$  only determines values up to  $2n\pi$ ,  $\delta$  is only determined up to  $n\pi/2$ . Arbitrarily choose  $\delta \in (-\pi/4, \pi/4]$ . As we shall see,  $\det(G_S) = 1$  is required to enable the construction of  $G_{\vec{\theta}}$ .

Next, we determine the eigensystem of  $\tilde{G}_S^T \tilde{G}_S$  to obtain eigenvalues  $\{e^{2i\epsilon_k}\}$  and eigenvectors  $\{|\tilde{\Psi}_k\rangle\}$ . Note that while  $\tilde{G}_S^T \tilde{G}_S$  is symmetric and hence possesses a real, orthonormal eigenbasis, standard analytic and numerical methods of obtaining the eigenvectors in general only yield a linearly independent set. Hence, for the moment, we only assume that  $\{|\tilde{\Psi}_k\rangle\}$  is linearly independent.

In Ref. [161] it was shown that

$$(\tilde{G}_S^T \tilde{G}_S)^* |\tilde{\Psi}_k\rangle = (\tilde{G}_S^T \tilde{G}_S)^{-1} |\tilde{\Psi}_k\rangle = e^{-2i\epsilon_k} |\tilde{\Psi}_k\rangle, \quad (4.5)$$

implying  $\tilde{G}_S^T \tilde{G}_S |\tilde{\Psi}_k\rangle^* = e^{2i\epsilon_k} |\tilde{\Psi}_k\rangle^*$ . By considering states  $(|\tilde{\Psi}_k\rangle \pm |\tilde{\Psi}_k\rangle^*)/2$  it can be seen that both the real and imaginary parts of  $\{|\tilde{\Psi}_k\rangle\}$  are themselves eigenvectors with the same eigenvalue. It can be shown that a subset of  $\{\text{Re}(|\tilde{\Psi}_k\rangle), \text{Im}(|\tilde{\Psi}_k\rangle)\}$  always exists that is linearly independent and forms a real eigenbasis. Using the Gram-Schmidt procedure then gives us a real, orthonormal eigenbasis which we redefine  $\{|\tilde{\Psi}_k\rangle\}$  to equal. Let  $\tilde{O}_1$  be the

matrix with rows equal to  $|\tilde{\Psi}_k\rangle$ . Note that  $\tilde{O}_1$  is orthogonal and hence  $|\det(\tilde{O}_1)| = 1$ . If  $\det(\tilde{O}_1) = -1$ , redefine  $|\tilde{\Psi}_1\rangle$  to equal  $-|\tilde{\Psi}_1\rangle$  so that  $\det(\tilde{O}_1) = 1$ . Let

$$\tilde{G}_{2\tilde{\epsilon}} = \begin{pmatrix} e^{2i\epsilon_1} & 0 & 0 & 0 \\ 0 & e^{2i\epsilon_2} & 0 & 0 \\ 0 & 0 & e^{2i\epsilon_3} & 0 \\ 0 & 0 & 0 & e^{2i\epsilon_4} \end{pmatrix}. \quad (4.6)$$

Note that as defined  $\tilde{O}_1$  diagonalizes  $\tilde{G}_S^T \tilde{G}_S$  meaning  $\tilde{G}_S^T \tilde{G}_S = \tilde{O}_1^T G_{2\tilde{\epsilon}} \tilde{O}_1$ .

Compute  $\epsilon_k \in (-\pi/2, \pi/2]$  from the eigenvalues  $e^{2i\epsilon_k}$  of  $\tilde{G}_S^T \tilde{G}_S$ . Since  $\det(\tilde{G}_S^T \tilde{G}_S) = 1$ ,  $\sum_k \epsilon_k = n\pi$ . If  $n > 0$ , subtract  $\pi$  from the  $n$  largest values of  $\epsilon_k$  as we shall later use  $\sum \epsilon_k = 0$  to eliminate  $\epsilon_3$  and allow  $\theta_1, \theta_2, \theta_3$  to be expressed in closed form in terms of  $\epsilon_1, \epsilon_2, \epsilon_4$ . Note that the eigenvalues  $e^{2i\epsilon_k}$  are not changed by this convenient redefinition. Similarly, if  $n < 0$ , add  $\pi$  to the  $n$  most negative values of  $\epsilon_k$ . Let  $\tilde{O}_2 = \tilde{G}_S \tilde{O}_1^T \tilde{G}_\epsilon^*$ . It can be directly verified that  $\tilde{O}_2$  is special orthogonal. We now have  $\tilde{G}_S = \tilde{O}_2 \tilde{G}_\epsilon \tilde{O}_1$ , and are close to obtaining a canonical decomposition.

In [163] it was shown that  $SO(4) = Q^\dagger SU(2) \otimes SU(2) Q$ , where  $Q$  is the transformation matrix of Eq. (4.3). The generic form of an element of  $SU(2) \otimes SU(2)$  is

$$\begin{pmatrix} a\alpha & a\beta & b\alpha & b\beta \\ -a\beta^* & a\alpha^* & -b\beta^* & b\alpha^* \\ -b^*\alpha & -b^*\beta & a^*\alpha & a^*\beta \\ b^*\beta^* & -b^*\alpha^* & -a^*\beta^* & a^*\alpha^* \end{pmatrix} = \begin{pmatrix} a & b \\ -b^* & a^* \end{pmatrix} \otimes \begin{pmatrix} \alpha & \beta \\ -\beta^* & \alpha^* \end{pmatrix}, \quad (4.7)$$

where  $a, b, \alpha, \beta \in \mathbb{C}$ ,  $|a|^2 + |b|^2 = 1$ , and  $|\alpha|^2 + |\beta|^2 = 1$ . After calculating

$O_1 = Q\tilde{O}_1Q^\dagger \in SU(2) \otimes SU(2)$ , two matrices  $G_{1A}, G_{1B} \in SU(2)$  such that  $O_1 = G_{1A} \otimes G_{1B}$  can be readily constructed from Eq. (4.7). For example,  $a^2 = (a\alpha)(a\alpha^*) - (a\beta)(-a\beta^*)$ . Matrices  $G_{1A}, G_{1B}$  are unique up to a possible mutual sign flip. Matrices  $G_{2A}, G_{2B} \in SU(2)$  such that  $O_2 = G_{2A} \otimes G_{2B}$  can similarly be constructed.

All that remains to do is convert  $\tilde{G}_{\vec{\epsilon}}$  into  $\tilde{G}_{\vec{\theta}} = Q^\dagger G_{\vec{\theta}} Q$ , which is

$$\begin{pmatrix} e^{i(\theta_1 - \theta_2 + \theta_3)} & 0 & 0 & 0 \\ 0 & e^{i(-\theta_1 + \theta_2 + \theta_3)} & 0 & 0 \\ 0 & 0 & e^{-i(\theta_1 + \theta_2 + \theta_3)} & 0 \\ 0 & 0 & 0 & e^{i(\theta_1 + \theta_2 - \theta_3)} \end{pmatrix}. \quad (4.8)$$

We therefore need

$$\epsilon_1 = \theta_1 - \theta_2 + \theta_3, \quad (4.9)$$

$$\epsilon_2 = -\theta_1 + \theta_2 + \theta_3, \quad (4.10)$$

$$\epsilon_3 = -\theta_1 - \theta_2 - \theta_3, \quad (4.11)$$

$$\epsilon_4 = \theta_1 + \theta_2 - \theta_3. \quad (4.12)$$

Since we have ensured that  $\sum_k \epsilon_k = 0$ , Eqs (4.9–4.12) are consistent and can be inverted to give

$$\theta_1 = (\epsilon_1 + \epsilon_4)/2 \quad (4.13)$$

$$\theta_2 = (\epsilon_2 + \epsilon_4)/2 \quad (4.14)$$

$$\theta_3 = (\epsilon_1 + \epsilon_2)/2. \quad (4.15)$$

We now have a canonical decomposition  $G \cong G_S = (G_{2A} \otimes G_{2B})G_{\vec{\theta}}(G_{1A} \otimes G_{1B})$ .

#### 4.4 Making a canonical decomposition unique

In this section, we explain how to modify  $G_{1A}$ ,  $G_{2A}$ ,  $G_{2A}$ ,  $G_{2B}$  to make  $\vec{\theta}$  unique. As it stands,  $\vec{\theta} \in (-\pi, \pi]^3$ . By direct multiplication it can be seen that

$$G_{(\theta_1 \pm \pi/2, \theta_2, \theta_3)} = \pm i(X \otimes X)G_{(\theta_1, \theta_2, \theta_3)} \quad (4.16)$$

$$G_{(\theta_1, \theta_2 \pm \pi/2, \theta_3)} = \pm i(Y \otimes Y)G_{(\theta_1, \theta_2, \theta_3)} \quad (4.17)$$

$$G_{(\theta_1, \theta_2, \theta_3 \pm \pi/2)} = \pm i(Z \otimes Z)G_{(\theta_1, \theta_2, \theta_3)}. \quad (4.18)$$

By appropriately redefining  $G_{1A}$ ,  $G_{1B}$ ,  $G_{2A}$ ,  $G_{2B}$ ,  $\vec{\theta}$  can be restricted to the range  $[0, \pi/2)$ .

As explained in beautiful detail in [163], there are 24 locally equivalent sets of values of  $\vec{\theta} \in [0, \pi/2)^3$ . Given  $(\theta_1, \theta_2, \theta_3)$ , the locally equivalent values are  $(\theta_i, \theta_j, \theta_k)$ ,  $(\pi/2 - \theta_i, \pi/2 - \theta_j, \theta_k)$ ,  $(\pi/2 - \theta_i, \theta_j, \pi/2 - \theta_k)$ , and  $(\theta_i, \pi/2 - \theta_j, \pi/2 - \theta_k)$  where  $i, j, k$ , are permutations of 1, 2, 3. To be more constructive, let

$$P_{12} = e^{i\pi/4Z} \otimes e^{i\pi/4Z} \quad (4.19)$$

$$P_{13} = e^{i\pi/4Y} \otimes e^{i\pi/4Y} \quad (4.20)$$

$$P_{23} = e^{i\pi/4X} \otimes e^{i\pi/4X} \quad (4.21)$$

$$M_{12} = e^{i\pi/4Z} \otimes e^{-i\pi/4Z} \quad (4.22)$$

$$M_{13} = e^{i\pi/4Y} \otimes e^{-i\pi/4Y} \quad (4.23)$$

$$M_{23} = e^{i\pi/4X} \otimes e^{-i\pi/4X}. \quad (4.24)$$

Given  $G_{(\theta_1, \theta_2, \theta_3)}$ , we find that

$$G_{(\theta_2, \theta_1, \theta_3)} = P_{12}G_{(\theta_1, \theta_2, \theta_3)}P_{12}^\dagger \quad (4.25)$$

$$G_{(\theta_3, \theta_2, \theta_1)} = P_{13} G_{(\theta_1, \theta_2, \theta_3)} P_{13}^\dagger \quad (4.26)$$

$$G_{(\theta_1, \theta_3, \theta_2)} = P_{23} G_{(\theta_1, \theta_2, \theta_3)} P_{23}^\dagger \quad (4.27)$$

$$G_{(-\theta_2, -\theta_1, \theta_3)} = M_{12} G_{(\theta_1, \theta_2, \theta_3)} M_{12}^\dagger \quad (4.28)$$

$$G_{(-\theta_3, \theta_2, -\theta_1)} = M_{13} G_{(\theta_1, \theta_2, \theta_3)} M_{13}^\dagger \quad (4.29)$$

$$G_{(\theta_1, -\theta_3, -\theta_2)} = M_{23} G_{(\theta_1, \theta_2, \theta_3)} M_{23}^\dagger \quad (4.30)$$

Using Eqs (4.25–4.30) and (4.16–4.18), it is always possible to obtain  $\vec{\theta}$  such that  $\theta_1 \geq \theta_2$ ,  $\pi/2 - \theta_1 \geq \theta_2$ ,  $\theta_2 \geq \theta_3$ ,  $\theta_3 \geq 0$ , and  $\pi/2 - \theta_1 \geq \theta_1$  if  $\theta_3 = 0$ . To obtain this unique  $\vec{\theta}$ , use Eqs (4.25–4.27) to order  $\theta_k$  such that  $\theta_1 \geq \theta_2 \geq \theta_3 \geq 0$ . If  $\theta_1 > \pi/4$  and  $\theta_2 \geq \pi/2 - \theta_1$ , use Eq. (4.28) and Eqs (4.16–4.17) to obtain  $(\pi/2 - \theta_2, \pi/2 - \theta_1, \theta_3)$ . Finally, again use Eqs (4.25–4.27) to order  $\theta_k$ . This gives the unique  $\vec{\theta}$  with the desired properties.

For the remainder of the thesis, when talking about a canonical decomposition of a gate  $G$ , we mean  $G_{1A}, G_{1B}, G_{2A}, G_{2B} \in U(2)$  and the unique  $\vec{\theta}$  described above such that  $G \cong (G_{2A} \otimes G_{2B}) G_{\vec{\theta}} (G_{1A} \otimes G_{1B})$  up to global phase. We have not restricted the single-qubit unitaries to be special as none of the standard single-qubit gates  $H$ ,  $X$ ,  $Z$ ,  $S$  and  $T$  are special and we wish to express  $G_{1A}$ ,  $G_{1B}$ ,  $G_{2A}$  and  $G_{2B}$  in terms of standard gates whenever possible.

#### 4.5 Building gates out of physical interactions

To complete the construction of an arbitrary gate  $G$  in terms of a 2-qubit evolution operator  $U(t)$  admitting a canonical decomposition with 2-qubit term  $U_{\vec{\phi}t}$  and single-qubit gates, let

$$G \cong (G_{2A} \otimes G_{2B}) G_{\vec{\theta}} (G_{1A} \otimes G_{1B}), \quad (4.31)$$

$$U(t) \cong (U_{2A}(t) \otimes U_{2B}(t)) U_{\vec{\phi}t} (U_{1A}(t) \otimes U_{1B}(t)), \quad (4.32)$$

and following [163], consider

$$\begin{aligned}
& M_{23}P_{23}P_{13}e^{i(\phi_1 X \otimes X + i\phi_2 Y \otimes Y + i\phi_3 Z \otimes Z)t_3}P_{13}^\dagger P_{23}^\dagger M_{23}^\dagger \\
& \times M_{12}P_{23}e^{i(\phi_1 X \otimes X + i\phi_2 Y \otimes Y + i\phi_3 Z \otimes Z)t_2}P_{23}^\dagger M_{12}^\dagger \\
& \times e^{i(\phi_1 X \otimes X + i\phi_2 Y \otimes Y + i\phi_3 Z \otimes Z)t_1} \\
& = e^{i(\phi_1 t_1 - \phi_3 t_2 + \phi_3 t_3)X \otimes X + i(\phi_2 t_1 - \phi_1 t_2 - \phi_2 t_3)Y \otimes Y + i(\phi_3 t_1 + \phi_2 t_2 - \phi_1 t_3)Z \otimes Z}.
\end{aligned} \tag{4.33}$$

With the conditions on  $\vec{\phi}$ , the equations

$$\begin{pmatrix} \phi_1 & -\phi_3 & \phi_3 \\ \phi_2 & -\phi_1 & -\phi_2 \\ \phi_3 & \phi_2 & -\phi_1 \end{pmatrix} \begin{pmatrix} t_1 \\ t_2 \\ t_3 \end{pmatrix} = \begin{pmatrix} \theta_1 \\ \theta_2 \\ \theta_3 \end{pmatrix} \tag{4.34}$$

are invertible. Note that this system of equations is neither unique nor special, as other matrices from Eqs (4.25–4.30) could have been used in Eq. (4.33). For example

$$\begin{aligned}
& M_{12}P_{12}e^{i(\phi_1 X \otimes X + i\phi_2 Y \otimes Y + i\phi_3 Z \otimes Z)t_3}P_{12}^\dagger M_{12}^\dagger \\
& \times M_{23}M_{13}e^{i(\phi_1 X \otimes X + i\phi_2 Y \otimes Y + i\phi_3 Z \otimes Z)t_2}M_{13}^\dagger M_{23}^\dagger \\
& \times e^{i(\phi_1 X \otimes X + i\phi_2 Y \otimes Y + i\phi_3 Z \otimes Z)t_1} \\
& = e^{i(\phi_1 t_1 - \phi_3 t_2 - \phi_1 t_3)X \otimes X + i(\phi_2 t_1 + \phi_1 t_2 - \phi_2 t_3)Y \otimes Y + i(\phi_3 t_1 - \phi_2 t_2 + \phi_3 t_3)Z \otimes Z}
\end{aligned} \tag{4.35}$$

also leads to an invertible system of equations.

After solving Eq. (4.34) for  $t_1, t_2, t_3$ , let

$$U_1 = U_{1A}^\dagger(t_1)G_{1A} \tag{4.36}$$

$$U_2 = U_{1B}^\dagger(t_1)G_{1B} \tag{4.37}$$

$$U_3 = U_{1A}^\dagger(t_2)e^{i\pi/4X}e^{i\pi/4Z}U_{2A}^\dagger(t_1) \tag{4.38}$$



$$U_4 = U_{1B}^\dagger(t_2)e^{i\pi/4X}e^{-i\pi/4Z}U_{2B}^\dagger(t_1) \quad (4.39)$$

$$U_5 = U_{1A}^\dagger(t_3)e^{i\pi/4Y}e^{i\pi/4X}e^{i\pi/4X}e^{-i\pi/4Z}e^{-i\pi/4X}U_{2A}^\dagger(t_2) \quad (4.40)$$

$$U_6 = U_{1B}^\dagger(t_3)e^{i\pi/4Y}e^{i\pi/4X}e^{-i\pi/4X}e^{i\pi/4Z}e^{-i\pi/4X}U_{2B}^\dagger(t_2) \quad (4.41)$$

$$U_7 = G_{2A}e^{-i\pi/4X}e^{-i\pi/4X}e^{-i\pi/4Y}U_{2A}^\dagger(t_3) \quad (4.42)$$

$$U_8 = G_{2B}e^{i\pi/4X}e^{-i\pi/4X}e^{-i\pi/4Y}U_{2B}^\dagger(t_3). \quad (4.43)$$

With these definitions, it can be verified by direct multiplication that

$$G \cong (U_7 \otimes U_8)U(t_3)(U_5 \otimes U_6)U(t_2)(U_3 \otimes U_4)U(t_1)(U_1 \otimes U_2). \quad (4.44)$$

Note that arbitrary choices have entered the calculation at a number of points meaning the above construction is not unique and may not be optimal. It can, however, be shown that no general construction of this form can use fewer than three periods of evolution of  $U(t)$  and eight single qubit gates in the worst case [163]. This suggests that the above implementation is close to optimal, and at worst efficient.

## 4.6 Conclusion

The construction of this chapter enables arbitrary 2-qubit gates to be expressed as a simple circuit involving at most eight single-qubit gates and three periods of evolution of a restricted class of 2-qubit interactions. This implies that if multiple single and 2-qubit gates are applied to the same pair of qubits, they should all be combined into a single compound gate to save time and reduce circuit complexity. Chapters 5, 6 and 8 rely heavily on this technique to absorb swap gates into neighboring useful gates, dramatically simplifying the circuits described therein.



## 5. 5-qubit QEC on an LNN QC

The question has been raised as to how well quantum error correction (QEC) can be implemented on a linear nearest neighbor (LNN) quantum computer [168] due to the expectation that numerous swap gates will be required. Working out a way around this is important due to the large number of LNN architectures currently under investigation [93, 92, 94, 101, 99, 169, 170, 171, 172, 173, 174, 175, 102, 176, 177]. In this chapter, a quantum circuit implementing 5-qubit QEC on an LNN architecture is described. Our goal is to keep the error correction scheme as simple as possible to facilitate physical realization. In particular, fault-tolerance has not been built into the circuit to minimize its complexity and the required number of qubits. Despite the lack of fault-tolerance, we show that, for both a discrete and continuous error model, a threshold physical error rate exists below which the circuit reduces the probability of error in the protected logical qubit. We also determine the required physical error rate for the logical qubit to be 10 times and 100 times as reliable as a single unprotected qubit.

This chapter is organized as follows. Firstly, explicit examples of canonically decomposed compound gates incorporating the swap gates required on an LNN architecture are given in Section 5.1. In Section 5.2, the non-fault-tolerant 5-qubit QEC scheme is described and the LNN circuit presented. Simulations of the performance of the LNN scheme when subjected to both discrete and continuous errors are discussed in Section 5.3. Section 5.4 con-

cludes with a summary of all results and a description of further work.

### 5.1 Compound gates

As discussed in detail in Chapter 4, the canonical decomposition enables any 2-qubit gate  $G$  to be expressed (non-uniquely) in the form

$$(G_{2A} \otimes G_{2B})G_{\vec{\theta}}(G_{1A} \otimes G_{1B}) \quad (5.1)$$

where  $G_{1A}, G_{1B}, G_{2A}, G_{2B} \in U(2)$  and

$$G_{\vec{\theta}} = e^{i(\theta_1 X \otimes X + \theta_2 Y \otimes Y + \theta_3 Z \otimes Z)}. \quad (5.2)$$

Provided a quantum computer allows qubits to be isolated, and has a 2-qubit evolution operator  $U(t)$  admitting a canonical decomposition with 2-qubit term  $U_{\vec{\phi}t}$ , an implementation of  $G$  exists using at most three periods of free evolution of  $U(t)$  and eight single-qubit gates.

Fig. 5.1a shows the form of a canonically decomposed CNOT on a Kane quantum computer [93, 144].  $Z$ -rotations have been represented by quarter, half and three-quarter circles corresponding to  $R_z(\pi/2)$ ,  $R_z(\pi)$ , and  $R_z(3\pi/2)$  respectively, where

$$R_z = e^{i\theta Z/2}. \quad (5.3)$$

Full circles represent  $Z$ -rotations of angle dependent on the physical construction of the computer (static magnetic field, phosphorus donor placement etc). The details of obtaining the canonical decomposition of the Kane 2-qubit evolution operator contained in [144]. Up to a couple of  $Z$ -rotations, the 2-qubit interaction corresponds to  $\phi_1 = \phi_2 = \pi/n$ , and  $\phi_3 = 0$ . Square

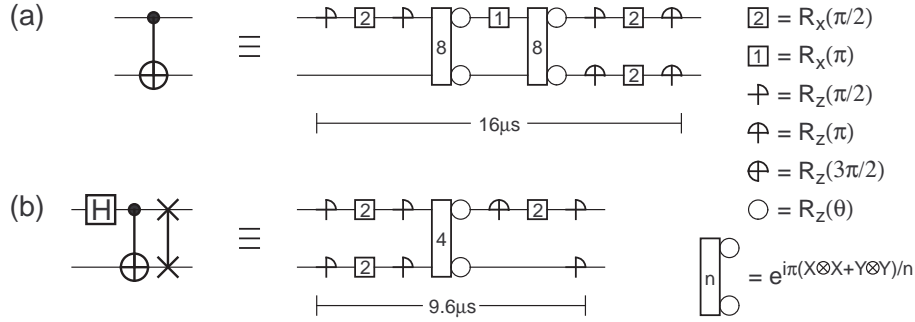


Fig. 5.1: Decomposition into physical operations of (a) CNOT and (b) Hadamard, CNOT then swap. Note that the Kane architecture has been used for illustrative purposes.

gates 1 and 2 correspond to X-rotations  $R_x(\pi)$  and  $R_x(\pi/2)$ . Fig. 5.1b shows an implementation of the composite gate Hadamard followed by CNOT followed by swap. Note that the total time of the compound gate is significantly less than the CNOT on its own. This fact has been used to minimize the total execution time of the LNN circuit of Fig. 5.2b.

The above implies that the swaps inevitably required in an LNN architecture to bring qubits together to be interacted can, in some cases, be incorporated into other gates without additional cost. On any architecture, canonically decomposed compound gates should be used whenever multiple single and 2-qubit gates are applied to the same two qubits.

## 5.2 5-qubit LNN QEC

5-qubit QEC schemes are designed to correct a single arbitrary error. No QEC scheme designed to correct a single arbitrary error can use less than five qubits [30]. A number of 5-qubit QEC proposals exist [178, 179, 112, 180, 181]. Fig. 5.2b shows a non-fault-tolerant circuit appropriate for an LNN architecture implementing the encode stage of the QEC scheme proposed in [178]. For reference, the original circuit is shown in Fig. 5.2a. Note that the

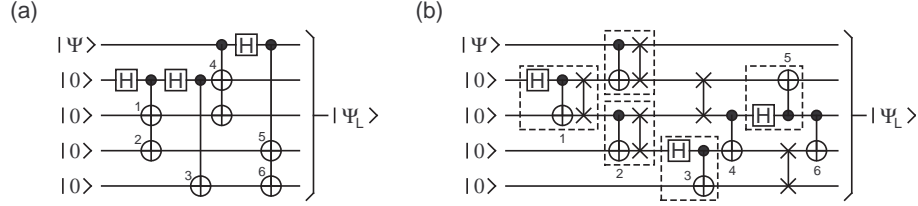


Fig. 5.2: (a) 5-qubit encoding circuit for general architecture, (b) equivalent circuit for linear nearest neighbor architecture with dashed boxes indicating compound gates. CNOT gates that must be performed sequentially are numbered.

LNN circuit uses exactly the same number of CNOTs and achieves minimal depth since the CNOT gates numbered 1–6 in Fig. 5.2a must be performed sequentially on any architecture that can only interact pairs of qubits (not three or more at once). The two extra “naked” swaps in Fig. 5.2b do not significantly add to the total time of the circuit. Fig. 5.3 shows an equivalent circuit broken into physical operations for a Kane quantum computer. Note that this circuit uses the fact that if two 2-qubit gates share a qubit then two single-qubit unitaries can be combined as shown in Fig. 5.4. The decode circuit is simply the encode circuit run backwards. 5-qubit QEC schemes are primarily useful for data storage due to the impossibility of fault-tolerantly interacting two logical qubits [118], though with some effort it is possible to nontrivially interact three logical qubits. Fig. 5.5 shows a full encode-wait-decode-measure-correct data storage cycle. Table 5.1 shows the range of possible measurements and the action required in each case.

### 5.3 Simulation of performance

When simulating the QEC cycle, the LNN circuit of Fig. 5.2b was used to keep the analysis independent of the specific architecture used. Each compound gate was modelled as taking the same time, allowing the time  $T$  to

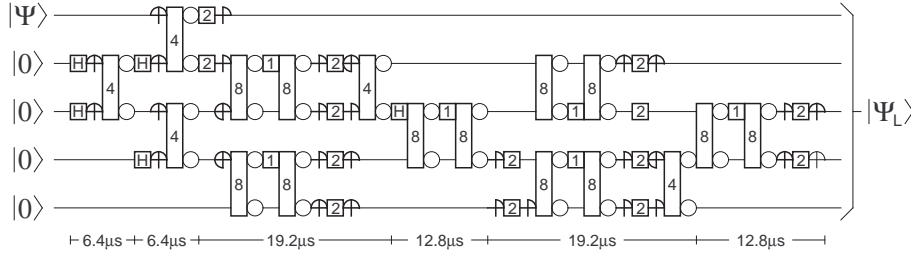


Fig. 5.3: A sequence of physical gates implementing the circuit of Fig. 5.2b. Note the Kane architecture has been used for illustrative purposes.

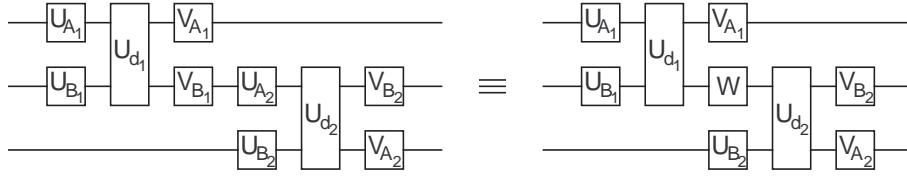


Fig. 5.4: Circuit equivalence used to reduce the number of physical gates in Fig. 5.3.  
 $W = U_{A_2} V_{B_1}$

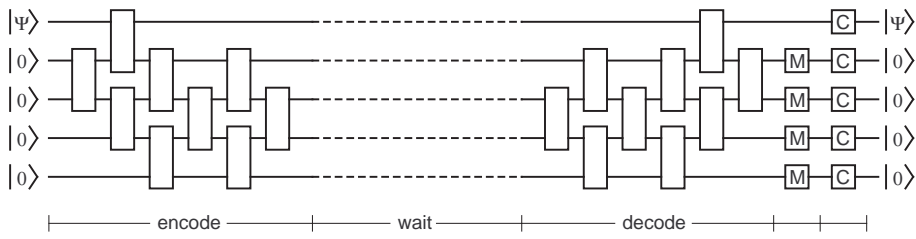


Fig. 5.5: A complete encode-wait-decode-measure-correct QEC cycle.

Measurement	Action
$\Psi' \otimes 0000$	$I \otimes IIII$
$\Psi' \otimes 0001$	$I \otimes IIIX$
$\Psi' \otimes 0010$	$I \otimes IIXI$
$\Psi' \otimes 0011$	$Z \otimes IIXX$
$\Psi' \otimes 0100$	$I \otimes IXII$
$\Psi' \otimes 0101$	$X \otimes IXIX$
$\Psi' \otimes 0110$	$Z \otimes IXXI$
$\Psi' \otimes 0111$	$X \otimes IXXX$
$\Psi' \otimes 1000$	$Z \otimes XIII$
$\Psi' \otimes 1001$	$I \otimes XIIIX$
$\Psi' \otimes 1010$	$X \otimes XIXI$
$\Psi' \otimes 1011$	$X \otimes XIXX$
$\Psi' \otimes 1100$	$Z \otimes XXII$
$\Psi' \otimes 1101$	$X \otimes XXIX$
$\Psi' \otimes 1110$	$XZ \otimes XXXI$
$\Psi' \otimes 1111$	$Z \otimes XXXX$

Tab. 5.1: Action required to correct the data qubit  $\Psi'$  vs measured value of ancilla qubits. Note that the X-operations simply reset the ancilla.

be made an integer such that each gate takes one time step. Gates were furthermore simulated as though perfectly reliable and errors applied to each qubit (including idle qubits) at the end of each time step. The rationale for including idle qubits is that, in an LNN architecture, active physical manipulation of some description is frequently required to decouple neighboring qubits. Both the manipulation itself and the degree of decoupling are likely to be imperfect, leading to errors. Furthermore, in schemes utilizing global electromagnetic fields to manipulate active qubits, supposedly idle qubits may not be sufficiently off resonant.

Two error models were used — discrete and continuous. In the discrete model, a qubit can suffer either a bit-flip (X), phase-flip (Z) or both simultaneously (XZ). Each type of error is equally likely with total probability of error  $p$  per qubit per time step. The continuous error model involves



applying single-qubit unitary operations of the form

$$U_\sigma = \begin{pmatrix} \cos(\theta/2)e^{i(\alpha+\beta)/2} & \sin(\theta/2)e^{i(\alpha-\beta)/2} \\ -\sin(\theta/2)e^{i(-\alpha+\beta)/2} & \cos(\theta/2)e^{i(-\alpha-\beta)/2} \end{pmatrix} \quad (5.4)$$

where  $\alpha$ ,  $\beta$ , and  $\theta$  are normally distributed about 0 with standard deviation  $\sigma$ .

Both the single-qubit and single logical qubit (five qubit) systems were simulated. The initial state

$$|\Psi\rangle = \sin(\pi/8)|0\rangle + \cos(\pi/8)|1\rangle \quad (5.5)$$

was used in both cases since  $|\langle\Psi|X|\Psi\rangle|^2 = 0.5$ ,  $|\langle\Psi|Z|\Psi\rangle|^2 = 0.5$ , and  $|\langle\Psi|XZ|\Psi\rangle|^2 = 0$  thus allowing each type of error to be detected (but not necessarily distinguished). Simpler states such as  $|0\rangle$ ,  $|1\rangle$ ,  $(|0\rangle+|1\rangle)/\sqrt{2}$ , and  $(|0\rangle-|1\rangle)/\sqrt{2}$  do not have this property. For example, the states  $|0\rangle$  and  $|1\rangle$  are insensitive to phase errors, whereas the other two states are insensitive to bit flip errors.

Let  $T_{wait}$  denote the duration of the wait stage. Note that the total duration of the encode, decode, measure and correct stages is 14. In the QEC case the total time  $T = T_{wait} + 14$  of one QEC cycle was varied to determine the time that minimizes the error per time step

$$\epsilon_{step} = 1 - \sqrt[T]{1 - \epsilon_{final}} \quad (5.6)$$

where  $\epsilon_{final} = 1 - |\langle\Psi'|\Psi\rangle|^2$  and  $|\Psi'\rangle$  is the final data qubit state. An optimal time  $T_{opt}$  exists since the logical qubit is only protected during the wait stage and the correction process can only cope with one error. If the wait time is zero, extra complexity has been added but no corrective ability. Similarly, if

$p$	$T_{opt}$	$\epsilon_{step}$	$\epsilon_{step}/p$
$10^{-2}$	25	$1.7 \times 10^{-2}$	$1.7 \times 10^0$
$1.6 \times 10^{-3}$	40	$1.6 \times 10^{-3}$	$1.0 \times 10^0$
$10^{-3}$	50	$8.4 \times 10^{-4}$	$8.4 \times 10^{-1}$
$10^{-4}$	150	$3.1 \times 10^{-5}$	$3.1 \times 10^{-1}$
$10^{-5}$	500	$1.0 \times 10^{-6}$	$1.0 \times 10^{-1}$
$10^{-6}$	1500	$3.2 \times 10^{-8}$	$3.2 \times 10^{-2}$
$10^{-7}$	5000	$1.0 \times 10^{-9}$	$1.0 \times 10^{-2}$
$10^{-8}$	10000	$2.0 \times 10^{-11}$	$2.0 \times 10^{-3}$

Tab. 5.2: Probability per time step  $\epsilon_{step}$  of the logical qubit being destroyed when using 5-qubit QEC vs physical probability  $p$  per qubit per time step of a discrete error.

the wait time is very large, it is almost certain that more than one error will occur, resulting in the qubit being destroyed during the correction process. Somewhere between these two extremes is a wait time that minimizes  $\epsilon_{step}$ . This property of non-fault-tolerant QEC has been noted previously [182].

Table 5.2 shows  $T_{opt}$ ,  $\epsilon_{step}$  and the reduction in error  $\epsilon_{step}/p$  versus  $p$  for discrete errors. Table 5.3 shows the corresponding data for continuous errors. Note that, in the continuous case, the single qubit  $p$  has been obtained via 1-qubit simulations using the indicated  $\sigma$  and wait time  $T = T_{opt} + 14$  and a 1-qubit version of Eq. (5.6)

$$p = 1 - \sqrt[T]{1 - \epsilon_{final}} \quad (5.7)$$

where  $\epsilon_{final} = 1 - |\langle \Psi' | \Psi \rangle|^2$  and  $|\Psi'\rangle$  is the final single-qubit state. In this context,  $p$  is the discrete error rate yielding the same final error probability as the corresponding  $\sigma$  over time  $T$ .

The threshold  $p = 1.6 \times 10^{-3}$  shown in Table 5.2 is comparable to some of the highest thresholds of fault-tolerant quantum computation described in Chapter 1, which were obtained using weaker noise models and architectures

$\sigma$	$T_{opt}$	$p$	$\epsilon_{step}$	$\epsilon_{step}/p$
$10^{-1}$	$2.5 \times 10^1$	$4.4 \times 10^{-3}$	$6.9 \times 10^{-3}$	$1.6 \times 10^0$
$4.7 \times 10^{-2}$	$5.5 \times 10^1$	$1.1 \times 10^{-3}$	$1.1 \times 10^{-3}$	$1.0 \times 10^0$
$10^{-2}$	$2.5 \times 10^2$	$4.9 \times 10^{-5}$	$1.4 \times 10^{-5}$	$2.9 \times 10^{-1}$
$3.6 \times 10^{-3}$	$5.5 \times 10^2$	$6.4 \times 10^{-6}$	$6.4 \times 10^{-7}$	$1.0 \times 10^{-1}$
$10^{-3}$	$2.5 \times 10^3$	$5.0 \times 10^{-7}$	$1.3 \times 10^{-8}$	$2.6 \times 10^{-2}$
$4.0 \times 10^{-4}$	$5.0 \times 10^3$	$8.0 \times 10^{-8}$	$8.0 \times 10^{-10}$	$1.0 \times 10^{-2}$
$10^{-4}$	$2.5 \times 10^4$	$5.0 \times 10^{-9}$	$1.0 \times 10^{-11}$	$2.0 \times 10^{-3}$
$10^{-5}$	$2.5 \times 10^5$	$5.0 \times 10^{-11}$	$7.2 \times 10^{-15}$	$1.4 \times 10^{-4}$

Tab. 5.3: Probability per time step  $\epsilon_{step}$  of the logical qubit being destroyed when using 5-qubit QEC vs standard deviation  $\sigma$  of continuous errors.

able to interact arbitrary pairs of qubits. If an error rate improvement of a factor of 10 or 100 is desired when using our scheme, then  $p = 10^{-5}$  or  $p = 10^{-7}$  is required respectively. Note that unlike fault-tolerant schemes, the error rate of the logical qubit does not scale as  $cp^2$ .

For continuous errors, the threshold standard deviation is  $\sigma = 4.7 \times 10^{-2}$ . The logical qubit is a factor of 10 more reliable than a single physical qubit for  $\sigma = 3.6 \times 10^{-3}$ . A factor of 100 improvement is achieved when  $\sigma = 4.0 \times 10^{-4}$ .

## 5.4 Conclusion

To summarize, we have presented a non-fault-tolerant circuit implementing 5-qubit QEC on an LNN architecture that achieves the same depth as the current least depth circuit [178], and simulated its effectiveness against both discrete and continuous errors. For the discrete error model, if error correction is to provide an error rate reduction of a factor of 10 or 100, the physical error rate  $p$  must be  $10^{-5}$  or  $10^{-7}$  respectively. The corresponding figures for the continuous error model are  $\sigma = 3.6 \times 10^{-3}$  and  $4.0 \times 10^{-4}$ .

Further work is required to determine whether the discrete or continuous

error model or some other model best describes errors in physical quantum computers. The relationship between the two error models also warrants further investigation. Further simulation is required to determine the error thresholds and scaling associated with single and 2-qubit LNN QEC protected gates.

## 6. QEC without measurement

In Chapter 5, we described and analyzed an explicit 5-qubit non-fault-tolerant LNN QEC scheme. In this chapter, we wish to relax the engineering requirements of this scheme further. In particular, for many architectures the most difficult aspect of quantum error correction is measuring qubits quickly and/or reliably. Interactive classical processing of measurement results can also be problematic. We therefore present an explicit 5-qubit QEC scheme that only requires slow resetting and no classical processing at the cost of halving the performance of the original approach and potentially requiring an additional 4 ancilla qubits. Prior work exists on removing measurement from fault-tolerant QEC [124, 183], but this approach requires many more qubits than the scheme presented here. A similar no measurement non-fault-tolerant LNN QEC scheme has been devised and physically implemented using liquid NMR technology [179], but is not directly applicable to other technologies, and only permits a single cycle of QEC to be performed.

The discussion is organized as follows. In Section 6.1, the concept of resetting as distinct from measurement is explained in more detail. In Section 6.2, a QEC scheme requiring fast resetting and no classical processing is described and its performance simulated. In Section 6.3, additional qubits are added to the circuit to enable the use of a slow reset operation. Section 6.4 concludes with a summary of our results and a description of further

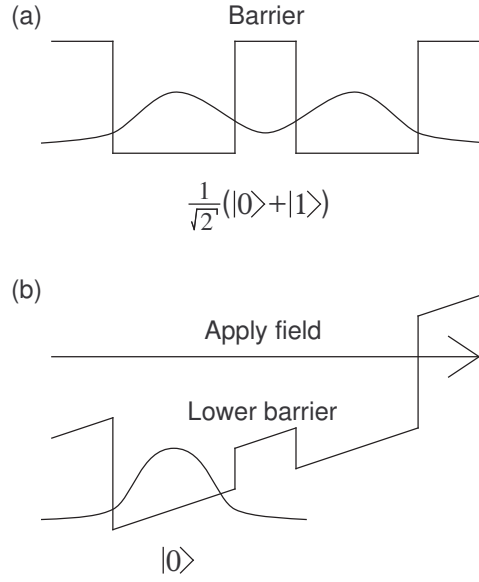


Fig. 6.1: Example of a physical model of resetting through relaxation. Given a double potential well with left and right occupancy representing  $|0\rangle$  and  $|1\rangle$  respectively, resetting to  $|0\rangle$  can be achieved by lowering the barrier and applying a bias.

work.

### 6.1 Resetting

Resetting is distinct from measurement in that a given qubit is in a known state after resetting but no information about its state beforehand is provided. A physical example of resetting is provided by a double quantum dot system separated by a potential barrier in which  $|0\rangle$  is represented by an electron in the left dot, and  $|1\rangle$  by an electron in the right dot. By applying an electric field across the double dot system and lowering the barrier potential, the electron can be encouraged to relax into the  $|0\rangle$  state. This process is illustrated in Fig. 6.1.

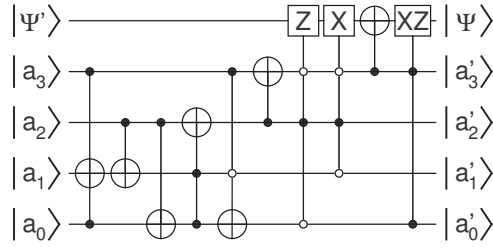


Fig. 6.2: Quantum circuit acting on a recently decoded logical qubit to correct the data qubit based on the value of the ancilla qubits. Hollow dots represent control qubits that must be  $|0\rangle$  for the attached gate to be applied.

## 6.2 5-qubit QEC without measurement

To eliminate measurement from Fig. 5.5, the implicit classical logic that converts the measured result into a corrective action must be converted into quantum logic gates. Fig. 6.2 shows a quantum circuit performing the necessary logic. The first half of the circuit rearranges the states 0000 to 1111 such that the required corrective action is as shown in column 3 of Table 6.1. This rearrangement of actions leads to the relatively simple corrective logic of the second half of Fig. 6.2.

In keeping with Chapter 5, an LNN version of Fig. 6.2 has been devised and is shown in Fig. 6.3. The LNN circuit was used in all simulations.

Given the increased complexity of Fig. 6.3 compared with Fig. 5.5, it is expected that the threshold error rates for both the discrete and continuous error models will be lower. Furthermore, the optimal wait time between correction cycles it is expected to be longer to balance the need for correction against the longer period of vulnerability during correction. Both of these effects can be observed in Tables 6.2 and 6.3.

For discrete errors, the new threshold error rate, and the error rates at which a factor of 10 and 100 improvement in reliability are achieved are

Ancilla	Action	Action
0000	I	I
0001	I	I
0010	I	I
0011	Z	I
0100	I	XZ
0101	X	X
0110	Z	Z
0111	X	I
1000	Z	X
1001	I	Z
1010	X	X
1011	X	Z
1100	Z	X
1101	X	Z
1110	XZ	X
1111	Z	Z

Tab. 6.1: Second column shows the action required to correct the data qubit given a certain ancilla value immediately after decoding. Third column shows the action required to correct the data qubit given a certain ancilla value after the application of the first half of Fig. 6.2.

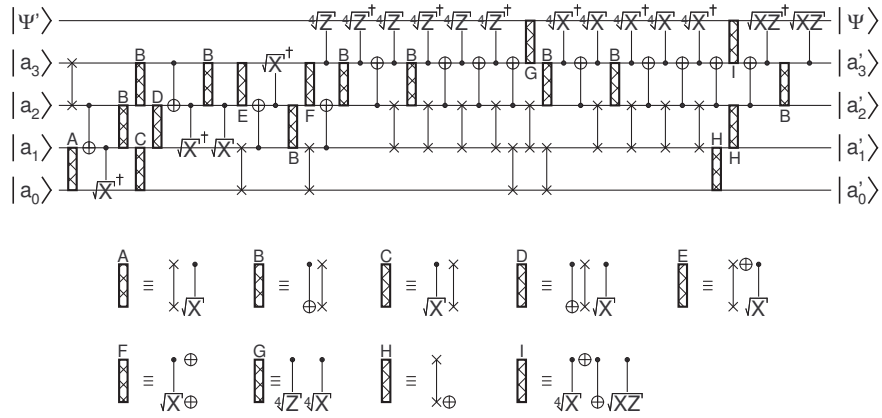


Fig. 6.3: Linear nearest neighbor version of Fig. 6.2.



$p$	$T_{opt}$	$\epsilon_{step}$	$\epsilon_{step}/p$
$10^{-3}$	120	$1.4 \times 10^{-3}$	$1.4 \times 10^0$
$3.7 \times 10^{-4}$	190	$3.7 \times 10^{-4}$	$1.0 \times 10^0$
$10^{-4}$	320	$6.0 \times 10^{-5}$	$6.0 \times 10^{-1}$
$10^{-5}$	1100	$2.1 \times 10^{-6}$	$2.1 \times 10^{-1}$
$2.2 \times 10^{-6}$	2300	$2.2 \times 10^{-7}$	$1.0 \times 10^{-1}$
$10^{-6}$	3000	$7.1 \times 10^{-8}$	$7.1 \times 10^{-2}$
$10^{-7}$	15000	$1.9 \times 10^{-9}$	$1.9 \times 10^{-2}$
$2.1 \times 10^{-8}$	40000	$2.1 \times 10^{-10}$	$1.0 \times 10^{-2}$

Tab. 6.2: Probability per time step  $\epsilon_{step}$  of the logical qubit being destroyed when using no measurement 5-qubit QEC vs physical probability  $p$  per qubit per time step of a discrete error.

$\sigma$	$T_{opt}$	$p$	$\epsilon_{step}$	$\epsilon_{step}/p$
$3.1 \times 10^{-2}$	$1.0 \times 10^2$	$4.6 \times 10^{-4}$	$4.6 \times 10^{-4}$	$1.0 \times 10^0$
$10^{-2}$	$3.2 \times 10^2$	$4.9 \times 10^{-5}$	$2.2 \times 10^{-5}$	$4.5 \times 10^{-1}$
$2.0 \times 10^{-3}$	$1.8 \times 10^3$	$2.0 \times 10^{-6}$	$2.0 \times 10^{-7}$	$1.0 \times 10^{-1}$
$10^{-3}$	$3.7 \times 10^3$	$5.0 \times 10^{-7}$	$2.4 \times 10^{-8}$	$4.8 \times 10^{-2}$
$2.1 \times 10^{-4}$	$2.4 \times 10^4$	$2.1 \times 10^{-8}$	$2.1 \times 10^{-10}$	$1.0 \times 10^{-2}$
$10^{-4}$	$5.0 \times 10^4$	$5.0 \times 10^{-9}$	$1.8 \times 10^{-11}$	$3.6 \times 10^{-3}$
$10^{-5}$	$4.0 \times 10^5$	$5.1 \times 10^{-11}$	$1.5 \times 10^{-14}$	$2.9 \times 10^{-4}$

Tab. 6.3: Probability per time step  $\epsilon_{step}$  of the logical qubit being destroyed when using no measurement 5-qubit QEC vs standard deviation  $\sigma$  of continuous errors.

$p = 3.7 \times 10^{-4}$ ,  $2.2 \times 10^{-6}$ , and  $2.1 \times 10^{-8}$  respectively. Note that these are approximately a factor of 5 less than the corresponding results obtained in Chapter 5. For continuous errors, the pertinent standard deviations are  $\sigma = 3.1 \times 10^{-2}$ ,  $2.0 \times 10^{-3}$ , and  $2.1 \times 10^{-4}$ . These are very comparable to the results obtained in Chapter 5, being at most a factor of 2 less.

### 6.3 5-qubit QEC with slow resetting

The use of Fig. 6.3 in a 5-qubit system assumes the reset operation is fast (comparable to the time required to implement a single quantum gate). This requirement can be eliminated with the addition of four ancilla qubits as shown in Fig. 6.4. By re-encoding with fresh ancilla, the reset operation may now take an amount of time equal to an entire QEC cycle. From Tables 6.2 and 6.3, depending on the physical error rate, this can be thousands of times longer than a single gate operation.

### 6.4 Conclusion

To summarize, we have shown that even without fault-tolerance, fast measurement, classical processing, and large numbers of qubits, it is still possible to construct a general quantum error correction scheme with a reasonably high ( $p = 3.7 \times 10^{-4}$  or  $\sigma = 3.1 \times 10^{-2}$ ) threshold error rate.

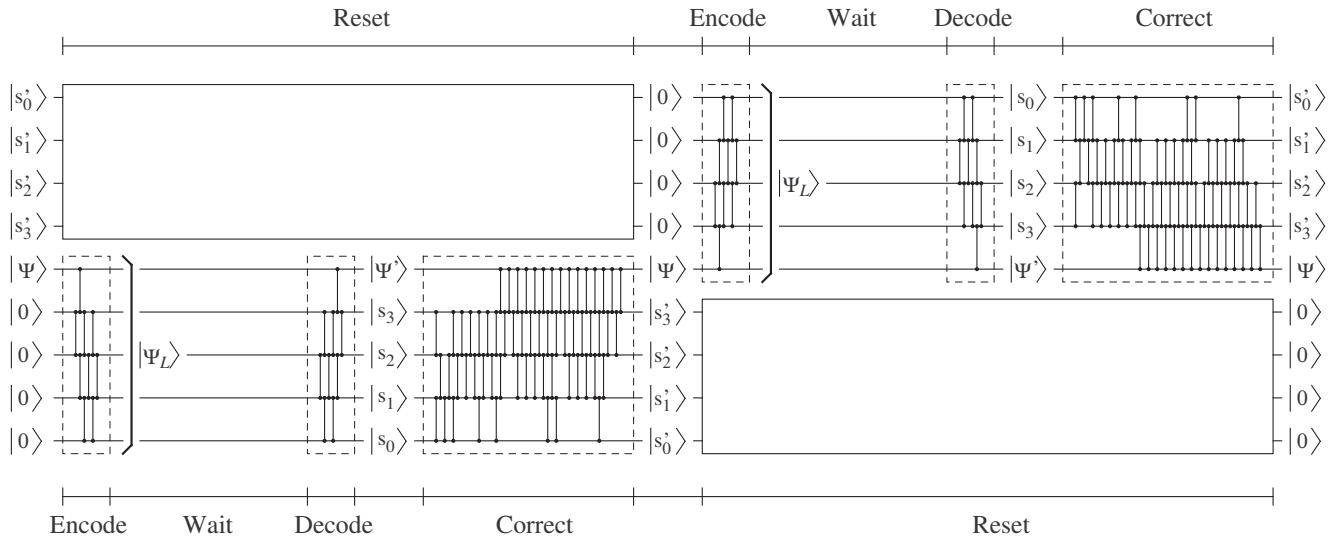


Fig. 6.4: 5-qubit quantum error correction scheme not requiring fast measurement or classical processing.



## 7. Shor's algorithm

Chapters 8, 9 and to a lesser extent Chapter 10 deal with aspects of implementing Shor's algorithm [6, 184]. This chapter provides a detailed review of the algorithm. In addition to Shor's papers, we draw heavily on Ref. [30].

When Shor's algorithm was published in 1994, it was greeted with great excitement due to its potential to break the popular RSA encryption protocol [7]. RSA is used in all aspects of e-commerce from Internet banking to secure online payment and can also be used to facilitate secure message transmission. The security of RSA is conditional on large integers being difficult to factorize, which has so far proven to be the case when using classical computers. Given a quantum computer, Shor's algorithm renders the integer factoring problem tractable.

To be precise, let  $N = N_1 N_2$  be a product of prime numbers. Let  $L = \ln_2 N$  be the binary length of  $N$ . Given  $N$ , Shor's algorithm enables the determination of  $N_1$  and  $N_2$  in a time polynomial in  $L$ . This is achieved indirectly by finding the period  $r$  of  $f(k) = m^k \bmod N$ , where  $1 < m < N$ ,  $\gcd(m, N) = 1$  and  $\gcd$  denotes the greatest common divisor. Provided  $r$  is even and  $f(r/2) \neq N - 1$ , the factors are  $N_1 = \gcd(f(r/2) + 1, N)$  and  $N_2 = \gcd(f(r/2) - 1, N)$ . Note that the greatest common divisor can be computed in a time linear in  $L$  using a classical computer. For odd  $N$  and randomly selected  $m$  such that  $1 < m < N$  and  $\gcd(m, N) = 1$ , the probability that  $f(k)$  has a suitable  $r$  is at least 0.75 [30]. Thus on average

Circuit	Qubits	Depth
Beauregard [191]	$\sim 2L$	$\sim 32L^3$
Vedral [186]	$\sim 5L$	$240L^3$
Zalka 1 [190]	$\sim 5L$	$\sim 3000L^2$
Zalka 2 [190]	$\sim 50L$	$\sim 2^{19}L^{1.2}$
Van Meter [185]	$O(L^2)$	$O(L \log^2 L)$

Tab. 7.1: Required number of qubits and circuit depth of different implementations of the quantum part of Shor's algorithm. Where possible, figures are accurate to leading order in  $L$ .

very few values of  $m$  need to be tested to factor  $N$ .

The quantum part of Shor's algorithm can be viewed as a subroutine that generates numbers of the form  $j \simeq c2^{2L}/r$ . To distinguish this from the necessary classical pre- and post-processing, this subroutine will be referred to as quantum period finding (QPF). Due to decoherence and imprecise gates, the probability  $s$  that QPF will successfully generate useful data (defined precisely below) may be quite low with many repetitions required to work out the period  $r$  of a given  $f(k) = m^k \bmod N$ . Using this terminology, Shor's algorithm consists of classical preprocessing, potentially many repetitions of QPF with classical postprocessing and possibly a small number of repetitions of the entire cycle followed by more classical post-processing (Fig. 7.1).

The efficiency of QPF can only be quantified with reference to a specific quantum circuit implementation. To date, the most thorough work on different quantum circuit implementations has been performed by Van Meter [185] drawing on work by Vedral [186], Beckman [187], Gossett [188], Draper [189] and Zalka [190]. Table 7.1 gives representative examples of the variety of circuits in existence and their qubit counts and depths as a function of  $L$ . Note that generally speaking time can be saved at the cost of more qubits.

An underlying procedure common to all implementations does exist. The

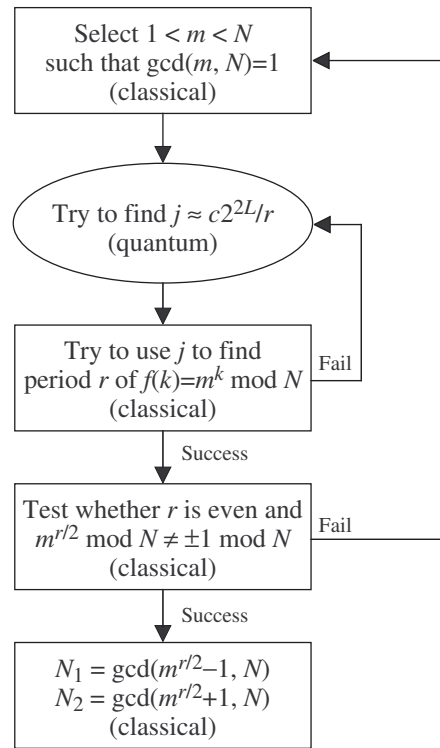


Fig. 7.1: The complete Shor's algorithm including classical pre- and postprocessing. The first branch is highly likely to fail, resulting in many repetitions of the quantum heart of the algorithm, whereas the second branch is highly likely to succeed.

first common step involves initializing the quantum computer to a single pure state  $|0\rangle_{2L}|0\rangle_L$ . Note that for clarity the computer state has been broken into a  $2L$  qubit  $k$  register and an  $L$  qubit  $f$  register. The meaning of this will become clearer below.

Step two is to Hadamard transform each qubit in the  $k$ -register yielding

$$\frac{1}{2^L} \sum_{k=0}^{2^{2L}-1} |k\rangle_{2L} |0\rangle_L. \quad (7.1)$$

Step three is to calculate and store the corresponding values of  $f(k)$  in the  $f$ -register

$$\frac{1}{2^L} \sum_{k=0}^{2^{2L}-1} |k\rangle_{2L} |f(k)\rangle_L. \quad (7.2)$$

Note that this step requires additional ancilla qubits. The exact number depends heavily on the circuit used.

Step four can actually be omitted but it explicitly shows the origin of the period  $r$  being sought. Measuring the  $f$ -register yields

$$\frac{\sqrt{r}}{2^L} \sum_{n=0}^{2^{2L}/r-1} |k_0 + nr\rangle_{2L} |f_M\rangle_L \quad (7.3)$$

where  $k_0$  is the smallest value of  $k$  such that  $f(k)$  equals the measured value  $f_M$ .

Step five is to apply the quantum Fourier transform

$$|k\rangle \rightarrow \frac{1}{2^L} \sum_{j=0}^{2^{2L}-1} \exp\left(\frac{2\pi i}{2^{2L}} jk\right) |j\rangle \quad (7.4)$$

to the  $k$ -register resulting in

$$\frac{\sqrt{r}}{2^{2L}} \sum_{j=0}^{2^{2L}-1} \sum_{p=0}^{2^{2L}/r-1} \exp\left(\frac{2\pi i}{2^{2L}} j(k_0 + pr)\right) |j\rangle_{2L} |f_M\rangle_L. \quad (7.5)$$



The meaning of equation 7.5 is best illustrated by reversing the order of the summation

$$\frac{\sqrt{r}}{2^{2L}} \sum_{j=0}^{2^{2L}-1} \sum_{p=0}^{2^{2L}/r-1} \exp\left(\frac{2\pi i}{2^{2L}} j(k_0 + pr)\right) |j\rangle_{2L} |f_M\rangle_L. \quad (7.6)$$

The probability of measuring a given value of  $j$  is thus

$$\Pr(j, r, L) = \left| \frac{\sqrt{r}}{2^{2L}} \sum_{p=0}^{2^{2L}/r-1} \exp\left(\frac{2\pi i}{2^{2L}} jpr\right) \right|^2. \quad (7.7)$$

If  $r$  divides  $2^{2L}$ , Eq. (7.7) can be evaluated exactly. In this case the probability of observing  $j = c2^{2L}/r$  for some integer  $0 \leq c < r$  is  $1/r$  whereas if  $j \neq c2^{2L}/r$  the probability is 0. This situation is illustrated in Fig. 7.2a. However if  $r$  divides  $2^{2L}$  exactly a quantum computer is not needed as  $r$  would then be a power of 2 and easily calculable. When  $r$  is not a power of 2 the perfect peaks of Fig. 7.2a become slightly broader as shown in Fig. 7.2b. All one can then say is that with high probability the value  $j$  measured will satisfy  $j \simeq c2^{2L}/r$  for some  $0 \leq c < r$ .

Given a measurement  $j \simeq c2^{2L}/r$  with  $c \neq 0$ , classical postprocessing is required to extract information about  $r$ . The process begins with a continued fraction expansion. To illustrate, consider factoring 143 ( $L = 8$ ). Suppose we choose  $m$  equal 2 and the output  $j$  of QPF is 31674. The relation  $j \simeq c2^{2L}/r$  becomes  $31674 \simeq c65536/r$ . The continued fraction expansion of  $c/r$  is

$$\frac{31674}{65536} = \frac{1}{\frac{32768}{15837}} = \frac{1}{2 + \frac{1094}{15837}} = \frac{1}{2 + \frac{1}{14 + \frac{1}{2 + \frac{1}{10 + \frac{1}{52}}}}}. \quad (7.8)$$

The continued fraction expansion of any number between 0 and 1 is completely specified by the list of denominators which in this case is  $\{2, 14, 2, 10, 52\}$ .

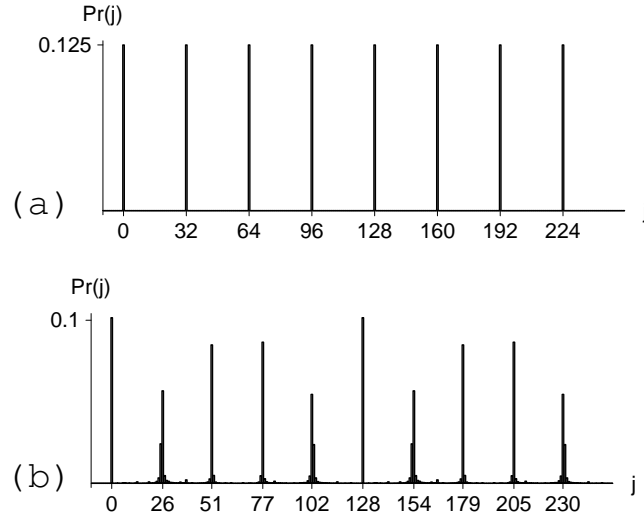


Fig. 7.2: Probability of different measurements  $j$  at the end of quantum period finding with total number of states  $2^{2L} = 256$  and (a) period  $r = 8$ , (b) period  $r = 10$ .

The  $n$ th convergent of a continued fraction expansion is the proper fraction equivalent to the first  $n$  elements of this list.

$$\begin{aligned}
 \{2\} &= \frac{1}{2} \\
 \{2, 14\} &= \frac{14}{29} \\
 \{2, 14, 2\} &= \frac{29}{60} \\
 \{2, 14, 2, 10\} &= \frac{304}{629} \\
 \{2, 14, 2, 10, 52\} &= \frac{15837}{32768}
 \end{aligned} \tag{7.9}$$

An introductory exposition and further properties of continued fractions are described in Ref. [30]. The period  $r$  can be sought by substituting each denominator into the function  $f(k) = 2^k \bmod 143$ . With high probability only the largest denominator less than  $2^L$  will be of interest. In this case  $2^{60} \bmod 143 = 1$  and hence  $r = 60$ .

Two modifications to the above are required. Firstly, if  $c$  and  $r$  have common factors, none of the denominators will be the period but rather one will be a divisor of  $r$ . After repeating QPF a number of times, let  $\{j_m\}$  denote the set of measured values. Let  $\{c_{mn}/d_{mn}\}$  denote the set of convergents associated with each measured value  $\{j_m\}$ . If a pair  $c_{mn}, c_{m'n'}$  exists such that  $\gcd(c_{mn}, c_{m'n'}) = 1$  and  $d_{mn}, d_{m'n'}$  are divisors of  $r$  then  $r = \text{lcm}(d_{mn}, d_{m'n'})$ , where  $\text{lcm}$  denotes the least common multiple. It can be shown that given any two divisors  $d_{mn}, d_{m'n'}$  with corresponding  $c_{mn}, c_{m'n'}$  the probability that  $\gcd(c_{mn}, c_{m'n'}) = 1$  is at least  $1/4$  [30]. Thus, on average, only a small number of different divisors are required. In practice, it will not be known which denominators are divisors so every pair  $d_{mn}, d_{m'n'}$  with  $\gcd(c_{mn}, c_{m'n'}) = 1$  must be tested.

The second modification is simply allowing for the possibility that the output  $j$  of QPF may be useless. Let  $s$  denote the probability that  $j = \lfloor c2^{2L}/r \rfloor$  or  $\lceil c2^{2L}/r \rceil$  for some  $0 < c < r$  where  $\lfloor \cdot \rfloor, \lceil \cdot \rceil$  denote rounding down and up respectively. Such values of  $j$  will be called useful as the denominators of the associated convergents are guaranteed to include a divisor of  $r$  [30]. To obtain a divisor of  $r$ ,  $O(1/s)$  runs of QPF must be performed.

To summarize, as each new value  $j_m$  is measured, the denominators  $d_{mn}$  less than  $2^L$  of the convergents of the continued fraction expansion of  $j_m/2^{2L}$  are substituted into  $f(k) = m^k \bmod N$  to determine whether any  $f(d_{mn}) = 1$  which would imply that  $r = d_{mn}$ . If not, every pair  $d_{mn}, d_{m'n'}$  with associated numerators  $c_{mn}, c_{m'n'}$  satisfying  $\gcd(c_{mn}, c_{m'n'}) = 1$  is tested to see whether  $r = \text{lcm}(d_{mn}, d_{m'n'})$ . Note that as shown in Fig. 7.1, if  $r$  is even or  $m^{r/2} \bmod N = \pm 1 \bmod N$  then the entire process needs to be repeated  $O(1)$  times. Thus Shor's algorithm always succeeds provided  $O(1/s)$  runs of QPF can be performed. Note that if  $s$  is too small, it may

not be possible to repeat QPF  $O(1/s)$  times in a practical amount of time.

## 8. Shor's algorithm on an LNN QC

Implementing Shor's factorization algorithm [6, 184] is arguably the ultimate goal of much experimental quantum computer research. A necessary test of any quantum computer proposal is therefore whether or not it can implement quantum period finding (QPF) as described in Chapter 7. While several different quantum circuits implementing QPF have been designed (Table 7.1), most tacitly assume that arbitrary pairs of qubits within the computer can be interacted. As discussed in Chapter 5, a large number of promising proposals, including the Kane quantum computer, are best suited to realizing a single line of qubits with nearest neighbor interactions only. Determining whether these linear nearest neighbor (LNN) architectures can implement QPF in particular and quantum algorithms in general in a practical manner is a nontrivial and important question. In this chapter we present a circuit implementing QPF designed for an LNN QC. As the rest of Shor's algorithm is classical, this implies that Shor's algorithm can be implemented on an LNN QC. Despite the interaction restrictions, the circuit presented uses just  $2L + 4$  qubits and to leading order requires  $8L^4$  gates arranged in a circuit of depth  $32L^3$  — identical to leading order to the Beauregard circuit [191] upon which this work is based. Note that the original Beauregard's circuit used just  $2L + 3$  qubits, but with the extra qubit repeated Toffoli gates can be implemented more quickly, reducing the overall depth of the circuit by a factor of 4. The precise differences between

the LNN and Beauregard circuit are detailed throughout the chapter.

As controlling large numbers of qubits has so far proven to be extraordinarily difficult, this work places emphasis firstly on minimizing the required number of qubits. Secondly, the depth has been minimized over the total gate count in an effort to reduce the need for quantum error correction assuming the primary source of error will be decoherence rather than the quantum gates themselves. If gate errors dominate, a higher depth but lower gate count circuit would be preferable [186].

The chapter is structured as follows. In Section 8.1 Shor's algorithm is broken into a series of simple tasks appropriate for direct translation into circuits. Sections 8.2 to 8.6 then present, in order of increasing complexity, the LNN quantum circuits that together comprise the LNN Shor quantum circuit. The LNN quantum Fourier transform (QFT) is presented first, followed by a modular addition, the controlled swap, modular multiplication, and finally the complete circuit. Section 8.7 contains a summary of all results, and a description of further work.

### 8.1 *Decomposing Shor's algorithm*

The purpose of this section is to break Shor's algorithm into a series of steps that can be easily implemented as quantum circuits. Neglecting the classical computations and optional measurement step described in the previous chapter, Shor's algorithm has already been broken into four steps.

1. Hadamard transform.
2. Modular exponentiation.
3. Quantum Fourier transform.
4. Measurement.

The modular exponentiation step is the only one that requires further decomposition.

The calculation of  $f(k) = m^k \bmod N$  is firstly broken up into a series of controlled modular multiplications.

$$f(k) = \prod_{i=0}^{2L-1} (m^{2^i k_i} \bmod N), \quad (8.1)$$

where  $k_i$  denotes the  $i$ th bit of  $k$ . If  $k_i = 1$  the multiplication  $m^{2^i} \bmod N$  occurs, and if  $k_i = 0$  nothing happens.

There are many different ways to implement controlled modular multiplication (Table 7.1). The methods of [191] require the fewest qubits and will be used here. To illustrate how each controlled modular multiplication proceeds, let  $a(i) = m^{2^i} \bmod N$  and

$$x(i) = \prod_{j=0}^{i-1} (m^{2^j k_j} \bmod N). \quad (8.2)$$

$x(i)$  represents a partially completed modular exponentiation and  $a(i)$  the next term to multiply by. Let  $|x(i), 0\rangle$  denote a quantum register containing  $x(i)$  and another of equal size containing 0. Firstly, add  $a(i)$  modularly multiplied by the first register to second register if and only if (iff)  $k_i = 1$ .

$$\begin{aligned} |x(i), 0\rangle &\mapsto |x(i), 0 + a(i)x(i) \bmod N\rangle \\ &= |x(i), x(i+1)\rangle. \end{aligned} \quad (8.3)$$

Secondly, swap the registers iff  $k_i = 1$ .

$$|x(i), x(i+1)\rangle \mapsto |x(i+1), x(i)\rangle \quad (8.4)$$

Thirdly, subtract  $a(i)^{-1}$  modularly multiplied by the first register from the second register iff  $k_i = 1$ .

$$\begin{aligned}
& |x(i+1), x(i)\rangle \\
\mapsto & |x(i+1), x(i) - a(i)^{-1}x(i+1) \bmod N\rangle \\
= & |x(i+1), 0\rangle.
\end{aligned} \tag{8.5}$$

Note that while nothing happens if  $k_i = 0$ , by the definition of  $x(i)$  the final state in this case will still be  $|x(i+1), 0\rangle$ .

The first and third steps described in the previous paragraph are further broken up into series of controlled modular additions and subtractions respectively.

$$0 + a(i)x(i) = 0 + \sum_{j=0}^{L-1} a(i)2^j x(i)_j \bmod N, \tag{8.6}$$

$$x(i) - a(i)^{-1}x(i+1) = x(i) - \sum_{j=0}^{L-1} a(i)^{-1}2^j x(i+1)_j \bmod N, \tag{8.7}$$

where  $x(i)_j$  and  $x(i+1)_j$  denote the  $j$ th bit of  $x(i)$  and  $x(i+1)$  respectively. Note that the additions associated with a given  $x(i)_j$  can only occur if  $x(i)_j = 1$  and similarly for the subtractions. Given that these additions and subtractions form a multiplication that is conditional on  $k_i$ , it is also necessary that  $k_i = 1$ .

Further decomposition will be left for subsequent sections.



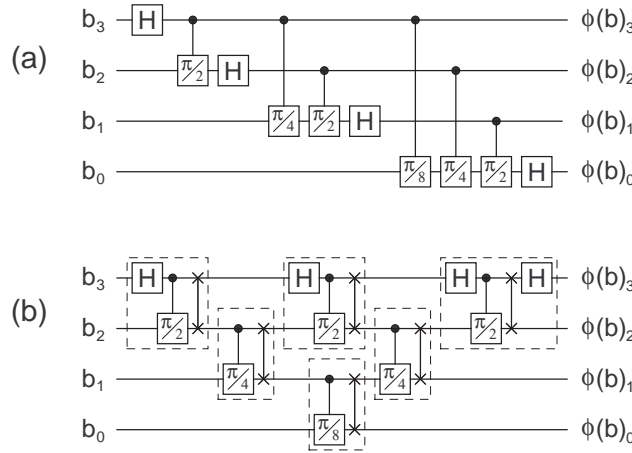


Fig. 8.1: (a) Standard quantum Fourier transform circuit. (b) An equivalent linear nearest neighbor circuit.

## 8.2 Quantum Fourier Transform

The first circuit that needs to be described, as it will be used in all subsequent circuits, is the QFT.

$$|k\rangle \rightarrow \frac{1}{\sqrt{2^L}} \sum_{j=0}^{2^L-1} \exp(2\pi i j k / 2^L) |j\rangle \quad (8.8)$$

Fig. 8.1a shows the usual circuit design for an architecture that can interact arbitrary pairs of qubits. Fig. 8.1b shows the same circuit rearranged with the aid of swap gates to allow it to be implemented on an LNN architecture. Note that the general QFT circuit inverts the most significant to least significant ordering of the qubits whereas the LNN circuit does not. Dashed boxes indicate compound gates implemented with the aid of the canonical decomposition. To emphasize the advantage of using compound gates, Fig. 8.2 contains a comparison of a single swap gate with a Hadamard gate followed by a controlled phase rotation, followed by a swap gate.

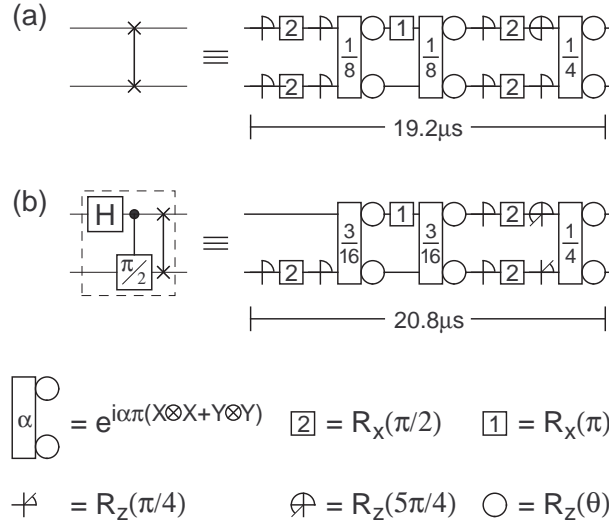


Fig. 8.2: (a) Swap gate expressed as a sequence of physical operations via the canonical decomposition. (b) Similarly decomposed compound gate consisting of a Hadamard gate, controlled phase rotation, and swap gate. Note that the Kane architecture has been used for illustrative purposes.

Counting compound gates as one, the total number of gates required to implement a QFT on  $L$  qubits for both the general and LNN architectures is  $L(L-1)/2$ . Assuming gates can be implemented in parallel, the minimum circuit depth for both is  $2L-3$ . Note that for large  $L$  it is both necessary and possible for nearly all of the exponentially small controlled rotation gates to be omitted [192, 136]. Omitting these gates does not, however, enable a reduction in the depth of the circuit. This point will be discussed in detail in Chapter 9. Furthermore, in the LNN case the swap gates associated with omitted controlled rotations must remain for the circuit to work so the gate count also remains unchanged.

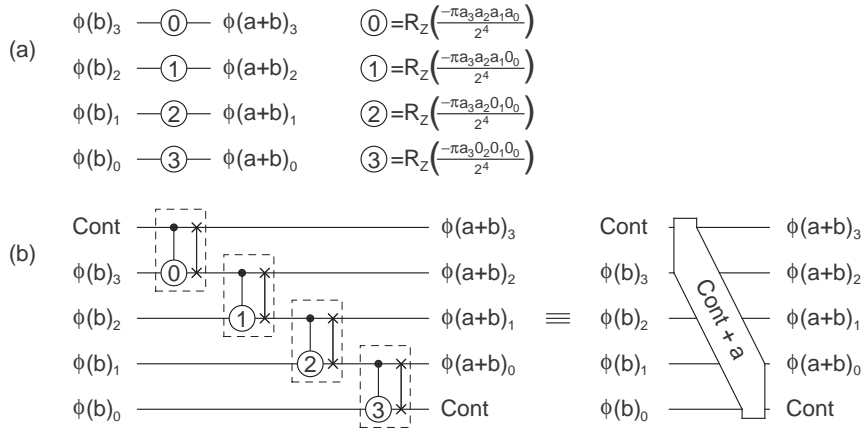


Fig. 8.3: (a) Quantum Fourier addition. (b) Controlled quantum Fourier addition and its symbolic equivalent circuit.  $Cont + a$  denotes the addition of  $a$  if  $Cont = 1$ .

### 8.3 Modular Addition

Given a quantum register containing an arbitrary superposition of binary numbers, there is a particularly easy way to add a binary number to each number in the superposition [193, 191]. By quantum Fourier transforming the superposition, the addition can be performed simply by applying appropriate single-qubit rotations as shown in Fig. 8.3a. Such an addition can also very easily be made dependant on a single control qubit as shown in Fig. 8.3b.

Performing controlled modular addition is considerably more complicated as shown in Fig. 8.4. This circuit adds  $2^j m^{2^i} \bmod N$  iff both  $x(i)_j$  and  $k_i$  are 1 to the register containing  $\phi(b)$  to obtain  $\phi(c)$  where  $c = (b + 2^j m^{2^i}) \bmod N$ . Note that the register containing  $\phi(b)$  is  $L + 1$  qubits in length to prevent overflow at any stage of the computation.

The first five gates comprise a Toffoli gate that sets  $kx = 1$  iff  $x(i)_j = k_i = 1$ .  $k_i$  and  $x(i)_j$  are defined in Eq. (8.1) and Eqs (8.6–8.7) respectively.

Note that the Beauregard circuit does not have a  $kx$  qubit, but without it the singly-controlled Fourier additions become doubly-controlled and take four times as long. The calculations of the gate count and circuit depth of the Beauregard circuit presented here have therefore been done with a  $kx$  qubit included.

The next circuit element firstly adds  $2^j m^{2^i} \bmod N$  iff  $kx = 1$  then subtracts  $N$ . If  $b + (2^j m^{2^i} \bmod N) < N$ , subtracting  $N$  will result in a negative number. In a binary register, this means that the most significant bit will be 1. The next circuit element is an inverse QFT which takes the addition result out of Fourier space and allows the most significant bit to be accessed by the following CNOT. The *MS* (Most Significant) qubit will now be 1 iff the addition result was negative. If  $b + (2^j m^{2^i} \bmod N) > N$ , subtracting  $N$  will yield the positive number  $(b + 2^j m^{2^i}) \bmod N$  and the *MS* qubit will remain set to 0.

We now encounter the first circuit element that would not be present if interactions between arbitrary pairs of qubits were possible. Note that while this “long swap” operation technically consists of  $L$  regular swap gates, it only increases the depth of the circuit by 1. The subsequent QFT enables the *MS* controlled Fourier addition of  $N$  yielding the positive number  $(b + 2^j m^{2^i}) \bmod N$  if  $MS = 1$  and leaving the already correct result unchanged if  $MS = 0$ .

While it might appear that we are now done, the qubits *MS* and *kx* must be reset so they can be reused. The next circuit element subtracts  $2^j m^{2^i} \bmod N$ . The result will be positive and hence the most significant bit of the result equal to 0 iff the very first addition  $b + (2^j m^{2^i} \bmod N)$  gave a number less than  $N$ . This corresponds to the  $MS = 1$  case. After another inverse QFT to allow the most significant bit of the result to be accessed, the

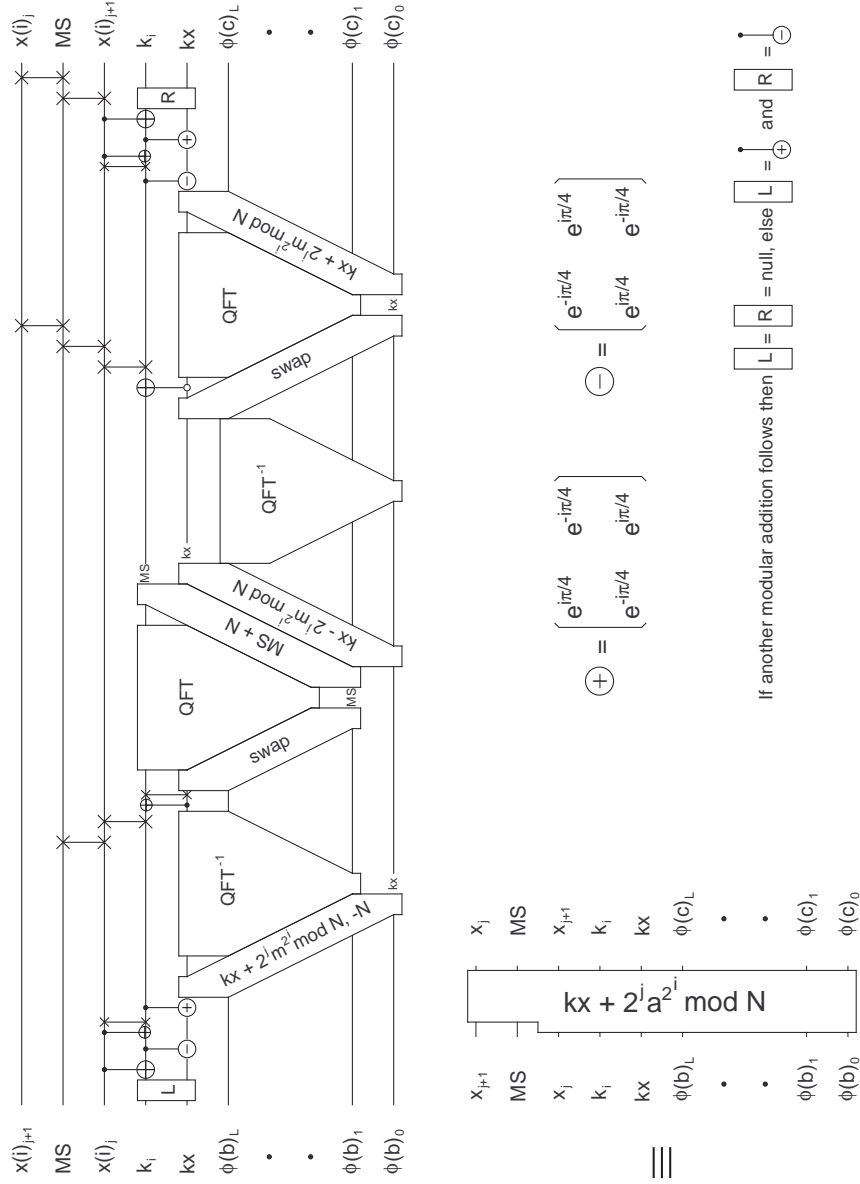


Fig. 8.4: Circuit to compute  $c = (b + 2^j m^{2^i}) \bmod N$ . The diagonal circuit elements labelled swap represent a series of 2-qubit swap gates. Small gates spaced close together represent compound gates. The qubits  $x(i)$  are defined in Eq. 8.2 and essentially store the current partially calculated value of the modular exponentiation that forms the heart of Shor's algorithm. The  $MS$  (Most Significant) qubit is used to keep track of the sign of the partially calculated modular addition result. The  $k_i$  qubit is the  $i$ th bit of  $k$  in Eq. 8.1. The  $kx$  qubit is set to 1 if and only if  $x(i)_j = k_i = 1$ .  $kx \pm 2^j m^{2^i} \bmod N$  denotes modular addition (subtraction) conditional on  $kx = 1$ .

$MS$  qubit is reset by a CNOT gate that flips the target qubit iff the control qubit is 0. Note that the long swap operation that occurs in the middle of all this to move the  $kx$  qubit to a more convenient location only increases the depth of the circuit by 1.

After adding back  $2^j m^{2^i} \bmod N$ , the next few gates form a Toffoli gate that resets  $kx$ . The final two swap gates move  $x(i)_{j+1}$  into position ready for the next modular addition. Note that the  $L$  and  $R$  gates are inverses of one another and hence not required if modular additions precede and follow the circuit shown. Only one of the final two swap gates contributes to the overall depth of the circuit.

The total gate count of the LNN modular addition circuit is  $2L^2 + 8L + 22$  and compares very favorably with the general architecture gate count of  $2L^2 + 6L + 14$ . Similarly, the LNN depth is  $8L + 16$  versus the general depth of  $8L + 13$ .

#### 8.4 Controlled swap

Performing a controlled swap of two large registers is slightly more difficult when only LNN interactions are available. The two registers need to be meshed so that pairs of equally significant qubits can be controlled-swapped. The mesh circuit is shown in Fig. 8.5. This circuit element would not be required in a general architecture.

After the mesh circuit has been applied, the functional part of the controlled swap circuit (Fig. 8.6) can be applied optimally with the control qubit moving from one end of the meshed registers to the other. The mesh circuit is then applied in reverse to untangle the two registers.

The gate count and circuit depth of a mesh circuit is  $L(L-1)/2$  and  $L-1$  respectively. The corresponding equations for a complete LNN controlled

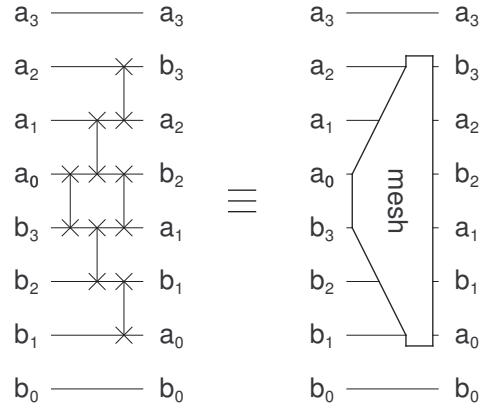


Fig. 8.5: Circuit designed to interleave two quantum registers.

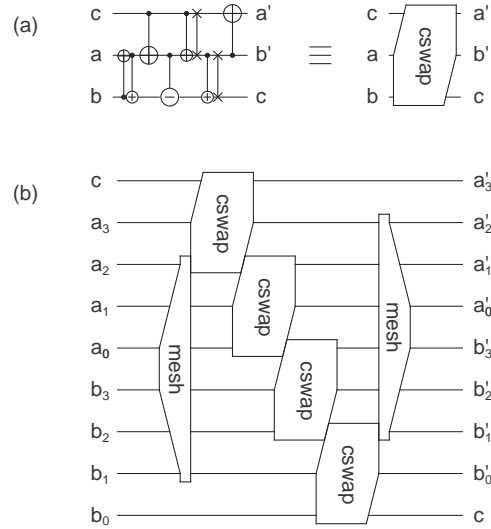


Fig. 8.6: (a) LNN circuit for the controlled swapping of two qubits  $|a\rangle$  and  $|b\rangle$ . The qubits  $|a'\rangle$  and  $|b'\rangle$  represent the potentially swapped states. (b) LNN circuit for the controlled swapping of two quantum registers. Note that when chained together, the effective depth of the cswap gate is 4.

swap are  $L^2 + 5L$  and  $6L$ . The general controlled swap only requires  $6L$  gates and can be implemented in a circuit of depth  $4L + 2$ . The controlled swap is the only part of this implementation of Shor's algorithm that is significantly more difficult to implement on an LNN architecture.

### 8.5 Modular Multiplication

The ideas behind the modular multiplication circuit of Fig. 8.7 were discussed in Section 8.1. The first third comprises a controlled modular multiply (via repeated addition) with the result being stored in a temporary register. The middle third implements a controlled swap of registers. The final third resets the temporary register.

Note that the main way in which the performance of the LNN circuit differs from the ideal general case is due to the inclusion of the two mesh circuits. Nearly all of the remaining swaps shown in the circuit do not contribute to the overall depth. Note that the two swaps drawn within the QFT and inverse QFT are intended to indicate the appending of a swap gate to the first and last compound gates in these circuits respectively.

The total gate count for the LNN modular multiplication circuit is  $4L^3 + 20L^2 + 58L - 2$  versus the general gate count of  $4L^3 + 13L^2 + 35L + 4$ . The LNN depth is  $16L^2 + 40L - 7$  and the general depth  $16L^2 + 33L - 6$ .

### 8.6 Complete Circuit

The complete circuit for Shor's algorithm (Fig. 8.8) can best be understood with reference to Fig. 8.1a and the four steps described in Section 8.1. The last two steps of Shor's algorithm are a QFT and measurement of the qubits involved in the QFT. When a 2-qubit controlled quantum gate is followed by measurement of the controlled qubit, it is equivalent to measure the control



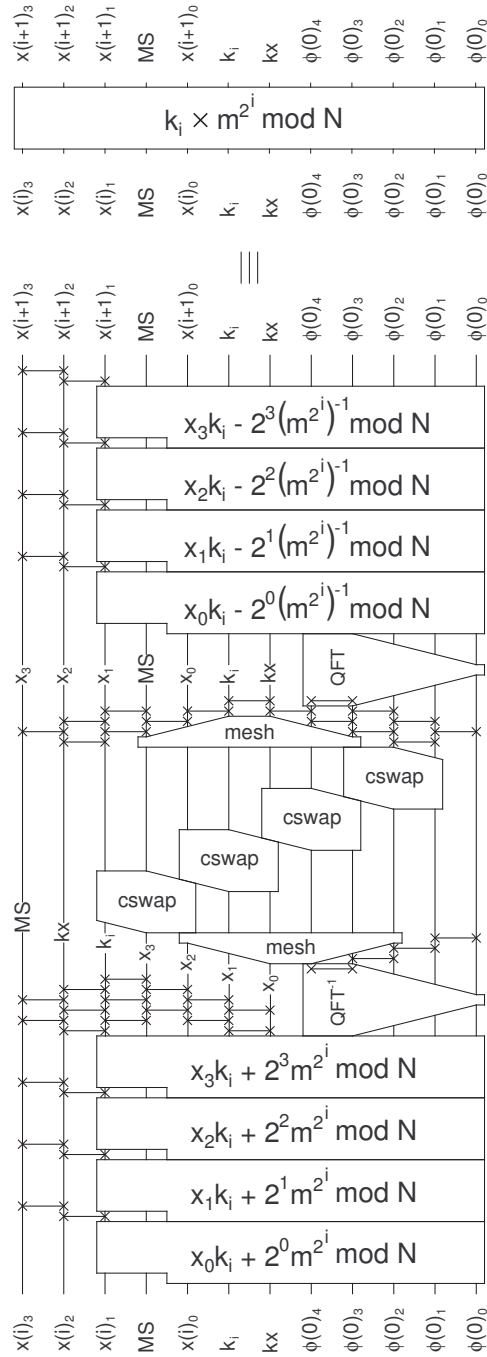


Fig. 8.7: Circuit designed to modularly multiply  $x(i)$  by  $m^{2^i}$  if and only if  $k_i = 1$ . Note that for simplicity the circuit for  $L = 4$  has been shown. Note that the bottom  $L + 1$  qubits are ancilla and as such start and end in the  $|\phi(0)\rangle$  state. The swap gates within the two QFT structures represent compound gates.  $k_i \times m^{2^i} \bmod N$  denotes modular multiplication conditional on  $k_i = 1$ .

qubit first and then apply a classically controlled gate to the target qubit. If this is done to every qubit in Fig. 8.1a, it can be seen that every qubit is decoupled. Furthermore, since the QFT is applied to the  $k$  register and the  $k$  register qubits are never interacted with one another, it is possible to arrange the circuit such that each qubit in the  $k$  register is sequentially used to control a modular multiplication, QFTed, then measured. Even better, after the first qubit of the  $k$  register is manipulated in this manner, it can be reset and used as the second qubit of the  $k$  register. This one qubit trick [194] forms the basis of Fig. 8.8.

The total number of gates required in the LNN and general cases are  $8L^4 + 40L^3 + 116\frac{1}{2}L^2 + 4\frac{1}{2}L - 2$  and  $8L^4 + 26L^3 + 70\frac{1}{2}L^2 + 8\frac{1}{2}L - 1$  respectively. The circuit depths are  $32L^3 + 80L^2 - 4L - 2$  and  $32L^3 + 66L^2 - 2L - 1$  respectively. The primary result of this chapter is that the gate count and depth equations for both architectures are identical to leading order.

### 8.7 Conclusion

We have presented a circuit implementing Shor's algorithm in a manner appropriate for a linear nearest neighbor qubit array and studied the number of extra gates and consequent increase in circuit depth such a design entails. To leading order our circuit involves  $8L^4$  gates arranged in a circuit of depth  $32L^3$  on  $2L + 4$  qubits — figures identical to that possible when interactions between arbitrary pairs of qubits are allowed. Given the importance of Shor's algorithm, this result supports the widespread experimental study of linear nearest neighbor architectures.

Simulations of the robustness of the circuit when subjected to random discrete errors have been completed [195], showing extreme sensitivity to even small numbers of errors. Future simulations will investigate the per-

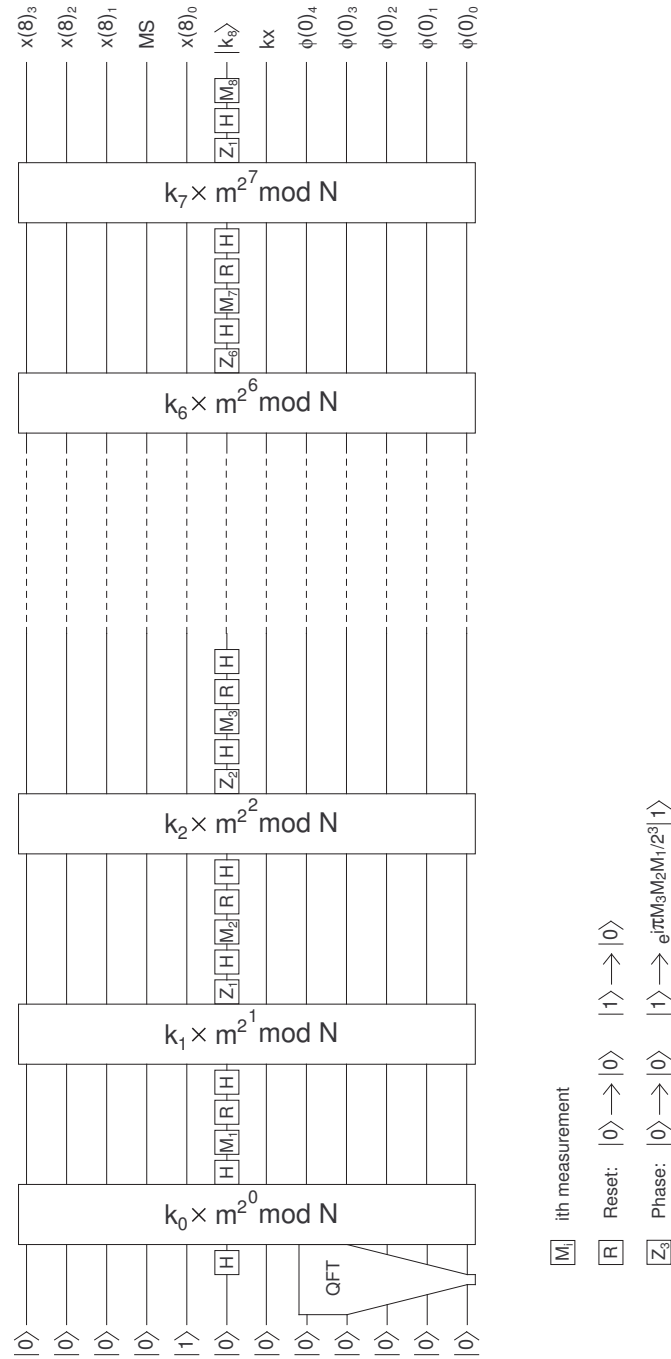


Fig. 8.8: Circuit implementing the quantum part of Shor's algorithm. The single-qubit gates interleaved between the modular multiplications comprise a QFT that has been decomposed by using measurement gates to remove the need for controlled quantum phase rotations. Note that without these single-qubit gates the remaining circuit is simply modular exponentiation.

formance of the circuit when protected by LNN quantum error correction.

## 9. Shor's algorithm with a limited set of rotation gates

Every circuit implementation of Shor's algorithm (see Table 7.1) ideally calls for controlled rotation gates of magnitude  $\pi/2^{2L}$  where  $L$  is the binary length of the integer  $N$  to be factored. Such exponentially small rotations are physically impossible to implement for large  $L$ . Prior work by Coppersmith focusing solely on a quantum Fourier transform suggested that it would be sufficient to implement controlled  $\pi/10^6$  rotations if integers thousands of bits long were desired factored [192]. In this chapter, we study in detail the complete Shor's algorithm using only controlled  $\pi/2^d$  rotation gates with  $d$  less than or equal to some  $d_{\max}$ . It is found that integers up to length  $L_{\max} = O(4^{d_{\max}})$  can be factored without significant performance penalty. Consequently, we are able to show that controlled rotation gates of magnitude  $\pi/64$  are sufficient to factor integers thousands of bits long.

The reader is assumed to be familiar with the description of Shor's algorithm and notation as outlined in Chapter 7. In Section 9.1, Coppersmith's approximate quantum Fourier transform is introduced. In Section 9.2, we investigate the relationship between the period  $r$  of the function  $f(k)$  given as input to the quantum part of Shor's algorithm, and the probability  $s$  of obtaining useful output. In Section 9.3, we study the relationship between  $s$  and both the length  $L$  of the integer  $N$  being factored and the minimum

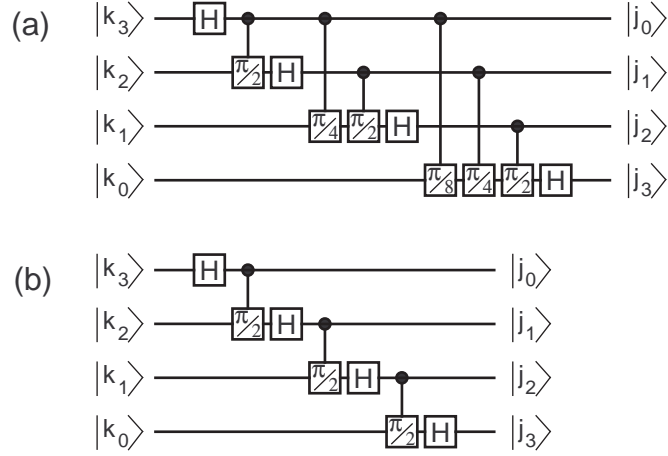


Fig. 9.1: Circuit for a 4-qubit (a) quantum Fourier transform and (b) approximate quantum Fourier transform with  $d_{\max} = 1$ .

angle controlled rotation  $\pi/2^{d_{\max}}$ . This is then used to relate  $L_{\max}$  to  $d_{\max}$ . Section 9.4 contains a summary of results.

### 9.1 Approximate quantum Fourier transform

Provided any circuit from Table 7.1 other than Beauregard's is used to implement Shor's algorithm, exponentially small rotations only occur in the one and only quantum Fourier transform required just before measurement. The standard QFT circuit is shown in Fig. 9.1a. Note the use of controlled rotations of magnitude  $\pi/2^d$ . In matrix notation these 2-qubit operations correspond to

$$\begin{pmatrix} 1 & 0 & 0 & 0 \\ 0 & 1 & 0 & 0 \\ 0 & 0 & 1 & 0 \\ 0 & 0 & 0 & e^{i\pi/2^d} \end{pmatrix}. \quad (9.1)$$

Coppersmith's approximate QFT (AQFT) circuit [192] is very similar

with just the deletion of rotation gates with  $d$  greater than some  $d_{\max}$ . For example, Fig. 9.1b shows an AQFT with  $d_{\max} = 1$ . Let  $[j]_m$  denote the  $m$ th bit of  $j$ . The action of the AQFT on a computational basis state  $|k\rangle$  is

$$|k\rangle \rightarrow \frac{1}{\sqrt{2^{2L}}} \sum_{j=0}^{2^{2L}-1} |j\rangle \exp\left(\frac{2\pi i}{2^{2L}} \tilde{\sum}_{mn} [j]_m [k]_n 2^{m+n}\right) \quad (9.2)$$

where  $\tilde{\sum}_{mn}$  denotes a sum over all  $m, n$  such that  $0 \leq m, n < 2L$  and  $2L - d_{\max} + 1 \leq m + n < 2L$ . It has been shown by Coppersmith that the AQFT is a good approximation of the QFT [192] in the sense that the phase of individual computational basis states in the output of the AQFT differ in angle from those in the output of the QFT by at most  $2\pi L/2^{d_{\max}}$ . The purpose of this chapter is to investigate in detail the effect of using the AQFT in Shor's algorithm.

## 9.2 Dependence of output reliability on period of $f(k) = m^k \bmod N$

Different values of  $r$  (the period of  $f(k) = x^k \bmod N$ ) imply different probabilities  $s$  that the value  $j$  measured at the end of QPF will be useful. In particular, as discussed in Chapter 7, if  $r$  is a power of 2 the probability of useful output is much higher (Fig. 7.2). This section investigates how sensitive  $s$  is to variations in  $r$ . Recall Eq. (7.7) for the probability of measuring a given value of  $j$ . When the AQFT of Eq. (9.2) is used this becomes

$$\Pr(j, r, L, d_{\max}) = \left| \frac{\sqrt{r}}{2^{2L}} \sum_{p=0}^{2^{2L}/r-1} \exp\left(\frac{2\pi i}{2^{2L}} \tilde{\sum}_{mn} [j]_m [pr]_n 2^{m+n}\right) \right|^2 \quad (9.3)$$

The probability  $s$  of useful output is thus

$$s(r, L, d_{\max}) = \sum_{\{\text{useful } j\}} \Pr(j, r, L, d_{\max}) \quad (9.4)$$

where  $\{\text{useful } j\}$  denotes all  $j = \lfloor c2^{2L}/r \rfloor$  or  $\lceil c2^{2L}/r \rceil$  such that  $0 < c < r$ . Fig. 9.3 shows  $s$  for  $r$  ranging from 2 to  $2^L - 1$  and for various values of  $L$  and  $d_{\max}$ . The decrease in  $s$  for small values of  $r$  is more a result of the definition of  $\{\text{useful } j\}$  than an indication of poor data. When  $r$  is small there are few useful values of  $j \simeq c2^{2L}/r$ ,  $0 < c < r$  and a large range states likely to be observed around each one resulting superficially in a low probability of useful output  $s$  as  $s$  is the sum of the probabilities of observing only values  $j = \lfloor c2^{2L}/r \rfloor$  or  $\lceil c2^{2L}/r \rceil$ ,  $0 < c < r$ . However, in practice values much further from  $j \simeq c2^{2L}/r$  can be used to obtain useful output. For example if  $r = 4$  and  $j = 16400$  the correct output value (4) can still be determined from the continued fraction expansion of  $16400/65536$  which is far from the ideal case of  $16384/65536$ . To simplify subsequent analysis each pair  $(L, d_{\max})$  will from now on be associated with  $s(2^{L-1} + 2, L, d_{\max})$  which corresponds to the minimum value of  $s$  to the right of the central peak. The choice of this point as a meaningful characterization of the entire graph is justified by the discussion above.

For completeness, Fig. 9.3e shows the case of noisy controlled rotation gates of the form

$$\begin{pmatrix} 1 & 0 & 0 & 0 \\ 0 & 1 & 0 & 0 \\ 0 & 0 & 1 & 0 \\ 0 & 0 & 0 & e^{i(\pi/2^d + \delta)} \end{pmatrix}. \quad (9.5)$$

where  $\delta$  is a normally distributed random variable of standard deviation  $\sigma$ . This has been included to simulate the effect of using approximate rotation gates built out of a finite number of fault-tolerant gates. The general form and probability of successful output can be seen to be similar despite  $\sigma = \pi/32$ . This  $\sigma$  corresponds to  $\pi/2^{d_{\max}+2}$ . For a controlled  $\pi/64$  rotation,



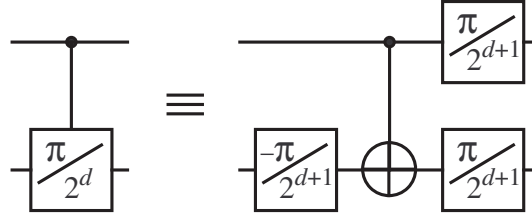


Fig. 9.2: Decomposition of a controlled phase gate into single-qubit rotations and a CNOT gate.

single-qubit rotations of angle  $\pi/128$  are required, as shown in Fig. 9.2.

Fig. 9.3e implies that it is acceptable for these rotations to be implemented within  $\pi/512$ , implying

$$U = \begin{pmatrix} 1 & 0 \\ 0 & e^{i(\pi/128 + \pi/512)} \end{pmatrix} \quad (9.6)$$

is an acceptable approximation of  $R_{128}$ . This point will be developed further in Chapter 9.

### 9.3 Dependence of output usefulness on integer length and rotation gate set

In order to determine how the probability of useful output  $s$  depends on both the integer length  $L$  and the minimum allowed controlled rotation  $\pi/2^{d_{\max}}$ , Eq. (9.4) was solved with  $r = 2^{L-1} + 2$  as discussed in Section 9.2. Fig. 9.4 contains semilog plots of  $s$  versus  $L$  for different values of  $d_{\max}$ . Note that Eq. (9.4) grows exponentially more difficult to evaluate as  $L$  increases.

For  $d_{\max}$  from 0 to 5, the exponential decrease of  $s$  with increasing  $L$  is

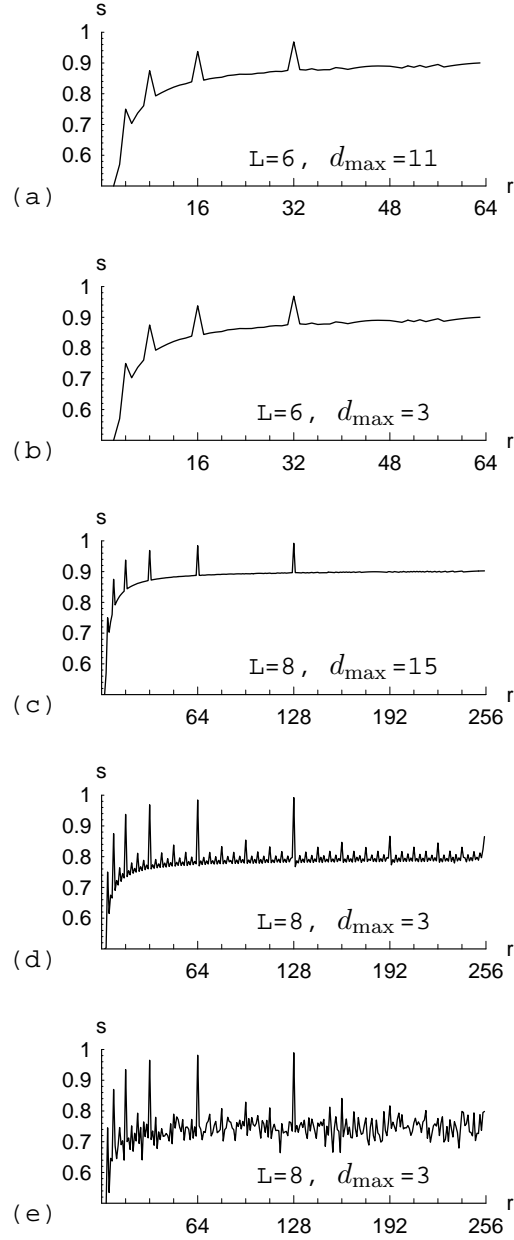


Fig. 9.3: Probability  $s$  of obtaining useful output from quantum period finding as a function of period  $r$  for different integer lengths  $L$  and rotation gate restrictions  $\pi/2^{d_{\max}}$ . The effect of using inaccurate controlled rotation gates ( $\sigma = \pi/32$ ) is shown in (e).

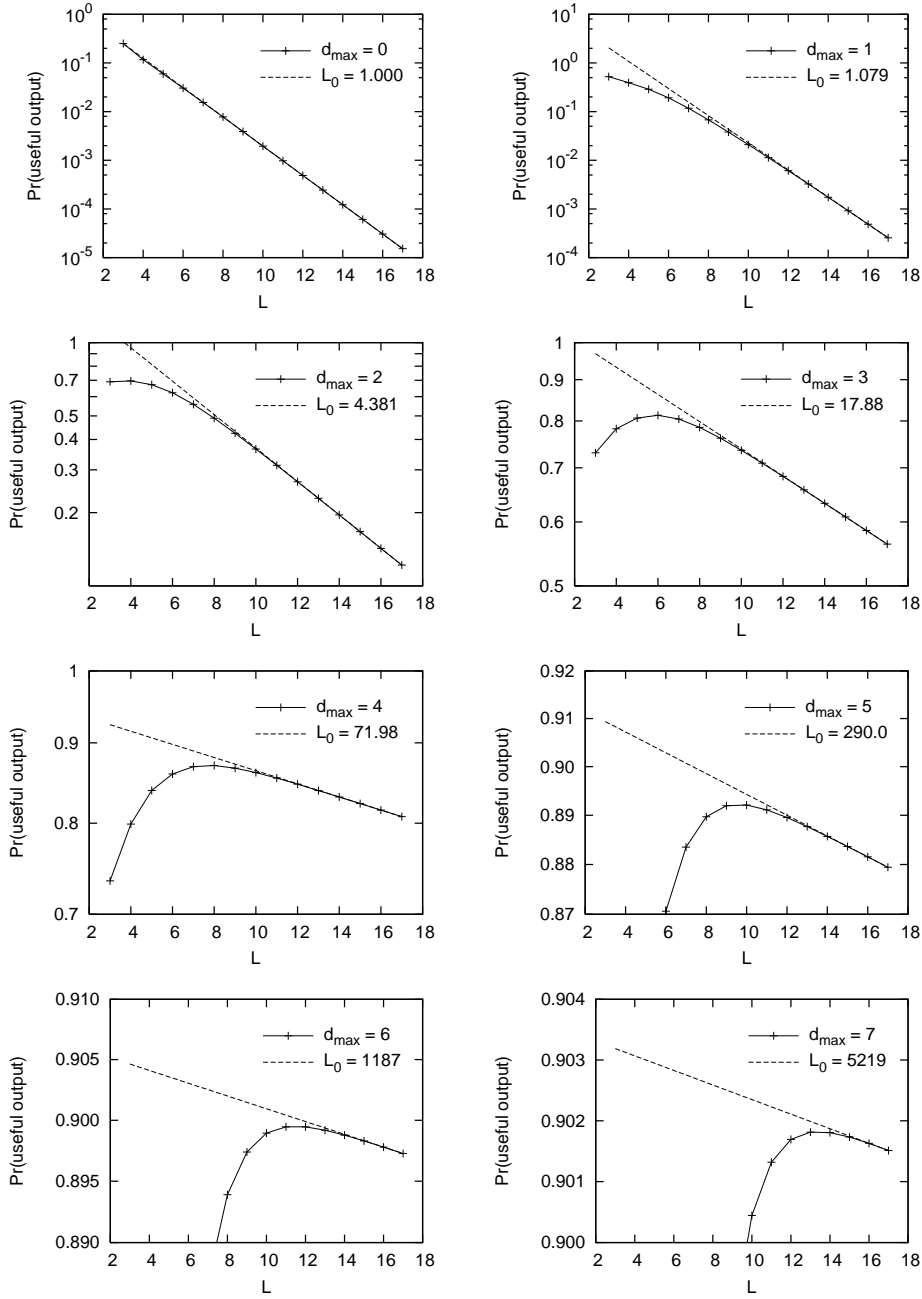


Fig. 9.4: Dependence of the probability of useful output from the quantum part of Shor's algorithm on the length  $L$  of the integer being factored for different levels of restriction of controlled rotation gates of angle  $\pi/2^{d_{\max}}$ . The parameter  $L_0$  characterizes lines of best fit of the form  $s \propto 2^{-L/L_0}$ .

clear. Asymptotic lines of best fit of the form

$$s \propto 2^{-L/L_0} \quad (9.7)$$

have been shown. Note that for  $d_{\max} > 0$ , the value of  $L_0$  increases by greater than a factor of 4 when  $d_{\max}$  increases by 1. This enables one to generalize Eq. (9.7) to an asymptotic lower bound valid for all  $d_{\max} > 0$

$$s \propto 2^{-L/4^{d_{\max}-1}} \quad (9.8)$$

with the constant of proportionality approximately equal to 1.

Keeping in mind that the required number of repetitions of QPF is  $O(1/s)$ , one can relate  $L_{\max}$  to  $d_{\max}$  by introducing an additional parameter  $f_{\max}$  characterizing the acceptable number of repetitions of QPF

$$L_{\max} \simeq 4^{d_{\max}-1} \log_2 f_{\max}. \quad (9.9)$$

Available RSA [7] encryption programs such as PGP typically use integers of length  $L$  up to 4096. The circuit in [186] runs in  $150L^3$  steps when an architecture that can interact arbitrary pairs of qubits in parallel is assumed and fault-tolerant gates are used. By virtue of the fact that this circuit only interacts a few qubits at a time leaving the rest idle, error correction can be easily built in without increasing the circuit depth. Thus for  $L = 4096$ ,  $\sim 10^{13}$  steps are required to perform a single run of QPF. On an electron spin or charge quantum computer [196, 99] running at 10GHz this corresponds to  $\sim 15$  minutes of computing. If we assume  $\sim 24$  hours of computing is acceptable then  $f_{\max} \sim 10^2$ . Substituting these values of  $L_{\max}$  and  $f_{\max}$  into Eq. (9.9) gives  $d_{\max} = 6$  after rounding up. Thus provided controlled  $\pi/64$

rotations can be implemented accurately, implying the need to accurately implement  $\pi/128$  single-qubit rotations, it is conceivable that a quantum computer could one day be used to break a 4096-bit RSA encryption in a single day. With additional qubits, this time could be reduced by several orders of magnitude by using one of the circuits described in Ref. [185].

#### 9.4 Conclusion

We have demonstrated the robustness of Shor's algorithm when a limited set of rotation gates is used. The length  $L_{\max}$  of the longest factorable integer can be related to the maximum acceptable runs of quantum period finding  $f_{\max}$  and the smallest accurately implementable controlled rotation gate  $\pi/2^{d_{\max}}$  via  $L_{\max} \sim 4^{d_{\max}-1} \log_2 f_{\max}$ . Integers thousands of digits in length can be factored provided controlled  $\pi/64$  rotations can be implemented with rotation angle accurate to  $\pi/256$ , corresponding to single-qubit  $\pi/128$  rotations implemented within  $\pi/512$ . Sufficiently accurate fault-tolerant approximations of such single-qubit rotation gates are presented in Chapter 10.



## 10. Constructing arbitrary single-qubit fault-tolerant gates

In large-scale quantum computation, every qubit of data is encoded across multiple physical qubits to form a logical qubit permitting quantum error correction and fault-tolerant computation. Unfortunately, only very small sets of fault-tolerant gates  $\mathcal{G}$  can be applied simply and exactly to logical qubits, where  $\mathcal{G}$  depends on the number of logical qubits considered, the code used, and the level of complexity one is prepared to tolerate when implementing fault-tolerant gates. Gates outside  $\mathcal{G}$  must be approximated with sequences of gates in  $\mathcal{G}$ . The existence of efficient approximating sequences has been established by the Solovay-Kitaev theorem and subsequent work [119, 120, 30, 121]. In this chapter, we describe a numerical procedure taking a universal gate set  $\mathcal{G}$ , gate  $U$ , and integer  $l$  and outputting an optimal approximation of  $U$  using at most  $l$  gates from  $\mathcal{G}$ . This procedure is used to explore the properties of approximations of the single-qubit phase rotation gates built out of fault-tolerant gates that can be applied to a single Steane code logical qubit. The average rate of convergence of Steane code fault-tolerant approximations to arbitrary single-qubit gates is also obtained.

Section 10.1 describes the basics of the numerical procedure used to find optimal gate sequences approximating a given gate. A universal set of 24 gates that can be applied fault-tolerantly to a single Steane code logical qubit

is given in Section 10.2, along with most of their quantum circuits. The complicated circuits comprising the T-gate, which is part of this universal set, are described separately in Section 10.3. Section 10.4 contains a discussion of single-qubit phase rotations and their fault-tolerant approximations, followed by approximations of arbitrary gates in Section 10.5. Section 10.6 summarizes the results of this chapter and their implications, and points to further work.

### 10.1 Finding optimal approximations

Let  $U(m)$  denote the  $m$ -dimensional unitary group. In this section, we outline a numerical procedure that takes a finite gate set  $\mathcal{G} \subset U(m)$  that generates  $U(m)$ , a gate  $U \in U(m)$ , and an integer  $l$  and outputs an optimal sequence  $U_l$  of at most  $l$  gates from  $\mathcal{G}$  minimizing the metric

$$\text{dist}(U, U_l) = \sqrt{\frac{m - |\text{tr}(U^\dagger U_l)|}{m}}. \quad (10.1)$$

The rationale of Eq. (10.1) is that if  $U$  and  $U_l$  are similar,  $U^\dagger U_l$  will be close to the identity matrix (possibly up to some global phase) and the absolute value of the trace will be close to  $m$ . By subtracting this absolute value from  $m$  and dividing by  $m$  a number between 0 and 1 is obtained. The overall square root is required to ensure that the triangle inequality

$$\text{dist}(U, W) \leq \text{dist}(U, V) + \text{dist}(V, W) \quad (10.2)$$

is satisfied. This metric has been used in preference to the trace distance used in the Solovay-Kitaev theorem [120, 30], as the trace distance does not ignore global phase, and hence leads to unnecessarily long phase correct approximating sequences.



Finding optimal gate sequences is a difficult task, and the run-time of the numerical procedure presented here scales exponentially with  $l$ . Nevertheless, as we shall see in Section 10.4, gate sequences of sufficient length for practical purposes can be obtained.

For a set  $\mathcal{G}$  of size  $g = |\mathcal{G}|$  and a maximum sequence length of  $l$ , the size of the set of all possible gate sequences of length up to  $l$  is approximately  $g^l$ . For even moderate  $g$  and  $l$ , this set cannot be searched exhaustively. To describe the basics of the actual method used, a few more definitions are required. Let  $G$  denote a gate in  $\mathcal{G}$ . Order  $\mathcal{G}$ , and denote the  $i$ th gate by  $G_i$ . Let  $S$  denote a sequence of gates in  $\mathcal{G}$ . Order the possible gate sequences in the obvious manner  $G_1, \dots, G_g, G_1G_1, \dots, G_1G_g, G_2G_1, \dots$ , and let  $S_n$  denote the  $n$ th sequence in this ordering. Let  $\{S\}_l$  denote all sequences with length less than or equal to  $l$ . Let  $\{Q\}_{l'}, l' < l$  denote the set of unique sequences of length at most  $l'$ . Naively,  $\{Q\}_{l'}$  can be constructed by starting with the set containing the identity matrix, sequentially testing whether  $S_n \in \{S\}_{l'}$  satisfies  $\text{dist}(S_n, Q) > 0$  for all  $Q \in \{Q\}_{l'}$ , and adding  $S_n$  to  $\{Q\}_{l'}$  if it does. A search for an optimal approximation of  $U$  using gates in  $\mathcal{G}$  begins with the construction of a very large set of unique sequences  $\{Q\}_{l'}$ .

The utility of  $\{Q\}_{l'}$  lies in its ability to predict which sequences in  $\{S\}_l, l > l'$  do not need to be compared with  $U$  to determine whether they are good approximations, and what the next sequence worth comparing is. To be more precise, assume every sequence up to  $S_{n-1}$  has been compared with  $U$ . Let  $\{S_{n-1}\}$  denote this set of compared sequences. Consider subsequences of  $S_n$  of length  $l'$ . If any subsequence is not in  $\{Q\}_{l'}$ , there exists a sequence in  $\{S_{n-1}\}$  equivalent to  $S_n$ . In other words, a sequence equivalent to  $S_n$  has already been compared with  $U$ , and  $S_n$  can be skipped.

Furthermore, let

$$S_n = G_{i_N} \dots G_{i_{k+l'+1}} G_{i_{k+l'}} \dots G_{i_{k+1}} G_{i_k} \dots G_{i_1}, \quad (10.3)$$

where  $G_{i_{k+l'}} \dots G_{i_{k+1}}$  is the subsequence not in  $\{Q\}_{l'}$ . Let  $Q(G_{i_{k+l'}} \dots G_{i_{k+1}})$  denote the next sequence in  $\{Q\}_{l'}$  after  $G_{i_{k+l'}} \dots G_{i_{k+1}}$ . The next sequence with the potential to not be equivalent to a sequence in  $\{S_{n-1}\}$  is

$$G_{i_N} \dots G_{i_{k+l'+1}} Q(G_{i_{k+l'}} \dots G_{i_{k+1}}) G_1 \dots G_1. \quad (10.4)$$

The process of checking subsequences is then repeated on this new sequence. Skipping sequences in this manner is vastly better than an exhaustive search, and enables optimal sequences of interesting length to be obtained. It should be stressed, however, that the runtime is still exponentially in  $l$ .

Highly non-optimal but polynomial runtime sequence finding techniques do exist [120, 30, 197, 198] but will not be discussed here.

## 10.2 Simple Steane code single-qubit gates

For the remainder of the chapter we will restrict our attention to fault-tolerant single-qubit gates that can be applied to the 7-qubit Steane code.

The Steane code representation of states  $|0\rangle$  and  $|1\rangle$  is [113]

$$\begin{aligned} |0_L\rangle = & \frac{1}{\sqrt{8}}(|0000000\rangle + |1010101\rangle + |0110011\rangle + |1100110\rangle \\ & + |0001111\rangle + |1011010\rangle + |0111100\rangle + |1101001\rangle), \end{aligned} \quad (10.5)$$

$$\begin{aligned} |1_L\rangle = & \frac{1}{\sqrt{8}}(|1111111\rangle + |0101010\rangle + |1001100\rangle + |0011001\rangle \\ & + |1110000\rangle + |0100101\rangle + |1000011\rangle + |0010110\rangle). \end{aligned} \quad (10.6)$$

An equivalent description of this code can be given in terms of stabilizers [117] which are operators that map the logical states  $|0_L\rangle$  and  $|1_L\rangle$  to themselves.

$$\text{IIIXXXX} \quad (10.7)$$

$$\text{IXXIIXX} \quad (10.8)$$

$$\text{XIXIXIX} \quad (10.9)$$

$$\text{IIIZZZZ} \quad (10.10)$$

$$\text{IZZIIZZ} \quad (10.11)$$

$$\text{ZIZIZIZ} \quad (10.12)$$

States  $|0_L\rangle$  and  $|1_L\rangle$  are the only two that are simultaneously stabilized by Eqs (10.7–10.12). Non-fault-tolerant circuits for both a general and LNN architecture that take an arbitrary state  $\alpha|0\rangle + \beta|1\rangle$  and produce  $\alpha|0_L\rangle + \beta|1_L\rangle$  are shown in Fig. 10.1. The fault-tolerant preparation of logical states is more complicated, and will be discussed in the context of  $T$ -gate ancilla state preparation in Section 10.3.

The minimal universal set of single-qubit fault-tolerant gates that can be applied to a Steane code logical qubit consists of just the Hadamard gate and the  $T$ -gate

$$T = \begin{pmatrix} 1 & 0 \\ 0 & e^{i\pi/4} \end{pmatrix}. \quad (10.13)$$

For practical purposes, the gates  $X$ ,  $Z$ ,  $S$ ,  $S^\dagger$  should be added to this set, where

$$S = \begin{pmatrix} 1 & 0 \\ 0 & i \end{pmatrix}, \quad (10.14)$$

along with all gates generated by  $H$ ,  $X$ ,  $Z$ ,  $S$ ,  $S^\dagger$ . The complete list of

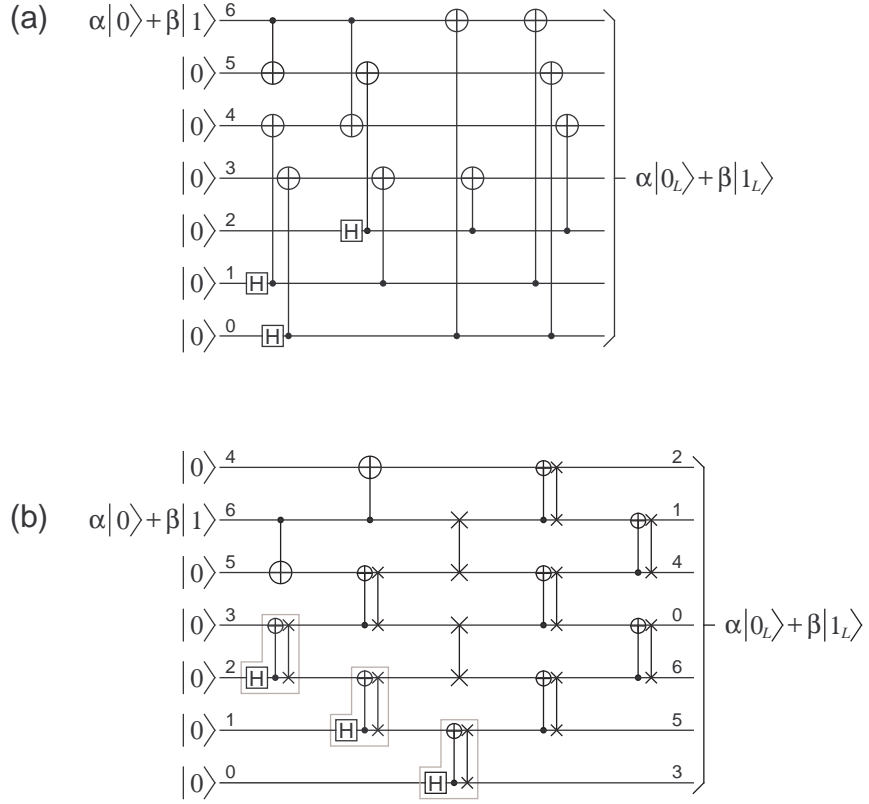


Fig. 10.1: Non-fault-tolerant 7-qubit Steane code encoding circuits taking an arbitrary state  $\alpha|0\rangle + \beta|1\rangle$  and producing  $\alpha|0_L\rangle + \beta|1_L\rangle$ . (a) Depth 4 circuit for an architecture able to interact arbitrary pairs of qubits. (b) Depth 5 circuit for a linear nearest neighbor architecture.

gates that we shall consider is shown in Eq. (10.15). This is our set  $\mathcal{G}$ . Note that gates  $\{I, G_1, \dots, G_{23}\}$  form a group under multiplication. Appendix A contains the multiplication table of this group.

$$\begin{array}{ll}
G_1 = H & G_{13} = HS \\
G_2 = X & G_{14} = HS^\dagger \\
G_3 = Z & G_{15} = ZXH \\
G_4 = S & G_{16} = SXH \\
G_5 = S^\dagger & G_{17} = S^\dagger XH \\
G_6 = XH & G_{18} = HSH \\
G_7 = ZH & G_{19} = HS^\dagger H \\
G_8 = SH & G_{20} = HSX \\
G_9 = S^\dagger H & G_{21} = HS^\dagger X \\
G_{10} = ZX & G_{22} = S^\dagger HS \\
G_{11} = SX & G_{23} = SHS^\dagger \\
G_{12} = S^\dagger X & G_{24} = T
\end{array} \tag{10.15}$$

To justify the use of such a large set  $\mathcal{G}$ , consider the transversal circuits shown in Fig. 10.2 implementing  $H$ ,  $X$ ,  $Z$ ,  $S$  and  $S^\dagger$ . By combination, it can be seen that gates  $\{G_6, \dots, G_{23}\}$  can also be implemented with simple transversal applications of single qubit gates. As we shall see in Section 10.3, by comparison the  $T$ -gate is extremely complicated to implement. Since we are interested in minimal complexity as well as minimum length sequences of gates in  $\mathcal{G}$ , it would be unreasonable to count  $G_{23}$  as three gates when in reality it can be implemented as easily as any other gate  $\{G_1, \dots, G_{22}\}$ . Since  $\{I, G_1, \dots, G_{23}\}$  is a group under multiplication, minimum length sequences of gates approximating some  $U$  outside  $\mathcal{G}$  will alternate between an element of  $\{G_1, \dots, G_{23}\}$  and a  $T$ -gate. Note that the  $T^\dagger$ -gate is not required in  $\mathcal{G}$  for

universality or efficiency as, in gate sequences of length  $l \geq 2$ , it is equally efficient to use  $S^\dagger T$  or  $TS^\dagger$ . The extra  $S^\dagger$ -gate is absorbed into neighboring  $G_i$ -gates,  $i < 24$ .

### 10.3 The fault-tolerant $T$ -gate

Moving on to implementing the fault-tolerant  $T$ -gate [30], the basic idea is to prepare an ancilla state  $|0_L\rangle + e^{i\pi/4}|1_L\rangle$  then apply the circuit shown in Fig. 10.3. Tracing the action of Fig. 10.3, we initially have

$$(|0_L\rangle + e^{i\pi/4}|1_L\rangle)(\alpha|0_L\rangle + \beta|1_L\rangle). \quad (10.16)$$

After applying the CNOT we obtain

$$\begin{aligned} & \alpha|0_L\rangle|0_L\rangle + \beta|0_L\rangle|1_L\rangle + \alpha e^{i\pi/4}|1_L\rangle|1_L\rangle + \beta e^{i\pi/4}|1_L\rangle|0_L\rangle \\ = & (\alpha|0_L\rangle + \beta e^{i\pi/4}|1_L\rangle)|0_L\rangle + (\beta|0_L\rangle + \alpha e^{i\pi/4}|1_L\rangle)|1_L\rangle. \end{aligned} \quad (10.17)$$

After measuring the lower logical qubit, if  $|0_L\rangle$  is observed (meaning one of the eight bit strings shown in Eq. (10.5) or a bit string a single bit different from one of these eight), no further action is required. If  $|1_L\rangle$  is observed, applying the logical gate  $SX$  to the top qubit will yield the desired state up to an irrelevant global phase. Note that the measurement step and subsequent classical processing allows the correction of a single bit-flip error and is insensitive to phase errors.

To fault-tolerantly prepare the ancilla state, we first need to be able to fault-tolerantly prepare the state  $|0_L\rangle$ . As we shall see, to do this, we need to be able to fault-tolerantly determine whether a state  $|\Psi\rangle$  is in the  $+1$  or  $-1$  eigenstate of a self-inverse operator  $A$  ( $A^2 = I$ ). A non-fault-tolerant circuit doing this is shown in Fig. 10.4. It is instructive to trace the action of the

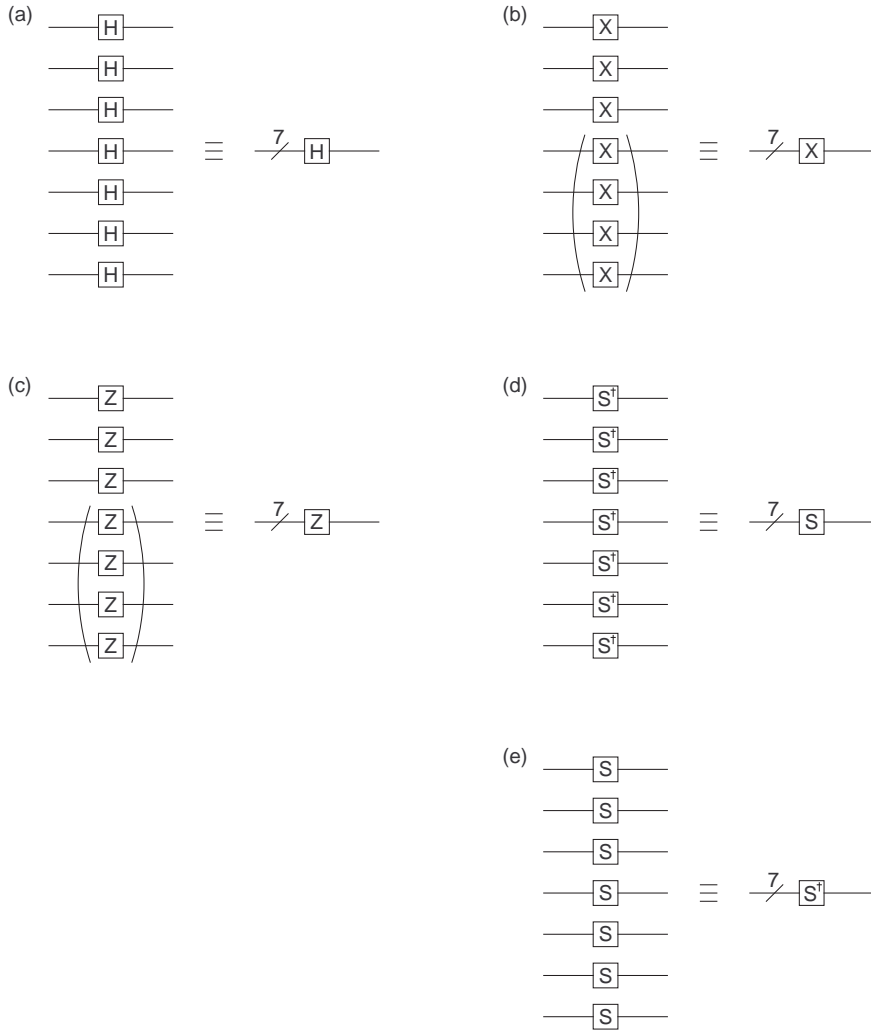


Fig. 10.2: Circuits fault-tolerantly applying common single-qubit gates to Steane code logical qubits. Gates in brackets are optional as they implement stabilizers.

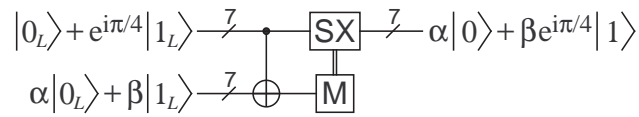


Fig. 10.3: High-level representation of the circuit implementing the  $T$ -gate on a Steane code logical qubit. Input  $\alpha|0_L\rangle + \beta|1_L\rangle$  is transformed into  $\alpha|0_L\rangle + \beta e^{i\pi/4}|1_L\rangle$ .

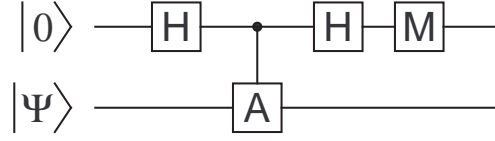


Fig. 10.4: Circuit measuring whether  $|\Psi\rangle$  is in the  $+1$  or  $-1$  eigenstate of  $A$ .

circuit. The initial state is  $|0\rangle|\Psi\rangle$ , which after the first Hadamard becomes  $(|0\rangle + |1\rangle)|\Psi\rangle$ . After the controlled- $A$  the state becomes  $|0\rangle|\Psi\rangle + |1\rangle A|\Psi\rangle$ . After the second Hadamard

$$\begin{aligned}
 & (|0\rangle + |1\rangle)|\Psi\rangle + (|0\rangle - |1\rangle)A|\Psi\rangle \\
 = & |0\rangle(|\Psi\rangle + A|\Psi\rangle) + |1\rangle(|\Psi\rangle - A|\Psi\rangle).
 \end{aligned} \tag{10.18}$$

If a zero is measured, the lower qubit will be in the  $+1$  eigenstate  $|\Psi\rangle + A|\Psi\rangle$ . Conversely, if one is measured, the lower qubit will be in the  $-1$  eigenstate  $|\Psi\rangle - A|\Psi\rangle$ .

The specific self-inverse operators we wish to measure are the stabilizers Eqs (10.7–10.9). To build a fault-tolerant circuit measuring these multiple qubit operators, the control qubit shown in Fig. 10.4 must be replaced by a cat state so that each qubit modified by the stabilizer is controlled by a different qubit in the cat state. This is necessary to prevent a single error in a control qubit propagating to multiple target qubits. This in turn necessitates fault-tolerant cat state preparation which is shown in Fig. 10.5a [199]. A single bit- or phase-flip anywhere in this circuit causes at most one error in the final state. This circuit is significantly simpler, and no less robust than the fault-tolerant cat state preparation circuit suggested in [30] (Fig. 10.6). The uncat circuit of Fig. 10.5b is fault-tolerant purely because its output is a single qubit and by definition a single error can cause of most



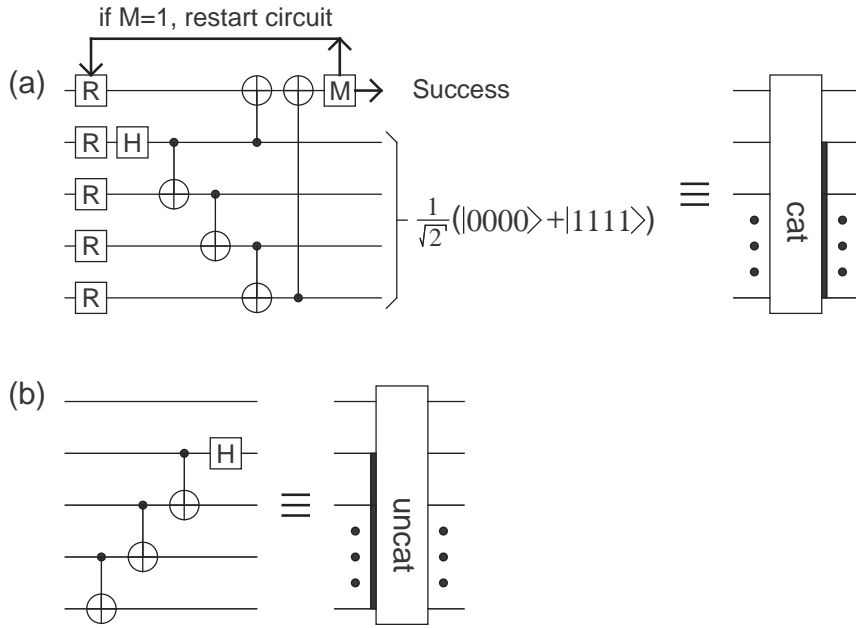


Fig. 10.5: (a) Simple circuit fault-tolerantly preparing a cat state. (b) Circuit undoing the preparation of a cat state.

one error in the output.

Using the circuit notation shown in Fig. 10.7, the complete circuit for fault-tolerantly measuring a stabilizer is shown in Fig. 10.8. Note that the basic stabilizer measurement circuit appears three times since a single error in a cat state block, while not propagating to multiple qubits in the logical state block, almost always causes an incorrect measurement. To ensure a probability  $O(p^2)$  of incorrect measurement, the process must be repeated up to three times. The third measurement structure can be omitted if the first two measurements are the same. The final triply controlled Z-gate is only applied if the majority of the measurements are one. Note that this assumes fast and reliable classical processing is available. The final Z-gate converts a  $-1$  eigenstate of  $XIXIXIX$  into a  $+1$  eigenstate. Thus the

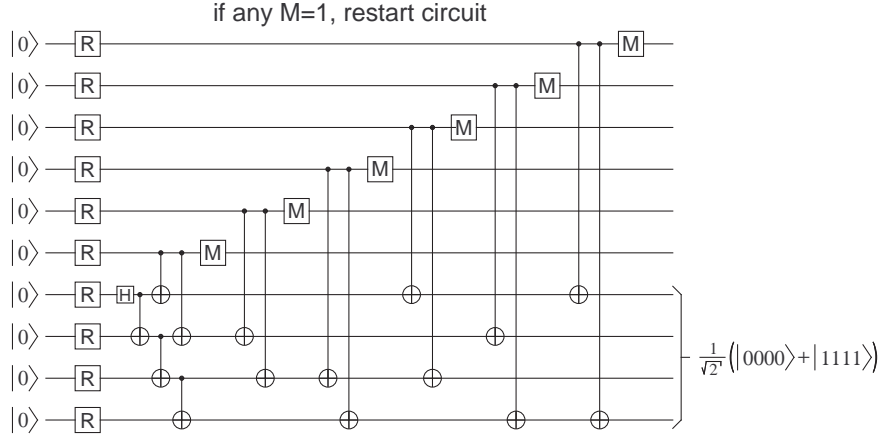


Fig. 10.6: Typical, but unnecessarily complicated circuit fault-tolerantly preparing a cat state.

output of Fig. 10.8 is the  $+1$  eigenstate of  $XIXIXIX$  with probability  $O(p^2)$  of failure (i.e. more than one incorrect output qubit).

We now have the necessary tools to fault-tolerantly prepare  $|0_L\rangle$ . Recall that  $|0_L\rangle$  and  $|1_L\rangle$  are the only two states simultaneously stabilized by all of Eqs (10.7–10.12). If we include the logical  $Z$  operator,  $|0_L\rangle$  is the unique state stabilized by  $Z$  and all six stabilizers. The state  $|0_L\rangle$  could thus be created using the circuit of Fig. 10.9 which outputs  $|0_L\rangle$  for arbitrary input [30].

A better way of obtaining  $|0_L\rangle$ , is to start with the state  $|0000000\rangle$  which is physically accessible in a quantum computer architecture either via some form of special reset operation, or measurement possibly followed by an  $X$ -gate. State  $|0000000\rangle$  is a  $+1$  eigenstate of logical  $Z$  and Eqs (10.10–10.12), therefore only stabilizers Eqs (10.7–10.9) need to be measured (Fig. 10.10).

To complete the construction of the ancilla state, and hence the  $T$ -gate (Fig. 10.11), the operator  $e^{i\pi/4}X$  is measured. Note that  $e^{i\pi/4}X$  is not self-inverse, but nevertheless the circuit works as required. Specifically, be-

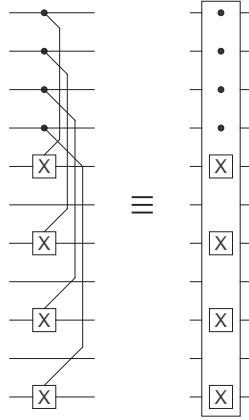


Fig. 10.7: Symbolic representation of transversal controlled operations.

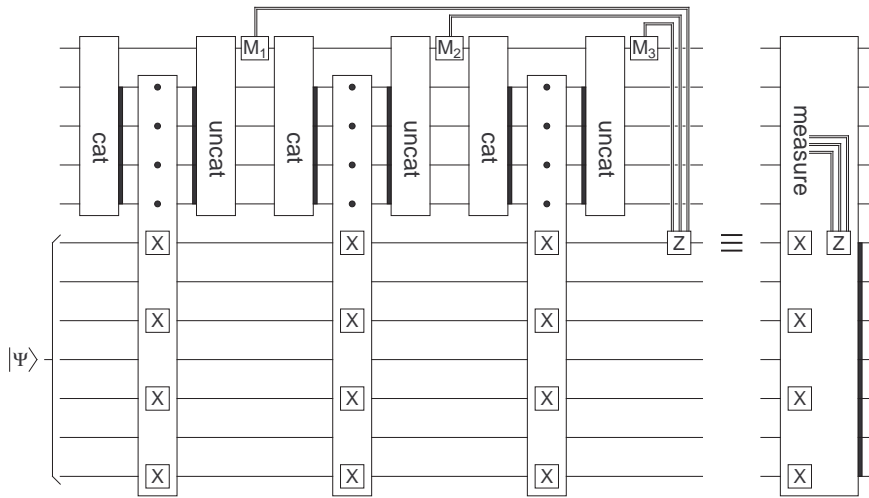


Fig. 10.8: Circuit fault-tolerantly projecting  $|\Psi\rangle$  onto the  $\pm 1$  eigenstates of XIXIXIX, then converting  $-1$  eigenstate's into  $+1$  eigenstates. The third measurement structure can be omitted if  $M_1 = M_2$ .

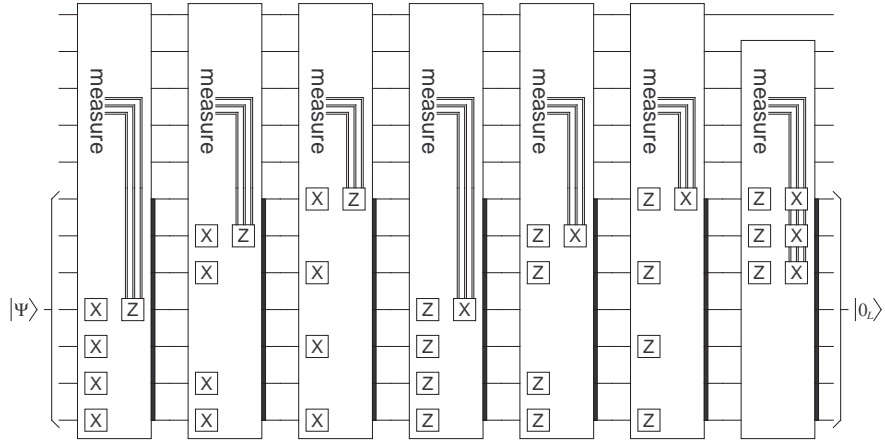


Fig. 10.9: Circuit taking arbitrary input and producing  $|0_L\rangle$  by repeated stabilizer measurement.

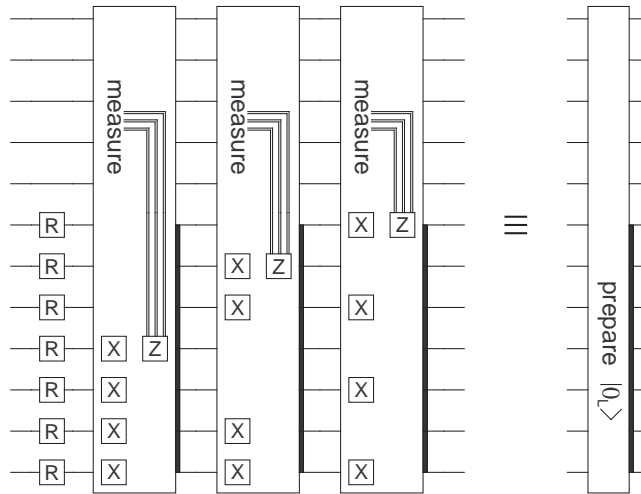


Fig. 10.10: Circuit taking arbitrary input and producing  $|0_L\rangle$  via physical resetting and just three stabilizer measurements.

fore cat state preparation we have  $|000\rangle|0_L\rangle$ . After cat state creation this becomes

$$\frac{1}{\sqrt{2}}(|000\rangle + |111\rangle)|0_L\rangle. \quad (10.19)$$

After transversal CNOT we have

$$\frac{1}{\sqrt{2}}(|000\rangle|0_L\rangle + |111\rangle|1_L\rangle). \quad (10.20)$$

Note that only three physical CNOT gates are required to implement a logical CNOT gate on the Steane code due to its stabilizer structure. After the single-qubit  $T$ -gate we have

$$\frac{1}{\sqrt{2}}(|000\rangle|0_L\rangle + e^{i\pi/4}|111\rangle|1_L\rangle). \quad (10.21)$$

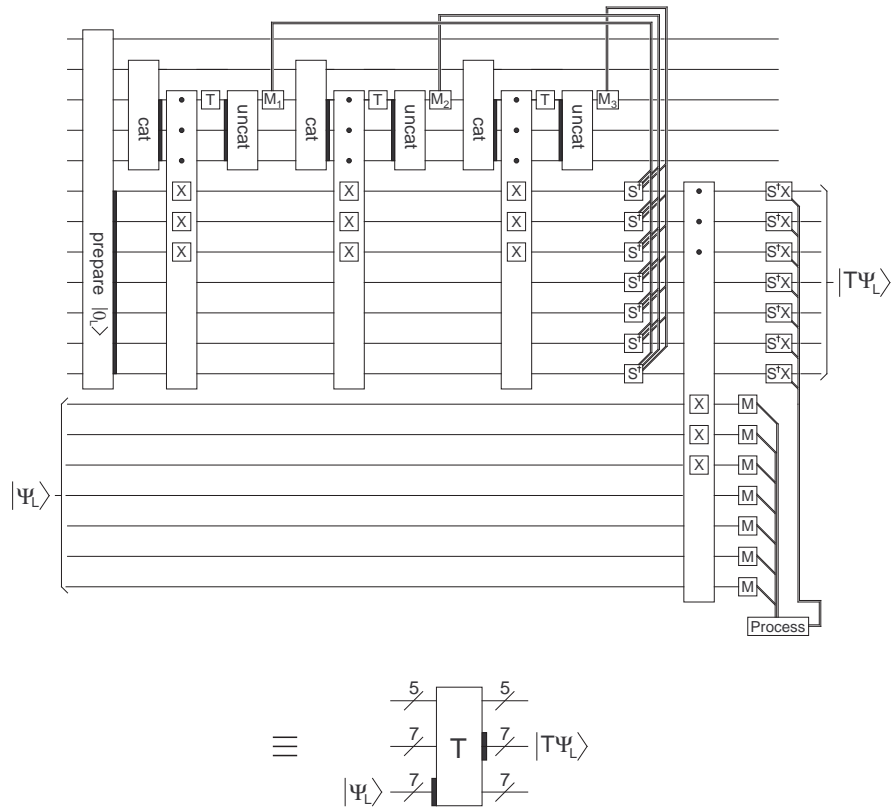
After uncat we have

$$|0\rangle \frac{1}{\sqrt{2}}(|0_L\rangle + e^{i\pi/4}|1_L\rangle) + |1\rangle \frac{1}{\sqrt{2}}(|0_L\rangle - e^{i\pi/4}|1_L\rangle), \quad (10.22)$$

resulting in the state  $(|0_L\rangle + e^{i\pi/4}|1_L\rangle)/\sqrt{2}$  if zero is measured, and  $(|0_L\rangle - e^{i\pi/4}|1_L\rangle)/\sqrt{2}$  if one is measured. Note that the steps shown in Eqs (10.19–10.22) must be repeated up to three times to be able to say that a 0 or 1 has been measured with probability of error  $O(p^2)$ . The final logical  $S$ -gate converts  $(|0_L\rangle - e^{i\pi/4}|1_L\rangle)/\sqrt{2}$  into  $(|0_L\rangle + e^{i\pi/4}|1_L\rangle)/\sqrt{2}$ . Under the assumptions that 2-qubit gates, measurement, reset and classical processing each have depth 1, single-qubit gates have depth zero and do not contribute to the gate count, and arbitrary disjoint 2-qubit gates can be implemented in parallel, Table 10.1 summarizes the best case complexity of the  $T$ -gate.

Circuit Element	Count
Qubits	19
Gates	93
Resets	45
Measurements	17
Depth	92

Tab. 10.1: Best case complexity of the T-gate.

Fig. 10.11: Complete circuit implementing the  $T$ -gate on a Steane code logical qubit.

## 10.4 Approximations of phase gates

We now use the machinery described in this chapter to construct optimal fault-tolerant approximations of single-qubit phase rotation gates

$$R_{2^d} = \begin{pmatrix} 1 & 0 \\ 0 & e^{i\pi/2^d} \end{pmatrix}. \quad (10.23)$$

Gates  $R_{2^d}$  are examples of gates used in the single-qubit quantum Fourier transform that forms part of the Shor circuits described in Chapters 8–9. Note that phase rotations of angle  $2\pi x/2^d$ , where  $x$  is a  $d$ -digit binary number, are also required, but the properties of fault-tolerant approximations of such gates can be inferred from  $R_{2^d}$ .

For a given  $R_{2^d}$ , and maximum number of gates  $l$  in  $\mathcal{G}$ , Fig. 10.12 shows  $\text{dist}(R_{2^d}, U_l)$  where  $U_l$  is an optimal sequence of at most  $l$  gates in  $\mathcal{G}$  minimizing  $\text{dist}(R_{2^d}, U_l)$ . For  $d \geq 3$ ,  $U_1$  is equivalent to the identity. Note that as  $d$  increases,  $R_{2^d}$  becomes closer and closer to the identity, lowering the value of  $\text{dist}(R_{2^d}, U_1)$ , and increasing the value of  $l$  required to obtain an approximation  $U_l$  that is closer to  $R_{2^d}$  than the identity. In fact, for  $R_{128}$  the shortest sequence of gates that provides a better approximation of  $R_{128}$  than the identity has length  $l = 31$ . There are a very large number of optimal sequences of this length. An example of one with a minimal number of  $T$ -gates is

$$\begin{aligned} U_{31} = & HTHT(SH)T(SH)T(SH)THTHT(SH) \\ & THTHT(SH)THTHTHT(SH)T(S^\dagger H) \end{aligned} \quad (10.24)$$

The parentheses group standard gates into elements of the set  $\mathcal{G}$  defined in Eq. (10.15). Note that  $\text{dist}(R_{128}, I) = 8.7 \times 10^{-3}$  whereas  $\text{dist}(R_{128}, U_{33}) =$

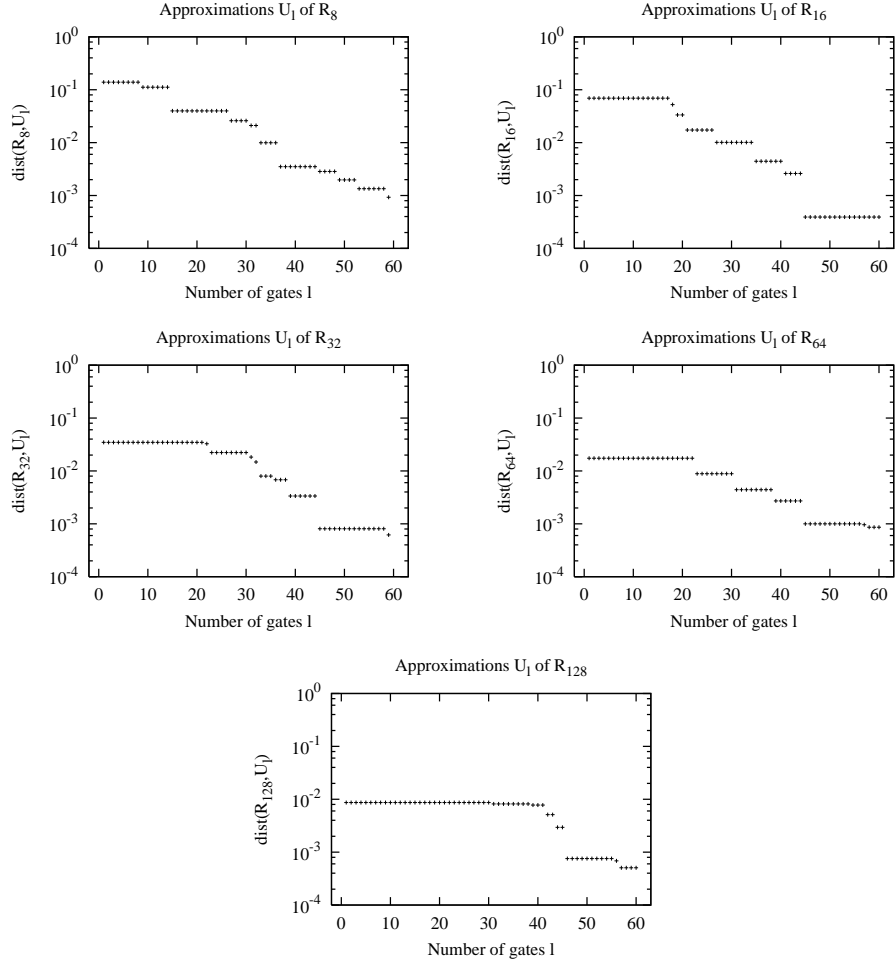


Fig. 10.12: Optimal fault-tolerant approximations  $U_l$  of phase rotation gates  $R_{2^d}$ , for  $R_8$  to  $R_{128}$ .

$8.1 \times 10^{-3}$ . In other words Eq. (10.24) is only slightly better than the identity. This immediately raises the question of how many gates are required to construct a sufficiently good approximation.

In Chapter 9, it was shown that

$$U = \begin{pmatrix} 1 & 0 \\ 0 & e^{i(\pi/128 + \pi/512)} \end{pmatrix} \quad (10.25)$$



was sufficiently close to  $R_{128}$ . This is, of course, only a property of Shor's algorithm, not a universal property of quantum circuits. Given  $\text{dist}(R_{128}, U) = 2.2 \times 10^{-3}$ , a sufficiently accurate fault-tolerant approximation  $U_l$  of  $R_{128}$  must therefore satisfy  $\text{dist}(R_{128}, U_l) < 2.2 \times 10^{-3}$ . The smallest value of  $l$  for which this is true is 46, and one of the many optimal gate sequences satisfying  $\text{dist}(R_{128}, U_{46}) = 7.5 \times 10^{-4}$  is

$$\begin{aligned} U_{46} = & HTHTHT(SH)THT(SH)T(SH)T(SH)THT \\ & (SH)T(SH)THTHT(SH)T(SH)THT(SH)T \\ & (SH)T(SH)THT(SH)THT(HS^\dagger)T \end{aligned} \quad (10.26)$$

Parentheses again group standard gates into elements of  $\mathcal{G}$ . Now that we have a minimal complexity circuit sufficiently close to  $R_{128}$ , the immediate question is whether it is practical. An alternative to Eq. (10.26) is shown in Fig. 10.13 which simply decodes the logical qubit, applies  $R_{128}$ , then re-encodes. This simple non-fault-tolerant circuit will fail (generate more than one error in the output logical qubit) if a single error occurs almost anywhere in the top six qubits. Given there are  $11 \times 6 = 66$  possible error locations, the probability of no errors in the top six qubits is  $(1 - p)^{66}$ . This is the worst-case reliability of the circuit.

A partial schematic of the circuit corresponding to Eq. 10.26 is shown in Fig. 10.14. As the circuit is fault-tolerant, it only fails if at least two errors occur within the circuit. Any analysis of the reliability of the circuit is complicated by the fact that the  $T$ -gates that comprise the bulk of the circuit have error correction built in at a number of places. Furthermore, when errors are detected and corrected, the circuit typically increases in depth. Referring back to Fig. 10.11, we shall assume that the  $T$ -gate is only sensitive to errors in the lower 14 qubits and that the depth of the circuit

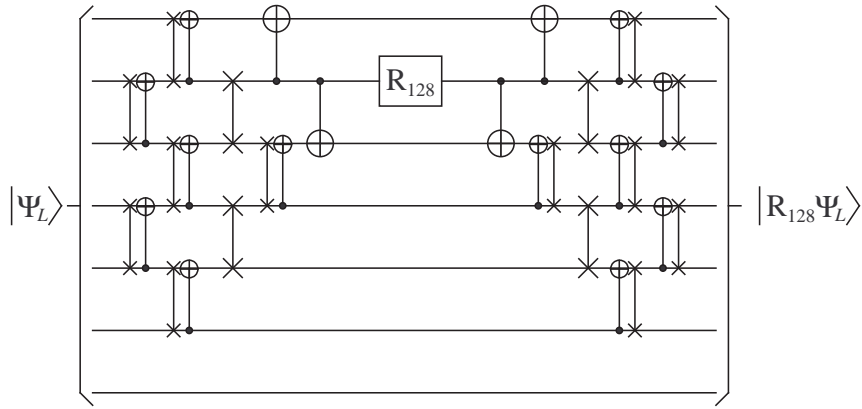


Fig. 10.13: Non-fault-tolerant circuit exactly implementing  $R_{128}$  by first decoding the logical qubit and re-encoding after application of  $R_{128}$ .

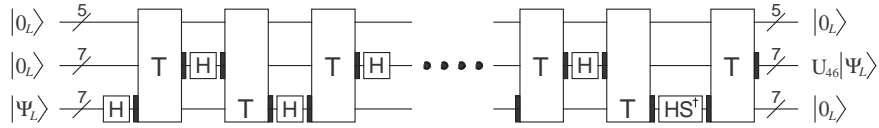


Fig. 10.14: Schematic of a minimum complexity, sufficiently accurate fault-tolerant approximation of  $R_{128}$  given in full by Eq. (10.26).

is never increased by errors. From Table 10.1, the best case depth of the  $T$ -gate is 92. This implies an area sensitive to errors of approximately 1300. Given there are 23  $T$ -gates in Fig. 10.14, the total area sensitive to errors is approximately 30000. The reliability of Fig. 10.14 is thus approximately  $(1 - p)^{30000} + 30000p(1 - p)^{29999}$ , which is only greater than the non-fault-tolerant circuit for  $p < 1.4 \times 10^{-7}$ .

A fault-tolerant circuit correcting an arbitrary single error in a Steane logical qubit is shown in Fig. 10.15. Consider the first half of the circuit. Given eigenvalue measurements  $E_1, E_2, E_3$ , the appropriate qubit to correct is shown in Table 10.2. Note that slightly less complex circuits exist that use

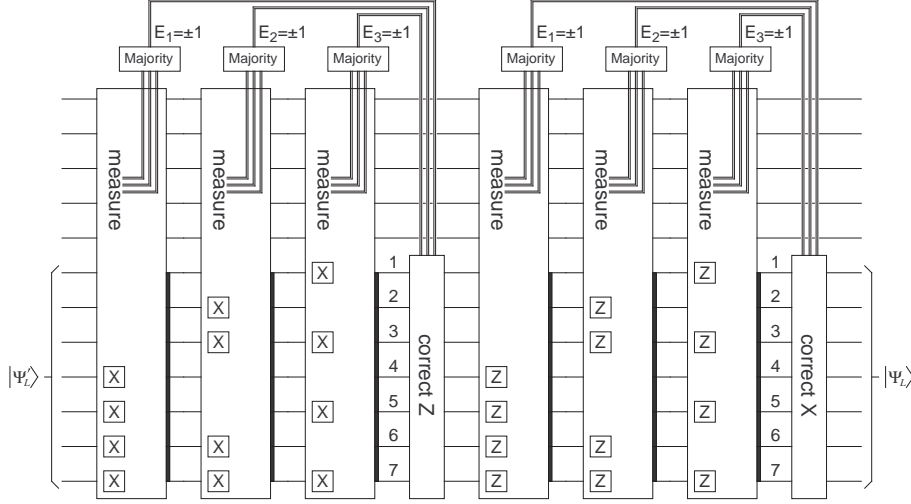


Fig. 10.15: Circuit fault-tolerantly correcting an arbitrary single error within the logical qubit. The qubit acted on by the correct  $Z/X$  boxes is described by Table 10.2.

more qubits [126], but our choice of circuit will not play a significant role in the following analysis. By applying error correction to the logical qubit after each  $T$ -gate in Fig. 10.14, the reliability of the circuit can be increased. The best case depth of Fig. 10.15 is 120, and if we assume that the circuit is only sensitive to errors in the lower seven qubits, the total area sensitive to errors is approximately 800. The error corrected  $U_{46}$  circuit will only fail if two errors occur within a single  $T$ -gate and error correction block. The reliability of a single block is  $(1 - p)^{2100} + 2100p(1 - p)^{2099}$ . The failure probability of the non-fault-tolerant circuit, the fault-tolerant circuit without correction, with correction after every second  $T$ -gate, and with correction after every  $T$ -gate is compared in Fig. 10.16.

Of the fault-tolerant circuits, the one with error correction after every  $T$ -gate performs best. Nevertheless, this circuit is still only more reliable than the non-fault-tolerant circuit for  $p < 1.3 \times 10^{-6}$ . Given that  $p \sim 10^{-6}$  is likely to be very difficult to achieve in practice, longer error correction

$E_1$	$E_2$	$E_3$	Qubit
+1	+1	+1	no error
+1	+1	-1	1
+1	-1	+1	2
+1	-1	-1	3
-1	+1	+1	4
-1	+1	-1	5
-1	-1	+1	6
-1	-1	-1	7

Tab. 10.2: Qubit to correct given certain sequence of eigenvalue measurements in both halves of Fig. 10.15.

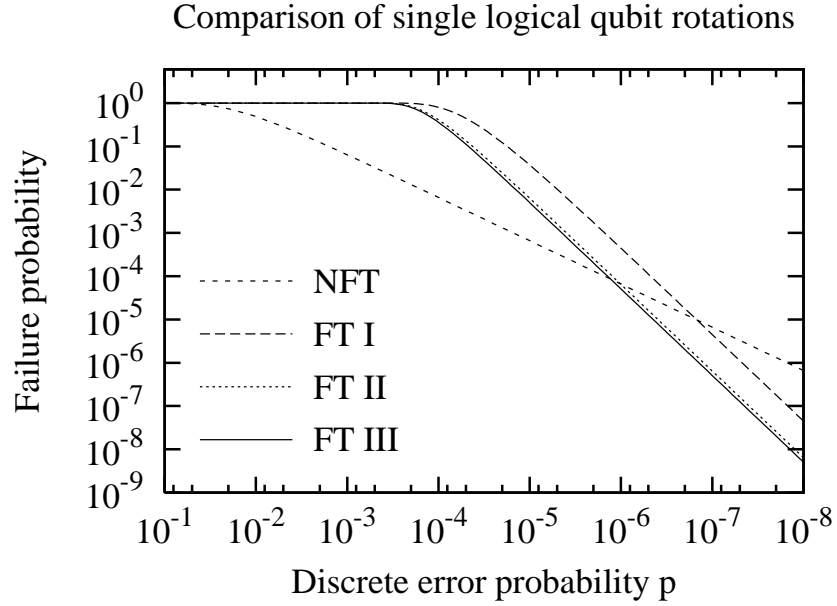


Fig. 10.16: Approximate probability of more than one error in the output logical qubit versus probability per qubit per time step of discrete error for different circuits implementing a  $R_{128}$  phase rotation gate. (a) NFT: non-fault-tolerant circuit from Fig. 10.13, (b) FT I: fault-tolerant circuit from Fig. 10.14, (c) FT II: as above but with Fig. 10.15 error correction after every second T-gate, (d) FT III: as above but with error correction after every T-gate. Note that all fault-tolerant results are for the 7-qubit Steane code without concatenation.

code words or concatenation would be required to make the fault-tolerant circuit practical [127]. Given that Fig. 10.14 is both extremely complex and the simplest fault-tolerant circuit sufficiently close to  $R_{128}$ , for practical computation non-fault-tolerant circuits similar to Fig. 10.13 are likely to remain the best way to implement arbitrary rotations for the foreseeable future.

In Shor's algorithm, the use of non-fault-tolerant rotations would be acceptable as only  $2L$  such gates are used to factorize an  $L$ -bit number  $N$ . Furthermore, only half of Fig. 10.13 would be required as these gates immediately precede measurement, and there is no point re-encoding before measurement. In a 4096 bit factorization, the total area of non-fault-tolerant circuit would be approximately  $2 \times 10^5$ . Assuming the rest of the Shor circuit uses sufficient error correction to be reliable, if  $p \sim 10^{-5}$ , the average number of errors in the non-fault-tolerant part of the circuit would be two — completely manageable with just a few repetitions of the entire circuit or minimal classical processing.

### 10.5 Approximations of arbitrary gates

In this section, we investigate the properties of fault-tolerant approximations of arbitrary single-qubit gates

$$U = \begin{pmatrix} \cos(\theta/2)e^{i(\alpha+\beta)/2} & \sin(\theta/2)e^{i(\alpha-\beta)/2} \\ -\sin(\theta/2)e^{i(-\alpha+\beta)/2} & \cos(\theta/2)e^{i(-\alpha-\beta)/2} \end{pmatrix}. \quad (10.27)$$

Consider Fig. 10.17. This was constructed using 1000 random matrices  $U$  of the form Eq. 10.27 with  $\alpha, \beta, \theta$  uniformly distributed in  $[0, 2\pi)$ . Optimal fault-tolerant approximations  $U_l$  were constructed of each, with the average

$\text{dist}(U, U_l)$  plotted for each  $l$ . The indicated line of best fit has the form

$$\delta = 0.292 \times 10^{-0.0511l}. \quad (10.28)$$

This equation characterizes the average number  $l$  of Steane code single-qubit fault-tolerant gates required to obtain a fault-tolerant approximation  $U_l$  of an arbitrary single-qubit gate  $U$  to within  $\delta = \text{dist}(U, U_l)$ .

An important point to note is that even with unlimited resources Eq. (10.28) does not provide a pathway to construct arbitrarily accurate gates. The accuracy of the fault-tolerant T-gate described in Section 10.3 depends critically on the accuracy of a single physical T-gate (Eq. (10.21)). Any over or under rotation at this point will be directly reflected in the output state of the logical qubit. Since half the gates in an optimal fault-tolerant approximation are T-gates, as the number of gates increases rotation errors will inevitably accumulate.

Consider the over-rotation gate

$$I_\theta = \begin{pmatrix} 1 & 0 \\ 0 & e^{i\theta} \end{pmatrix}, \quad (10.29)$$

where  $\theta \ll 1$ . For sufficiently small  $\theta$ ,  $\delta = \text{dist}(I, I_\theta) = \sqrt{3/8}\theta$ . Note that any metric on  $U(2)$  modulo global phase must have the property  $\delta \propto \theta$  and hence these results are not expected to depend on the precise metric used. In the logical T-gate, even if there is systematic over rotation in the single physical T-gate, the stochastic nature of Eq. (10.22) ensures that the final logical state will be out by a random angle  $\pm\theta$ . This implies that a fault-tolerant approximation involving  $l/2$  T-gates will be uncertain by an amount  $\delta = \sqrt{3l/16}\theta$ . The inequality  $\sqrt{3l/16}\theta < 0.292 \times 10^{-0.0511l}$  therefore

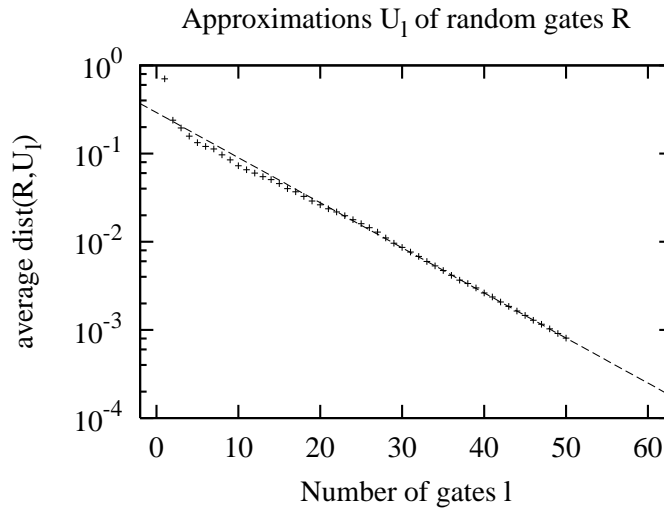


Fig. 10.17: Average accuracy of optimal fault-tolerant gate sequence approximations of length  $l$ .

sets the maximum number of gates that can meaningfully be included in a fault-tolerant approximation. Note that even if  $\theta \sim 10^{-4}$ ,  $l_{\max}$  is only 60 – a number of gates accessible using the algorithm described in this chapter.

## 10.6 Conclusion

We have described an algorithm enabling the optimal approximation of arbitrary unitary matrices given a discrete universal gate set. We have used this algorithm to investigate the properties of fault-tolerant approximations of arbitrary single-qubit gates using the gates that can be applied to a single Steane code logical qubit and found that on average an  $l$  gate approximation can be found within  $\delta = 0.292 \times 10^{-0.0511l}$  of the ideal gate. We have considered the specific case of the phase rotation gates used in Shor's algorithm and found that even the minimal complexity fault-tolerant circuits obtained are still so large that they are outperformed by non-fault-tolerant equivalents. The work here suggests that practical quantum algorithms

should avoid, where possible, logical gates that must be implemented using an approximate sequence of fault-tolerant gates. An important extension of this work would be to similarly examine the properties of fault-tolerant approximations of multiple-qubit gates and larger circuits.



## 11. Concluding remarks

Neglecting Chapters 1, 4 and 7 which contain review material only, in this thesis we

1. (Chapter 2) performed simulations of the adiabatic Kane  $^{31}\text{P}$  in  $^{28}\text{Si}$  CNOT gate suggesting that achieving a probability of error less than  $10^{-4}$  is possible provided the presence of the silicon dioxide layer, gate electrodes, and control circuitry do not reduce the experimentally measured coherence times of the  $^{31}\text{P}$  donor electron and nucleus, which were obtained in bulk  $^{28}\text{Si}$ , by more than a factor of 6.
2. (Chapter 3) performed simulations of the adiabatic Kane  $^{31}\text{P}$  in  $^{28}\text{Si}$  readout operation suggesting that the fidelity, stability, and accessibility of the states required to transfer nuclear spin information onto the donor electrons is insufficient to permit readout. We briefly outlined an alternative readout scheme based on resonant fields.
3. (Chapter 5) presented a simple 5-qubit quantum error correction (QEC) scheme designed for a linear nearest neighbor (LNN) architecture, simulating its performance when subjected to both discrete and continuous errors. Threshold error rates, at which a QEC scheme provides precisely no reduction in error, were obtained for both discrete ( $p = 1.6 \times 10^{-3}$ ) and continuous ( $\sigma = 4.7 \times 10^{-2}$ ) errors.

4. (Chapter 6) showed that it is possible to remove the need for measurement in the QEC scheme of Chapter 5 and, with the addition of four qubits, make do with slow resetting. Discrete and continuous threshold error rates were reduced to  $p = 3.7 \times 10^{-4}$  and  $\sigma = 3.1 \times 10^{-2}$  respectively.
5. (Chapter 8) presented a minimal qubit count LNN circuit implementing the quantum part of Shor's  $L$ -bit integer factoring algorithm. Achieved circuit depth and gate count identical to leading order in  $L$  to that possible when long-range interactions are available.
6. (Chapter 9) showed that Shor's algorithm can be used to factor integers  $O(4^d)$  bits long, provided single-qubit phase rotations of angle  $\pi/2^d$  can be implemented. Specifically, with sufficient qubits and error correction, we showed that a 4096 bit integer could conceivably be factored in a single day provided single-qubit phase rotations of angle  $\pi/128 \pm \pi/512$  could be implemented.
7. (Chapter 10) presented a numerical algorithm capable of obtaining optimal fault-tolerant approximations of arbitrary single-qubit gates. Used this algorithm to assess the properties of fault-tolerant approximations of single-qubit phase rotations with the conclusion that it is better to use simple non-fault-tolerant circuits to implement phase rotations in Shor's algorithm.

Significant further work is planned in three broad areas. Firstly, overcoming or coping with the lack of long-range communication in the solid-state. For example, teleportation has been proposed as a possible long-range communication technique [200, 201] but the details of how this would be implemented in practice have yet to be worked out. A threshold gate error rate

$p = 2.4 \times 10^{-6}$  below which an arbitrarily large quantum computation can be performed on an LNN architecture has been shown to exist for a simple discrete error model [125], but it is highly desirable that better LNN circuits with a higher threshold are found, and that an analysis using a more physical model of errors is performed.

Secondly, many quantum algorithms have now been proposed but very few have been analyzed for practicality, especially when only a limited set of quantum gates is available. A similar analysis to that carried out for Shor's algorithm in this thesis could be applied to quantum algorithms dealing with Poincaré recurrences and periodic orbits (classical dynamics) [202], eigenvalue calculation [11], pattern recognition [12], Schur and Clebsch-Gordon transforms (technically not algorithms in their own right) [13], numerical integrals and stochastic processes [14], black box function determination [203], Jones polynomials (knot theory) [10], a vast array of problems in the field of quantum system simulation [204, 205], a somewhat controversial algorithm related to the classically uncomputable halting problem [15], and a number of promising algorithms based on adiabatic quantum computation [16, 50]. Explicit techniques for the translation of adiabatic quantum algorithms into quantum circuits also need to be developed.

Thirdly and finally, while we have developed a quantum compiler capable of optimally approximating an arbitrary single-qubit gate, it would be extremely interesting to look at optimal approximations of larger circuits. Exact quantum compilation has received a great deal of attention [206, 207, 208] but in the worst-case results in circuits containing a number of gates that scales exponentially with the number of qubits. By contrast, the number of gates needed to approximate an arbitrary computation scales logarithmically with the required accuracy, and even if the required accuracy

increases exponentially with the number of qubits, this implies a polynomial growth of gate count.

## Appendix



## A. Simple Steane code gates

This appendix contains the complete multiplication tables of the largest possible group of fault-tolerant Steane code single logical qubit gates that can be implemented as products of single physical qubit rotations. These gates were introduced in Chapter 10. For convenience, we list these gates again below.

$$\begin{array}{ll}
 G_0 = I & G_{12} = S^\dagger X \\
 G_1 = H & G_{13} = HS \\
 G_2 = X & G_{14} = HS^\dagger \\
 G_3 = Z & G_{15} = ZXH \\
 G_4 = S & G_{16} = SXH \\
 G_5 = S^\dagger & G_{17} = S^\dagger XH \\
 G_6 = XH & G_{18} = HSH \\
 G_7 = ZH & G_{19} = HS^\dagger H \\
 G_8 = SH & G_{20} = HSX \\
 G_9 = S^\dagger H & G_{21} = HS^\dagger X \\
 G_{10} = ZX & G_{22} = S^\dagger HS \\
 G_{11} = SX & G_{23} = SHS^\dagger
 \end{array} \tag{A.1}$$

The tables on the following pages show  $G_i G_j = G_k$  with  $i$  the vertical index and  $j$  the horizontal index.

	$G_1$	$G_2$	$G_3$	$G_4$	$G_5$	$G_6$	$G_7$	$G_8$	$G_9$	$G_{10}$	$G_{11}$	$G_{12}$
$G_1$	$G_0$	$G_7$	$G_6$	$G_{13}$	$G_{14}$	$G_3$	$G_2$	$G_{18}$	$G_{19}$	$G_{15}$	$G_{20}$	$G_{21}$
$G_2$	$G_6$	$G_0$	$G_{10}$	$G_{12}$	$G_{11}$	$G_1$	$G_{15}$	$G_{17}$	$G_{16}$	$G_3$	$G_5$	$G_4$
$G_3$	$G_7$	$G_{10}$	$G_0$	$G_5$	$G_4$	$G_{15}$	$G_1$	$G_9$	$G_8$	$G_2$	$G_{12}$	$G_{11}$
$G_4$	$G_8$	$G_{11}$	$G_5$	$G_3$	$G_0$	$G_{16}$	$G_9$	$G_7$	$G_1$	$G_{12}$	$G_{10}$	$G_2$
$G_5$	$G_9$	$G_{12}$	$G_4$	$G_0$	$G_3$	$G_{17}$	$G_8$	$G_1$	$G_7$	$G_{11}$	$G_2$	$G_{10}$
$G_6$	$G_2$	$G_{15}$	$G_1$	$G_{14}$	$G_{13}$	$G_{10}$	$G_0$	$G_{19}$	$G_{18}$	$G_7$	$G_{21}$	$G_{20}$
$G_7$	$G_3$	$G_1$	$G_{15}$	$G_{21}$	$G_{20}$	$G_0$	$G_{10}$	$G_{23}$	$G_{22}$	$G_6$	$G_{14}$	$G_{13}$
$G_8$	$G_4$	$G_9$	$G_{16}$	$G_{19}$	$G_{23}$	$G_5$	$G_{11}$	$G_{14}$	$G_{21}$	$G_{17}$	$G_{18}$	$G_{22}$
$G_9$	$G_5$	$G_8$	$G_{17}$	$G_{22}$	$G_{18}$	$G_4$	$G_{12}$	$G_{20}$	$G_{13}$	$G_{16}$	$G_{23}$	$G_{19}$
$G_{10}$	$G_{15}$	$G_3$	$G_2$	$G_{11}$	$G_{12}$	$G_7$	$G_6$	$G_{16}$	$G_{17}$	$G_0$	$G_4$	$G_5$
$G_{11}$	$G_{16}$	$G_4$	$G_{12}$	$G_2$	$G_{10}$	$G_8$	$G_{17}$	$G_6$	$G_{15}$	$G_5$	$G_0$	$G_3$
$G_{12}$	$G_{17}$	$G_5$	$G_{11}$	$G_{10}$	$G_2$	$G_9$	$G_{16}$	$G_{15}$	$G_6$	$G_4$	$G_3$	$G_0$

	$G_{13}$	$G_{14}$	$G_{15}$	$G_{16}$	$G_{17}$	$G_{18}$	$G_{19}$	$G_{20}$	$G_{21}$	$G_{22}$	$G_{23}$
$G_1$	$G_4$	$G_5$	$G_{10}$	$G_{22}$	$G_{23}$	$G_8$	$G_9$	$G_{11}$	$G_{12}$	$G_{16}$	$G_{17}$
$G_2$	$G_{14}$	$G_{13}$	$G_7$	$G_9$	$G_8$	$G_{19}$	$G_{18}$	$G_{21}$	$G_{20}$	$G_{23}$	$G_{22}$
$G_3$	$G_{21}$	$G_{20}$	$G_6$	$G_{17}$	$G_{16}$	$G_{23}$	$G_{22}$	$G_{14}$	$G_{13}$	$G_{19}$	$G_{18}$
$G_4$	$G_{19}$	$G_{23}$	$G_{17}$	$G_{15}$	$G_6$	$G_{14}$	$G_{21}$	$G_{18}$	$G_{22}$	$G_{13}$	$G_{20}$
$G_5$	$G_{22}$	$G_{18}$	$G_{16}$	$G_6$	$G_{15}$	$G_{20}$	$G_{13}$	$G_{23}$	$G_{19}$	$G_{21}$	$G_{14}$
$G_6$	$G_{12}$	$G_{11}$	$G_3$	$G_{23}$	$G_{22}$	$G_{17}$	$G_{16}$	$G_5$	$G_4$	$G_9$	$G_8$
$G_7$	$G_5$	$G_4$	$G_2$	$G_{19}$	$G_{18}$	$G_9$	$G_8$	$G_{12}$	$G_{11}$	$G_{17}$	$G_{16}$
$G_8$	$G_3$	$G_0$	$G_{12}$	$G_{13}$	$G_{20}$	$G_7$	$G_1$	$G_{10}$	$G_2$	$G_{15}$	$G_6$
$G_9$	$G_0$	$G_3$	$G_{11}$	$G_{21}$	$G_{14}$	$G_1$	$G_7$	$G_2$	$G_{10}$	$G_6$	$G_{15}$
$G_{10}$	$G_{20}$	$G_{21}$	$G_1$	$G_8$	$G_9$	$G_{22}$	$G_{23}$	$G_{13}$	$G_{14}$	$G_{18}$	$G_{19}$
$G_{11}$	$G_{23}$	$G_{19}$	$G_9$	$G_1$	$G_7$	$G_{21}$	$G_{14}$	$G_{22}$	$G_{18}$	$G_{20}$	$G_{13}$
$G_{12}$	$G_{18}$	$G_{22}$	$G_8$	$G_7$	$G_1$	$G_{13}$	$G_{20}$	$G_{19}$	$G_{23}$	$G_{14}$	$G_{21}$



	$G_1$	$G_2$	$G_3$	$G_4$	$G_5$	$G_6$	$G_7$	$G_8$	$G_9$	$G_{10}$	$G_{11}$	$G_{12}$
$G_{13}$	$G_{18}$	$G_{20}$	$G_{14}$	$G_6$	$G_1$	$G_{22}$	$G_{19}$	$G_2$	$G_0$	$G_{21}$	$G_{15}$	$G_7$
$G_{14}$	$G_{19}$	$G_{21}$	$G_{13}$	$G_1$	$G_6$	$G_{23}$	$G_{18}$	$G_0$	$G_2$	$G_{20}$	$G_7$	$G_{15}$
$G_{15}$	$G_{10}$	$G_6$	$G_7$	$G_{20}$	$G_{21}$	$G_2$	$G_3$	$G_{22}$	$G_{23}$	$G_1$	$G_{13}$	$G_{14}$
$G_{16}$	$G_{11}$	$G_{17}$	$G_8$	$G_{23}$	$G_{19}$	$G_{12}$	$G_4$	$G_{21}$	$G_{14}$	$G_9$	$G_{22}$	$G_{18}$
$G_{17}$	$G_{12}$	$G_{16}$	$G_9$	$G_{18}$	$G_{22}$	$G_{11}$	$G_5$	$G_{13}$	$G_{20}$	$G_8$	$G_{19}$	$G_{23}$
$G_{18}$	$G_{13}$	$G_{19}$	$G_{22}$	$G_9$	$G_{17}$	$G_{14}$	$G_{20}$	$G_5$	$G_{12}$	$G_{23}$	$G_8$	$G_{16}$
$G_{19}$	$G_{14}$	$G_{18}$	$G_{23}$	$G_{16}$	$G_8$	$G_{13}$	$G_{21}$	$G_{11}$	$G_4$	$G_{22}$	$G_{17}$	$G_9$
$G_{20}$	$G_{22}$	$G_{13}$	$G_{21}$	$G_7$	$G_{15}$	$G_{18}$	$G_{23}$	$G_3$	$G_{10}$	$G_{14}$	$G_1$	$G_6$
$G_{21}$	$G_{23}$	$G_{14}$	$G_{20}$	$G_{15}$	$G_7$	$G_{19}$	$G_{22}$	$G_{10}$	$G_3$	$G_{13}$	$G_6$	$G_1$
$G_{22}$	$G_{20}$	$G_{23}$	$G_{18}$	$G_{17}$	$G_9$	$G_{21}$	$G_{13}$	$G_{12}$	$G_5$	$G_{19}$	$G_{16}$	$G_8$
$G_{23}$	$G_{21}$	$G_{22}$	$G_{19}$	$G_8$	$G_{16}$	$G_{20}$	$G_{14}$	$G_4$	$G_{11}$	$G_{18}$	$G_9$	$G_{17}$

	$G_{13}$	$G_{14}$	$G_{15}$	$G_{16}$	$G_{17}$	$G_{18}$	$G_{19}$	$G_{20}$	$G_{21}$	$G_{22}$	$G_{23}$
$G_{13}$	$G_9$	$G_{17}$	$G_{23}$	$G_{10}$	$G_3$	$G_5$	$G_{12}$	$G_8$	$G_{16}$	$G_4$	$G_{11}$
$G_{14}$	$G_{16}$	$G_8$	$G_{22}$	$G_3$	$G_{10}$	$G_{11}$	$G_4$	$G_{17}$	$G_9$	$G_{12}$	$G_5$
$G_{15}$	$G_{11}$	$G_{12}$	$G_0$	$G_{18}$	$G_{19}$	$G_{16}$	$G_{17}$	$G_4$	$G_5$	$G_8$	$G_9$
$G_{16}$	$G_2$	$G_{10}$	$G_5$	$G_{20}$	$G_{13}$	$G_6$	$G_{15}$	$G_0$	$G_3$	$G_1$	$G_7$
$G_{17}$	$G_{10}$	$G_2$	$G_4$	$G_{14}$	$G_{21}$	$G_{15}$	$G_6$	$G_3$	$G_0$	$G_7$	$G_1$
$G_{18}$	$G_6$	$G_1$	$G_{21}$	$G_4$	$G_{11}$	$G_2$	$G_0$	$G_{15}$	$G_7$	$G_{10}$	$G_3$
$G_{19}$	$G_1$	$G_6$	$G_{20}$	$G_{12}$	$G_5$	$G_0$	$G_2$	$G_7$	$G_{15}$	$G_3$	$G_{10}$
$G_{20}$	$G_{17}$	$G_9$	$G_{19}$	$G_0$	$G_2$	$G_{12}$	$G_5$	$G_{16}$	$G_8$	$G_{11}$	$G_4$
$G_{21}$	$G_8$	$G_{16}$	$G_{18}$	$G_2$	$G_0$	$G_4$	$G_{11}$	$G_9$	$G_{17}$	$G_5$	$G_{12}$
$G_{22}$	$G_7$	$G_{15}$	$G_{14}$	$G_{11}$	$G_4$	$G_3$	$G_{10}$	$G_1$	$G_6$	$G_0$	$G_2$
$G_{23}$	$G_{15}$	$G_7$	$G_{13}$	$G_5$	$G_{12}$	$G_{10}$	$G_3$	$G_6$	$G_1$	$G_2$	$G_0$



# Bibliography

- [1] Intel Corporation. Moore's law.  
<http://www.intel.com/research/silicon/mooreslaw.htm>, 2005.
- [2] P. S. Peercy. The drive to miniaturization. *Nature*, 406:1023–1026, 2000.
- [3] R. P. Feynman. Simulating physics with computers. *Int. J. Theor. Phys.*, 21(6–7):467–488, 1982.
- [4] D. Deutsch. Quantum theory, the Church-Turing principle and the universal quantum computer. *Proc. R. Soc. Lond. A*, 400:97–117, 1985.
- [5] A. M. Turing. On computable numbers, with an application to the entscheidungsproblem. *Proc. Lond. Math. Soc., Ser. 2*, 42:230–265, 1936.
- [6] P. W. Shor. Polynomial time algorithms for discrete logarithms and factoring on a quantum computer. In *Proc. Algorithmic Number Theory. First International Symposium, ANTS-I*, page 289, 1994.
- [7] R. L. Rivest, A. Shamir, and L. Adleman. A method for obtaining digital signatures and public-key cryptosystems. *Communications of the ACM*, 21(2):120–126, 1978.
- [8] P. Zimmerman. Pretty good privacy. [www.pgp.com](http://www.pgp.com), 1991.

- [9] A. Yu. Kitaev. Quantum measurements and the abelian stabilizer problem. Technical Report TR96-003, Electronic Colloquium on Computational Complexity, 1996. quant-ph/9511026.
- [10] V. Subramaniam and P. Ramadevi. Quantum computation of Jones' polynomials. *quant-ph/0210095*, 2002.
- [11] P. Jaksch and A. Papageorgiou. Eigenvector approximation leading to exponential speedup of quantum eigenvalue calculation. *Phys. Rev. Lett.*, 91:257902, 2003. quant-ph/0308016.
- [12] R. Schützhold. Pattern recognition on a quantum computer. *Phys. Rev. A*, 67:062311, 2003. quant-ph/0208063.
- [13] D. Bacon, I. L. Chuang, and A. W. Harrow. Efficient quantum circuits for Schur and Clebsch-Gordan transforms. *quant-ph/0407082*, 2004.
- [14] D. S. Abrams and C. P. Williams. Fast quantum algorithms for numerical integrals and stochastic processes. *quant-ph/9908083*, 1999.
- [15] T. D. Kieu. An anatomy of a quantum adiabatic algorithm that transcends the turing computability. *quant-ph/0407090*, 2004.
- [16] E. Farhi, J. Goldstone, S. Gutmann, J. Lapan, A. Lundgren, and D. Preda. A quantum adiabatic evolution algorithm applied to random instances of an NP-complete problem. *Science*, 292:472–475, 2001. quant-ph/0104129.
- [17] H.-K. Lo and H. F. Chau. Unconditional security of quantum key distribution over arbitrarily long distances. *Science*, 283:2050–2056, 1999. quant-ph/9803006.
- [18] B. Gelfond. Magiq technologies. [www.magiqtech.com](http://www.magiqtech.com), 2002.

- 
- [19] G. Ribordy, O. Guinnard, N. Gisin, and H. Zbinden. id quantique. [www.idquantique.com](http://www.idquantique.com), 2004.
- [20] id Quantique. Secure data archiving thanks to quantum cryptography. world premiere application of this promising technology. [www.idquantique.com/crypto-press-engl.html](http://www.idquantique.com/crypto-press-engl.html), 2004.
- [21] J. Faber and G. A. Giraldi. Models for quantum neural networks. [virtual01.lncc.br/giraldi/qc/Quantum-Neural-Nets/Research/Research.html](http://virtual01.lncc.br/giraldi/qc/Quantum-Neural-Nets/Research/Research.html), 2002.
- [22] S. Gupta and R. K. P. Zia. Quantum neural networks. *J. Comp. Sys. Sci.*, pages 355–383, 2002. [quant-ph/0201144](http://quant-ph/0201144).
- [23] J. Yepez. Type-ii quantum computers. *Int. J. Mod. Phys. C*, 12:1273–1284, 2001.
- [24] C. S. Lent, P. D. Tougaw, W. Porod, and G. H. Bernstein. Quantum cellular automata. *Nanotechnology*, 4:49–57, 1993.
- [25] M. J. Hadamard. Résolution dune question relative aux déterminants. *Bulletin des Sciences Mathématiques*, XVII:240–246, 1893.
- [26] M. J. L. Walsh. A closed set of normal orthogonal functions. *American Journal of Mathematics*, XLV:5–24, 1923.
- [27] R. Cleve, A. Ekert, C. Macchiavello, and M. Mosca. Quantum algorithms revisited. *Proc. R. Soc. Lond. A*, 454:339–354, 1998. [quant-ph/9708016](http://quant-ph/9708016).
- [28] D. P. DiVincenzo. Two-bit gates are universal for quantum computation. *Phys. Rev. A*, 51:1015–1022, 1995. [cond-mat/9407022](http://cond-mat/9407022).

- [29] M. J. Bremner, C. M. Dawson, J. L. Dodd, A. Gilchrist, A. W. Harrow, D. Mortimer, M. A. Nielsen, and T. J. Osborne. A practical scheme for quantum computation with any two-qubit entangling gate. *Phys. Rev. Lett.*, 89:247902, 2002. quant-ph/0207072.
- [30] M. A. Nielsen and I. L. Chuang. *Quantum Computation and Quantum Information*. Cambridge University Press, Cambridge, 2000.
- [31] P. Rungta, W. J. Munro, K. Nemoto, P. Deuar, G. J. Milburn, and C. M. Caves. Qudit entanglement. In H. J. Carmichael, R. J. Glauber, and M. O. Scully, editors, *Directions in Quantum Optics: A Collection of Papers Dedicated to the Memory of Dan Walls*. Springer-Verlag, Berlin, 2000. quant-ph/0001075.
- [32] G. Gour. Faithful teleportation with partially entangled states. *Phys. Rev. A*, 70(042301), 2004. quant-ph/0402133.
- [33] E. Knill. Non-binary unitary error bases and quantum codes. Technical Report LAUR-96-2717, Los Alamos National Laboratory, 1996. quant-ph/9608048.
- [34] M. Rötteler M. Grassl and T. Beth. Efficient quantum circuits for non-qubit quantum error-correcting codes. *Int. J. Found. Comp. Sci.*, 14:757–775, 2003. quant-ph/0211014.
- [35] N. J. Cerf, M. Bourennane, A. Karlsson, and N. Gisin. Security of quantum key distribution using d-level systems. *Phys. Rev. Lett.*, 88:127902, 2002. quant-ph/0107130.
- [36] V. Karimipour, S. Bagherinezhad, and A. Bahraminasab. Quantum key distribution for  $d$ -level systems with generalized Bell states. *Phys. Rev. A*, 65:052331, 2002. quant-ph/0111091.

- 
- [37] M. J. Bremner, D. Bacon, and M. A. Nielsen. Simulating Hamiltonian dynamics using many-qudit Hamiltonians and local unitary control. *quant-ph/0405115*, 2004.
  - [38] J. L. Cereceda. Generalization of the Deutsch algorithm using two qudits. *quant-ph/0407253*, 2004.
  - [39] H. H. Adamyany and G. Yu. Kryuchkyan. Continuous variable entanglement of phase locked light beams. *quant-ph/0406128*, 2004.
  - [40] J. A. Smolin. The continuous variable quantum teleportation controversy. *quant-ph/0407009*, 2004.
  - [41] R. L. Barnes. Stabilizer codes for continuous-variable quantum error correction. *quant-ph/0405064*, 2004.
  - [42] R. Namiki and T. Hirano. Practical limitation for continuous-variable quantum cryptography using coherent states. *Phys. Rev. Lett.*, 92:117901, 2004. *quant-ph/0403115*.
  - [43] A. K. Pati, S. L. Braunstein, and S. Lloyd. Quantum searching with continuous variables. *quant-ph/0002082*, 2000.
  - [44] A. K. Pati and S. L. Braunstein. Deutsch-Jozsa algorithm for continuous variables. In S. L. Braunstein and A. K. Pati, editors, *Quantum Information with Continuous Variables*. Kluwer Academic Publishers, Dordrecht, 2002. *quant-ph/0207108*.
  - [45] S. J. Lomonaco Jr. and L. H. Kauffman. A continuous variable Shor algorithm. *quant-ph/0210141*, 2002.
  - [46] S. J. Lomonaco Jr. and L. H. Kauffman. Continuous quantum hidden

- subgroup algorithms. In *Proc. SPIE*, volume 5105, pages 80–88, 2003. quant-ph/0304084.
- [47] E. Farhi, J. Goldstone, S. Gutmann, and M. Sipser. Quantum computation by adiabatic evolution. *quant-ph/0001106*, 2000.
- [48] D. Aharonov, W. van Dam, J. Kempe, Z. Landau, S. Lloyd, and O. Regev. Adiabatic quantum computation is equivalent to standard quantum computation. *quant-ph/0405098*, 2004.
- [49] J. Kempe, A. Kitaev, and O. Regev. The complexity of the local hamiltonian problem. *quant-ph/0406180*, 2004.
- [50] A. M. Childs, E. Farhi, J. Goldstone, and S. Gutmann. Finding cliques by quantum adiabatic evolution. *Quant. Info. Comp.*, 2:181–191, 2002. quant-ph/0012104.
- [51] V. N. Smelyanskiy, U. von Toussaint, and D. A. Timucin. Dynamics of quantum adiabatic evolution algorithm for number partitioning. *quant-ph/0202155*, 2002.
- [52] L.-A. Wu, M. S. Byrd, and D. A. Lidar. Polynomial-time simulation of pairing models on a quantum computer. *Phys. Rev. Lett.*, 89:057904, 2002. quant-ph/0108110.
- [53] V. N. Smelyanskiy, U. von Toussaint, and D. A. Timucin. Simulations of the adiabatic quantum optimization for the set partition problem. *quant-ph/0112143*, 2001.
- [54] H. J. Briegel and R. Raussendorf. Persistent entanglement in arrays of interacting particles. *Phys. Rev. Lett.*, 86:910–913, 2001. quant-ph/0004051.



- 
- [55] R. Raussendorf and H. J. Briegel. A one-way quantum computer. *Phys. Rev. Lett.*, 86:5188–5191, 2001.
- [56] R. Raussendorf, D. E. Browne, and H. J. Briegel. Measurement-based quantum computation on cluster states. *quant-ph/0301052*, 2003.
- [57] D. L. Zhou, B. Zeng, Z. Xu, and C. P. Sun. Quantum computation based on  $d$ -level cluster state. *Phys. Rev. A*, 68:062303, 2003. *quant-ph/0304054*.
- [58] M. Hein, J. Eisert, and H. J. Briegel. Multi-party entanglement in graph states. *Phys. Rev. A*, 69:062311, 2004. *quant-ph/0307130*.
- [59] B. Zeng, D. L. Zhou, Z. Xu, and C. P. Sun. Quantum teleportation using cluster states. *quant-ph/0304165*, 2003.
- [60] D. Schlingemann. Quantum error correcting codes and one-way quantum computing: Towards a quantum memory. *quant-ph/0308022*, 2003.
- [61] M. A. Nielsen and C. M. Dawson. Fault-tolerant quantum computation with cluster states. *quant-ph/0405134*, 2004.
- [62] W. Dür, H. Aschauer, and H.-J. Briegel. Multiparticle entanglement purification for graph states. *Phys. Rev. Lett.*, 91:107903, 2003. *quant-ph/0303087*.
- [63] D. Schlingemann. Logical network implementation for cluster states and graph codes. *Quant. Info. Comp.*, 3:431–449, 2003. *quant-ph/0202007*.
- [64] M. A. Nielsen. Optical quantum computation using cluster states. *quant-ph/0402005*, 2004.

- [65] D. E. Browne and T. Rudolph. Efficient linear optical quantum computation. *quant-ph/0405157*, 0405157.
- [66] S. D. Barrett and P. Kok. Efficient high-fidelity quantum computation using matter qubits and linear optics. *quant-ph/0408040*, 2004.
- [67] A. Yu. Kitaev. Fault-tolerant quantum computation by anyons. *quant-ph/9707021*, 1997.
- [68] R. Walter Ogburn and John Preskill. Topological quantum computation. *Lecture Notes in Computer Science*, 1509:341–356, 1999.
- [69] M. H. Freedman, A. Kitaev, M. J. Larsen, and Z. Wang. Topological quantum computation. *Bulletin of the American Mathematical Society*, 40:31–38, 2003. *quant-ph/0101025*.
- [70] C. Mochon. Anyons from non-solvable finite groups are sufficient for universal quantum computation. *Phys. Rev. A*, 67:022315, 2003. *quant-ph/0206128*.
- [71] C. Mochon. Anyon computers with smaller groups. *Phys. Rev. A*, 69:032306, 2004. *quant-ph/0306063*.
- [72] S. Lloyd. Quantum computation with Abelian anyons. *quant-ph/0004010*, 2000.
- [73] D. V. Averin and V. J. Goldman. Quantum computation with quasi-particles of the fractional quantum Hall effect. *Solid State Commun.*, 121:25–28, 2002. *cond-mat/0110193*.
- [74] B. Paredes, P. Fedichev, J. I. Cirac, and P. Zoller.  $\frac{1}{2}$ -anyons in small atomic Bose-Einstein condensates. *Phys. Rev. Lett.*, 87:010402, 2001. *cond-mat/0103251*.

- 
- [75] B. J. Overbosch and F. A. Bais. Inequivalent classes of interference experiments with non-Abelian anyons. *Phys. Rev. A*, 64:062107, 2001. quant-ph/0105015.
- [76] L.-M. Duan, E. Demler, and M. D. Lukin. Controlling spin exchange interactions of ultracold atoms in optical lattices. *Phys. Rev. Lett.*, 91:090402, 2003. cond-mat/0210564.
- [77] Y. Aharonov and D. Bohm. Significance of electromagnetic potentials in quantum theory. *Phys. Rev.*, 115:485–491, 1959.
- [78] M. V. Berry. Quantal phase factors accompanying adiabatic phase changes. *Proc. R. Soc. Lond. A*, 392:45–47, 1984.
- [79] J. A. Jones, V. Vedral, A. Ekert, and G. Castagnoli. Geometric quantum computation using nuclear magnetic resonance. *Nature*, 403:869–871, 2000.
- [80] G. Falci, R. Fazio, G. M. Palma, J. Siewert, and V. Vedral. Detection of geometric phases in superconducting nanocircuits. *Nature*, 407:355–358, 2000.
- [81] S.-L. Zhu and P. Zanardi. Geometric quantum gates robust against stochastic control errors. *quant-ph/0407177*, 2004.
- [82] D. Cory, A. Fahmy, and T. Havel. Nuclear magnetic resonance spectroscopy: an experimentally accessible paradigm for quantum computing. In T. Toffoli, M. Biafore, and J. Leo, editors, *Proceedings of the 4th Workshop on Physics and Computation*. New England Complex Systems Institute, 1996.
- [83] J. I. Cirac and P. Zoller. Quantum computations with cold trapped ions. *Phys. Rev. Lett.*, 74:4091–4094, 1995.

- [84] J. I. Cirac, P. Zoller, H. J. Kimble, and H. Mabuchi. Quantum state transfer and entanglement distribution among distant nodes in a quantum network. *Phys. Rev. Lett.*, 78:3221–3224, 1997. quant-ph/9611017.
- [85] L.-M. Duan, B. B. Blinov, D. L. Moehring, and C. Monroe. Scalable trapped ion quantum computation with a probabilistic ion-photon mapping. *Quant. Info. Proc.*, 4:165–173, 2004. quant-ph/0401020.
- [86] J. I. Cirac and P. Zoller. A scalable quantum computer with ions in an array of microtraps. *Nature*, 404:579–581, 2000.
- [87] D. Kielpinski, C. Monroe, and D. J. Wineland. Architecture for a large-scale ion-trap quantum computer. *Nature*, 417:709–711, 2002.
- [88] E. Knill, R. Laflamme, and G. J. Milburn. A scheme for efficient quantum computation with linear optics. *Nature*, 409:46–52, 2001.
- [89] Yu. Makhlin, G. Schön, and A. Shnirman. Josephson-junction qubits with controlled couplings. *Nature*, 398:305–307, 1999.
- [90] Y. Nakamura, Yu. A. Pashkin, and J. S. Tsai. Coherent control of macroscopic quantum states in a single-Cooper-pair box. *Nature*, 398:786–788, 1999.
- [91] M. F. Bocko, A. M. Herr, and M. J. Feldman. Prospects for quantum coherent computation using superconducting electronics. *IEEE Trans. Appl. Supercond.*, 7:3638–3641, 1997.
- [92] D. Loss and D. P. DiVincenzo. Quantum computation with quantum dots. *Phys. Rev. A*, 57:120–126, 1998. cond-mat/9701055.

- 
- [93] B. E. Kane. A silicon-based nuclear spin quantum computer. *Nature*, 393:133–137, 1998.
- [94] R. Vrijen, E. Yablonovitch, K. Wang, H. W. Jiang, A. Balandin, V. Roychowdhury, T. Mor, and D. DiVincenzo. Electron spin resonance transistors for quantum computing in silicon-germanium heterostructures. *Phys. Rev. A*, 62:012306, 2000. quant-ph/9905096.
- [95] C. D. Hill, L. C. L. Hollenberg, A. G. Fowler, C. J. Wellard, A. D. Greentree, and H.-S. Goan. Global control and fast solid-state donor electron spin quantum computing. *quant-ph/0411104*, 2004.
- [96] B. E. Kane. Silicon-based quantum computation. *Fortschr. Physik*, 48(9–11):1023–1041, 2000. quant-ph/0003031.
- [97] A. J. Skinner, M. E. Davenport, and B. E. Kane. Hydrogenic spin quantum computing in silicon: a digital approach. *Phys. Rev. Lett.*, 90:087901, 2003. quant-ph/0206159.
- [98] R. de Sousa, J. D. Delgado, and S. Das Sarma. Silicon quantum computation based on magnetic dipolar coupling. *Phys. Rev. A*, 70:052304, 2004. cond-mat/0311403.
- [99] L. C. L. Hollenberg, A. S. Dzurak, C. Wellard, A. R. Hamilton, D. J. Reilly, G. J. Milburn, and R. G. Clark. Charge-based quantum computing using single donors in semiconductors. *Phys. Rev. B*, 69:113301, 2004. cond-mat/0306235.
- [100] A. M. Stoneham, A. J. Fisher, and P. T. Greenland. Optically driven silicon-based quantum gates with potential for high-temperature operation. *J. Phys.: Cond. Mat.*, 15:L447–L451, 2003.

- [101] B. Golding and M. I. Dykman. Acceptor-based silicon quantum computing. *cond-mat/0309147*, 2003.
- [102] T. D. Ladd, J. R. Goldman, F. Yamaguchi, Y. Yamamoto, E. Abe, and K. M. Itoh. An all silicon quantum computer. *Phys. Rev. Lett.*, 89:017901, 2002. quant-ph/0109039.
- [103] P. M. Platzman and M. I. Dykman. Quantum computing with electrons floating on liquid helium. *Science*, 284:1967–1969, 1999.
- [104] Q. A. Turchette, C. J. Hood, W. Lange, H. Mabuchi, and H. J. Kimble. Measurement of conditional phase shifts for quantum logic. *Phys. Rev. Lett.*, 75:4710–4713, 1995.
- [105] T. Pellizzari, S. A. Gardiner, J. I. Cirac, and P. Zoller. Decoherence, continuous observation, and quantum computing: A cavity qed model. *Phys. Rev. Lett.*, 75:3788–3791, 1995.
- [106] G. K. Brennen, C. M. Caves, P. S. Jessen, and I. H. Deutsch. Quantum logic gates in optical lattices. *Phys. Rev. Lett.*, 82:1060–1063, 1999. quant-ph/9806021.
- [107] P. Jaksch, H.-J. Briegel, J. I. Cirac, C. W. Gardiner, and P. Zoller. Entanglement of atoms via cold controlled collisions. *Phys. Rev. Lett.*, 82:1975–1978, 1999. quant-ph/9810087.
- [108] V. Privman, I. D. Vagner, and G. Kventsel. Quantum computation in quantum-hall systems. *Phys. Lett. A*, 239:141–146, 1998. quant-ph/9707017.
- [109] D. P. DiVincenzo. The physical implementation of quantum computation. *Fortschr. Phys.*, 48:771–783, 2000. quant-ph/0002077.

- 
- [110] D. W. Leung, M. A. Nielsen, I. L. Chuang, and Yoshihisa Yamamoto. Approximate quantum error correction can lead to better codes. *Phys. Rev. A*, 56:2567–2573, 1997. quant-ph/9704002.
- [111] P. W. Shor. Algorithms for quantum computation: Discrete logarithms and factoring. In *Proc. 35th Annual Symposium on Foundations of Computer Science*, pages 124–134, 1994.
- [112] R. Laflamme, C. Miquel, J. P. Paz, and W. H. Zurek. Perfect quantum error correcting code. *Phys. Rev. Lett.*, 77:198, 1996. quant-ph/9602019.
- [113] A. M. Steane. Multiple particle interference and quantum error correction. *Proc. R. Soc. Lond. A*, 425:2551–2576, 1996. quant-ph/9601029.
- [114] A. R. Calderbank and P. W. Shor. Good quantum error-correcting codes exist. *Phys. Rev. A*, 54(2):1098–1105, 1995. quant-ph/9512032.
- [115] D. Gottesman. A class of quantum error-correcting codes saturating the quantum hamming bound. *Phys. Rev. A*, 54:1862–1868, 1996. quant-ph/9604038.
- [116] H. Pollatsek and M. B. Ruskai. Permutationally invariant codes for quantum error correction. *Lin. Alg. App.*, 392:255–288, 2004. quant-ph/0304153.
- [117] D. Gottesman. *Stabilizer Codes and Quantum Error Correction*. PhD thesis, Caltech, May 1997. quant-ph/9705052.
- [118] D. Gottesman. Theory of fault-tolerant quantum computation. *Phys. Rev. A*, 57:127–137, 1998. quant-ph/9702029.

- 
- [119] R. Solovay. Unknown title. Proof of Solovay-Kitaev Theorem, unpublished, 1995.
  - [120] A. Yu. Kitaev. Quantum computations: Algorithms and error correction. *Russ. Math. Surv.*, 52(6):1191–1249, 1997.
  - [121] A. W. Harrow, B. Recht, and I. L. Chuang. Efficient discrete approximations of quantum gates. *J. Math. Phys.*, 43:4445, 2002. quant-ph/0111031.
  - [122] E. Knill, R. Laflamme, and W. H. Zurek. Accuracy threshold for quantum computation. Technical Report LAUR-96-2199, Los Alamos National Laboratory, 1996. quant-ph/9610011.
  - [123] K. M. Svore, B. M. Terhal, and D. P. DiVincenzo. Local fault-tolerant quantum computation. *quant-ph/0410047*, 2004.
  - [124] D. Aharonov and M. Ben-Or. Fault-tolerant quantum computation with constant error rate. *quant-ph/9906129*, 1999.
  - [125] T. Szkopek, H. Fan, V. Roychowdhury, E. Yablonovitch, P. O. Boykin, G. Simms, M. Gyure, and B. Fong. Threshold error penalty for fault tolerant computation with nearest neighbour communication. *quant-ph/0411111*, 2004.
  - [126] A. M. Steane. Fast fault-tolerant filtering of quantum codewords. *quant-ph/0202036*, 2002.
  - [127] A. M. Steane. Overhead and noise threshold of fault-tolerant quantum error correction. *Phys. Rev. A*, 68:042322, 2003. quant-ph/0207119.
  - [128] B. W. Reichardt. Improved ancilla preparation scheme increases fault-tolerant threshold. *quant-ph/0406025*, 2004.



- 
- [129] E. Knill. Fault-tolerant postselected quantum computation: Schemes. *quant-ph/0402171*, 2004.
- [130] E. Knill. Fault-tolerant postselected quantum computation: Threshold analysis. *quant-ph/0404104*, 2004.
- [131] E. Knill. Quantum computing with very noisy devices. *quant-ph/0410199*, 2004.
- [132] A. G. Fowler, C. J. Wellard, and L. C. L. Hollenberg. Error rate of the Kane quantum computer controlled-NOT gate in the presence of dephasing. *Phys. Rev. A*, 67:012301, 2003. *quant-ph/0207103*.
- [133] L. C. L. Hollenberg, C. J. Wellard, C. I. Pakes, and A. G. Fowler. Single-spin readout for buried dopant semiconductor qubits. *Phys. Rev. B*, 69:233301, 2004. *quant-ph/0402077*.
- [134] A. G. Fowler, C. D. Hill, and L. C. L. Hollenberg. Quantum-error correction on linear-nearest-neighbor qubit arrays. *Phys. Rev. A*, 69:042314, 2004. *quant-ph/0311116*.
- [135] A. G. Fowler, S. J. Devitt, and L. C. L. Hollenberg. Implementation of Shor’s algorithm on a linear nearest neighbour qubit array. *Quant. Info. Comp.*, 4:237, 2004. *quant-ph/0402196*.
- [136] A. G. Fowler and L. C. L. Hollenberg. Scalability of Shor’s algorithm with a limited set of rotation gates. *Phys. Rev. A*, 70:032329, 2004. *quant-ph/0306018*.
- [137] G. Feher and E. A. Gere. Electron spin resonance experiments on donors in silicon. II. electron spin relaxation effects. *Phys. Rev.*, 114(5):1245, 1959.

- 
- [138] A. M. Tyryshkin, S. A. Lyon, A. V. Astashkin, and A. M. Raitsimring. Electron spin-relaxation times of phosphorus donors in silicon. *Phys. Rev. B*, 68:193207, 2003. cond-mat/0303006.
- [139] L. M. Kettle, H.-S. Goan, S. C. Smith, L. C. L. Hollenberg, and C. J. Wellard. The effects of j-gate potential and interfaces on donor exchange coupling in the kane quantum computer architecture. *J. Phys.: Cond. Mat.*, 16:1011–1023, 2004. cond-mat/0402183.
- [140] C. J. Wellard, L. C. L. Hollenberg, L. M. Kettle, and H.-S. Goan. Voltage control of exchange coupling in phosphorus doped silicon. *J. Phys.: Cond. Mat.*, 16:5697–5704, 2004. quant-ph/0402642.
- [141] H.-S. Goan and G. J. Milburn. Silicon-based electron-mediated nuclear spin quantum computer. *Internal SRC report*, 2000.
- [142] X. Hu, R. de Sousa, and S. Das Sarma. Decoherence and dephasing in spin-based solid state quantum computers. *cond-mat/0108339*, 2001.
- [143] A. Honig and E. Stupp. Electron spin-lattice relaxation in phosphorus-doped silicon. *Phys. Rev.*, 117:69–83, 1960.
- [144] C. D. Hill and H.-S. Goan. Fast non-adiabatic two qubit gates for the Kane quantum computer. *Phys. Rev. A*, 68:012321, 2003. quant-ph/0305040.
- [145] Belita Koiller, Xuedong Hu, and S. Das Sarma. Exchange in silicon-based quantum computer architecture. *Phys. Rev. Lett.*, 88:027903, 2002. cond-mat/0106259.
- [146] A. A. Larionov, L. E. Fedichkin, A. A. Kokin, and K. A. Valiev. The nuclear magnetic resonance spectrum of  $^{31}\text{P}$  donors in a silicon quantum computer. *Nanotechnology*, 11:392–396, 2000. quant-ph/0012005.

- 
- [147] K. A. Valiev and A. A. Kokin. Solid-state NMR quantum computer with individual access to qubits and some its ensemble developments. *quant-ph/9909008*, 1999.
- [148] L. M. Kettle, H.-S. Goan, S. C. Smith, C. J. Wellard, L. C. L. Hollenberg, and C. I. Pakes. Numerical study of hydrogenic effective mass theory for an impurity p donor in si in the presence of an electric field and interfaces. *Phys. Rev. B*, 68:075317, 2003. cond-mat/0308124.
- [149] B. H. Bransden and C. J. Joachain. *Introduction to Quantum Mechanics*. Wiley, New York, 1989.
- [150] C. Wellard. *Spin Dynamics and Quantum Computation*. PhD thesis, University of Melbourne, June 2001.
- [151] W. R. Bauer and W. Nadler. Spin dephasing in the extended strong collision approximation. *Phys. Rev. E*, 65:066123, 2002. cond-mat/0204325.
- [152] G. Burkard, D. Loss, and D. P. DiVincenzo. Coupled quantum dots as quantum gates. *Phys. Rev. B*, 59(3):2070, 1999. cond-mat/9808026.
- [153] K. Kimm and H.-H. Kwon. Decoherence of the quantum gate in Milburn’s model of decoherence. *Phys. Rev. A*, 65:022311, 2002.
- [154] D. Mozysky, Sh. Kogan, and G. P. Berman. Time scales of phonon-induced decoherence of semiconductor spin qubits. *Phys. Rev. B*, 65:245213, 2002. cond-mat/0112135.
- [155] R. de Sousa and S. Das Sarma. Electron spin coherence in semiconductors: Considerations for a spin-based solid-state quantum computer architecture. *Phys. Rev. B*, 67:033301, 2003. cond-mat/0203101.

- [156] M. Thorwart and Peter Hänggi. Decoherence and dissipation during a quantum XOR gate operation. *Phys. Rev. A*, 65:012309, 2002. cond-mat/0104513.
- [157] C. D. Hill and H.-S. Goan. Gates for the Kane quantum computer in the presence of dephasing. *Phys. Rev. A*, 70:022310, 2004. quant-ph/0405042.
- [158] D. P. DiVincenzo, D. Bacon, J. Kempe, G. Burkard, and K. B. Whaley. The physical implementation of quantum computation. *Nature*, 408:339–342, 2000. quant-ph/0002077.
- [159] C. J. Wellard, L. C. L. Hollenberg, F. Parisoli, L. M. Kettle, H.-S. Goan, J. A. L. McIntosh, and D. N. Jamieson. Electron exchange coupling for single-donor solid-state spin qubits. *Phys. Rev. B*, 68:195209, 2003. cond-mat/0309417.
- [160] A. D. Greentree, A. R. Hamilton, L. C. L. Hollenberg, and R. G. Clark. Electrical readout of a spin qubit without double occupancy. *cond-mat/0403449*, 2004.
- [161] Yu. Makhlin. Nonlocal properties of two-qubit gates and mixed states and optimization of quantum computations. *Quant. Info. Proc.*, 1:243–252, 2002. quant-ph/0002045.
- [162] B. Kraus and J. I. Cirac. Optimal creation of entanglement using a two-qubit gate. *Phys. Rev. A*, 63:062309, 2001. quant-ph/0011050.
- [163] J. Zhang, J. Vala, K. Birgitta Whaley, and S. Sastry. Geometric theory of nonlocal two-qubit operations. *Phys. Rev. A*, 67:042313, 2003. quant-ph/0209120.

- 
- [164] A. M. Childs, H. L. Haselgrove, and M. A. Nielsen. Lower bounds on the complexity of simulating quantum gates. *Phys. Rev. A*, 68:052311, 2003. quant-ph/0307190.
- [165] N. Khaneja, R. Brockett, and S. J. Glaser. Time optimal control in spin systems. *Phys. Rev. A*, 63:032308, 2001. quant-ph/0006114.
- [166] K. Hammerer, G. Vidal, and J. I. Cirac. Characterization of non-local gates. *Phys. Rev. A*, 66:062321, 2002. quant-ph/0205100.
- [167] S. Hill and W. K. Wootters. Entanglement of a pair of quantum bits. *Phys. Rev. Lett.*, 78:5022, 1997. quant-ph/9703041.
- [168] D. Gottesman. Fault-tolerant quantum computation with local gates. *J. Mod. Optic.*, 47:333–345, 2000. quant-ph/9903099.
- [169] L. Tian and P. Zoller. Quantum computing with atomic Josephson junction arrays. *Phys. Rev. A*, 68:042321, 2003. quant-ph/0306085.
- [170] M. Feng, I. D’Amico, P. Zanardi, and F. Rossi. Spin-based quantum gating with semiconductor quantum dots by bichromatic radiation method. *Europhys. Lett.*, 66(1):14, 2004. quant-ph/0304169.
- [171] J. K. Pachos and P. L. Knight. Quantum computation with a one-dimensional optical lattice. *Phys. Rev. Lett.*, 91:107902, 2003. quant-ph/0301084.
- [172] L. M. K. Vandersypen, R. Hanson, L. H. Willems van Beveren, J. M. Elzerman, J. S. Greidanus, S. De Franceschi, and L. P. Kouwenhoven. Quantum computing with electron spins in quantum dots. In A. J. Leggett, B. Ruggiero, and P. Silvestrini, editors, *Quantum Computing and Quantum Bits in Mesoscopic Systems*. Kluwer Academic/Plenum Publishers, New York, 2003. quant-ph/0207059.

- [173] P. Solinas, P. Zanardi, N. Zanghi, and F. Rossi. Semiconductor-based geometrical quantum gates. *Phys. Rev. B*, 67:121307, 2003. quant-ph/0207019.
- [174] J. H. Jefferson, M. Fearn, D. L. J. Tipton, and T. P. Spiller. Two-electron quantum dots as scalable qubits. *Phys. Rev. A*, 66:042328, 2002. quant-ph/0206075.
- [175] D. Petrosyan and G. Kurizki. Scalable solid-state quantum processor using subradiant two-atom states. *Phys. Rev. Lett.*, 89:207902, 2002. quant-ph/0205174.
- [176] V. V'yurkov and L. Y. Gorelik. Charge based quantum computer without charge transfer. *Quant. Comput. and Comput.*, 1(1):77–83, 2000. quant-ph/0009099.
- [177] E. O. Kamenetskii and O. Voskoboinikov. On implementation of ferrite magnetostatic/magnetoelectric particles for quantum computation. *cond-mat/0310558*, 2003.
- [178] S. L. Braunstein and J. A. Smolin. Perfect quantum error correction coding in 24 laser pulses. *Phys. Rev. A*, 55:945, 1997. quant-ph/9604036.
- [179] E. Knill, R. Laflamme, R. Martinez, and C. Negrevergne. Benchmarking quantum computers: The five-qubit error correcting code. *Phys. Rev. Lett.*, 86:5811, 2001. quant-ph/0101034.
- [180] J. Niwa, K. Matsumoto, and H. Imai. Simulating the effects of quantum error-correction schemes. *quant-ph/0211071*, 2002.
- [181] C. H. Bennett, D. P. DiVincenzo, J. A. Smolin, and W. K. Wootters.

- 
- Mixed state entanglement and quantum error correction. *Phys. Rev. A*, 54:3824, 1996. quant-ph/9604024.
- [182] A. Barenco, T. A. Brun, R. Schack, and T. P. Spiller. Effects of noise on quantum error correction algorithms. *Phys. Rev. A*, 56:1177–1188, 1997. quant-ph/9612047.
- [183] P. O. Boykin, T. Mor, V. Roychowdhury, and F. Vatan. Algorithms on ensemble quantum computers. *quant-ph/9907067*, 1999.
- [184] P. W. Shor. Polynomial time algorithms for discrete logarithms and factoring on a quantum computer. *SIAM J. Comput.*, 26:1484, 1997. quant-ph/9508027.
- [185] R. Van Meter and K. M. Itoh. Fast quantum modular exponentiation. *quant-ph/0408006*, 2004.
- [186] V. Vedral, A. Barenco, and A. Ekert. Quantum networks for elementary arithmetic operations. *Phys. Rev. A*, 54:147–153, 1996. quant-ph/9511018.
- [187] D. Beckman, A. N. Chariy, S. Devabhaktuniz, and J. Preskill. Efficient networks for quantum factoring. *quant-ph/9602016*, 1996.
- [188] P. Gossett. Quantum carry-save arithmetic. *quant-ph/9808061*, 1998.
- [189] T. G. Draper, S. A. Kutin, E. M. Rains, and K. M. Svore. A logarithmic-depth quantum carry-lookahead adder. *quant-ph/0406142*, 2004.
- [190] C. Zalka. Fast versions of Shor’s quantum factoring algorithm. *quant-ph/9806084*, 1998.

- 
- [191] S. Beauregard. Circuit for Shor's algorithm using  $2n+3$  qubits. *Quantum Inform. Compu.*, 3(2):175–185, 2003. quant-ph/0205095.
- [192] D. Coppersmith. An approximate Fourier transform useful in quantum factoring. Technical Report RC19642, T. J. Watson Research Center, IBM Corporation, 1994. quant-ph/0201067.
- [193] T. G. Draper. Addition on a quantum computer. *quant-ph/0008033*, 2000.
- [194] S. Parker and M. B. Plenio. Efficient factorization with a single pure qubit and  $\log(N)$  mixed qubits. *Phys. Rev. Lett.*, 85:3049–3052, 2000. quant-ph/0001066.
- [195] S. J. Devitt, A. G. Fowler, and L. C. L. Hollenberg. Simulations of Shor's algorithm with implications to scaling and quantum error correction. *quant-ph/0408081*, 2004.
- [196] G. Burkard, H.-A. Engel, and D. Loss. Spintronics and quantum dots for quantum computing and quantum communication. *Fortschr. Physik*, 48(9–11):965–986, 2000. cond-mat/0004182.
- [197] A. Yu. Kitaev, A. H. Shen, and M. N. Vyalyi. *Classical and Quantum Computation*. American Mathematical Society, Providence, RI, 2002.
- [198] C. Dawson. The Solovay-Kitaev quantum compiler. [www.physics.uq.edu.au/people/dawson/sk/index.html](http://www.physics.uq.edu.au/people/dawson/sk/index.html), 2004.
- [199] J. Preskill. Fault-tolerant quantum computation. *quant-ph/9712048*, 1997.
- [200] D. Copsey, M. Oskin, F. Impens, T. Metodiev, A. Cross, F. T. Chong, I. L. Chuang, and John Kubiatawicz. Toward a scalable, silicon-based



- 
- quantum computing architecture. *IEEE Journal of Selected Topics In Quantum Electronics*, 9:1552, 2003.
- [201] M. Oskin, F. T. Chong, I. L. Chuang, and J. Kubiawicz. Building quantum wires: The long and the short of it. In *Proc. 30th Annual Int. Symp. Comp. Arch.*, pages 374–387, 2003.
- [202] B. Georgeot. Quantum computing of poicare recurrences and periodic orbits. *Phys. Rev. A*, 69:032301, 2004. quant-ph/0307233.
- [203] J. Du, M. Shi, X. Zhou, Y. Fan, B. Ye, R. Han, and J. Wu. Implementation of a quantum algorithm to solve the bernstein-vazirani parity problem without entanglement on an ensemble quantum computer. *Phys. Rev. A*, 64:042306, 2001. quant-ph/0012114.
- [204] H.-K. Lo and H. F. Chau. Universal quantum simulators. *Science*, 273:1073–1078, 1996.
- [205] C. Zalka. Simulating quantum systems on a quantum computer. *Proc. R. Soc. Lond. A*, 454:313–322, 1998.
- [206] R. R. Tucci. Qubiter algorithm modification, expressing unstructured unitary matrices with fewer cnots. *quant-ph/0411027*, 2004.
- [207] V. V. Shende, S. S. Bullock, and I. L. Markov. A practical top-down approach to quantum circuit synthesis. *quant-ph/0406176*, 2004.
- [208] V. Bergholm, J. Vartiainen, M. Mottonen, and M. Salomaa. Quantum circuit for a direct sum of two-dimensional unitary operators. *quant-ph/0410066*, 2004.